NOTICE

The quality of this microform is heavily dependent upon the quality of the original thesis submitted for microfilming. Every effort has been made to ensure the highest quality of reproduction possible.

If pages are missing, contact the university which granted the degree.

Some pages may have indistinct print especially if the original pages were typed with a poor typewriter ribbon or if the university sent us an inferior photocopy.

AVIS

La qualité de cette microforme dépend grandement de la qualité de la thèse soumise au microfilmage. Nous avons tout fait pour assurer une qualité supérieure de reproduction.

S'il manque des pages, veuillez communiquer avec l'université qui a conféré le grade.

La qualité d'impression de certaines pages peut laisser à désirer, surtout si les pages originales ont été dactylographiées à l'aide d'un ruban usé ou si l'université nous a fait parvenir une photocopie de qualité inférieure.

UNIVERSITY OF ALBERTA

The Rotating Thermosyphon:
a numerical analysis of steady, laminar behaviour

by

Litong Zhao

A THESIS

SUBMITTED TO THE FACULTY OF GRADUATE STUDIES AND RESEARCH

IN PARTIAL FULFILMENT OF THE REQUIREMENTS FOR THE DEGREE

OF Doctor of Philosophy

Department of Mechanical Engineering

EDMONTON, ALBERTA

Spring, 1992

ISBN 0-315-73094-3

UNIVERSITY OF ALBERTA

RELEASE FORM

NAME OF AUTHOR Litong Zhao

TITLE OF THESIS The Rotating Thermosyphon: a numerical analysis of steady, laminar behaviour

DEGREE FOR WHICH THESIS WAS PRESENTED Doctor of Philosophy

YEAR THIS DEGREE GRANTED Spring, 1992

(SIGNED) Litong Zhao

PERMANENT ADDRESS:

....

....

....

DATED March 16 1992

UNIVERSITY OF ALBERTA

FACULTY OF GRADUATE STUDIES AND RESEARCH

The undersigned certify that they have read, and recommend to the Faculty of Graduate Studies and Research, for acceptance, a thesis entitled The Rotating Thermosyphon: a numerical analysis of steady, laminar behaviour submitted by Litong Zhao in partial fulfilment of the requirements for the degree of Doctor of Philosophy.

....
Dr. G.S.H. Lock
Supervisor

....
Dr. D.J. Steigmann

....
Dr. K.C. Cheng

....
Dr. L.W. Sigurdson

....
Dr. W.H. Finlay

....
Dr. K. Nandakumar

....
Dr. A.C.M. Sousa
External Examiner

Date.... March 12, 1992 ....

To

My Grandmother

and

My Parents

ABSTRACT

The three-dimensional flow pattern and heat transfer characteristics of square section, rotating, closed thermosyphons were explored using the SIMPLE-C algorithm to solve the three-dimensional Navier-Stokes equations under steady, laminar flow conditions. The effects of Rayleigh number, Ekman number, Prandtl number, gravity and eccentricity on the behaviour of radial, eccentric and concentric thermosyphons were revealed.

The flow pattern in a radial thermosyphon consists of an annular refluent flow near the two closed ends combined with a bifilamental flow in the mid length region. A distinctive feature of the rotating radial thermosyphon is that the Coriolis force may flatten the axial velocity profile, making it look almost two-dimensional.

In an eccentric thermosyphon, a bifilamental main circulation is formed; superimposed on that is an S-shaped secondary flow induced near the ends by buoyancy and Coriolis forces. This secondary flow modifies the main flow profile.

As expected, the flow pattern of a concentric thermosyphon consists of a central core in which hot fluid moves towards the cold end and an annular flow in which cold fluid moves towards the hot end. Under the influence of the Coriolis force,a converging ring flow (at the hot end) and a diverging ring flow (at the cold end) are formed.

The plots of Nu~Ra indicate that an impeded regime succeeds the conduction regime for all the three thermosyphons; and they suggest that a boundary layer regime succeeds the impeded regime in radial and eccentric thermosyphons at least.

When Ek decreases, the heat transfer rate has a maximum for the radial thermosyphon, whereas the heat transfer rates decrease monotonically for eccentric and concentric thermosyphons. At about $Ek=10^{-2}$, the heat transfer rate for all the three types begin to drop quickly when Ek decreases further. It seems that the flow regime is defined by both Ra and Ek. As the Ekman number decreases, the Coriolis force plays a bigger role.

Flow patterns and Nusselt numbers are almost the same for Pr>>1. For liquid metal (Pr=0.01), however, flow is much more vigorous, and Nu is lower.

As gravity becomes important, the heat transfer rate is higher, and the flow pattern may be modified accordingly.

When eccentricity becomes smaller, the heat transfer rates are lower due to a weaker body force field. The heat transfer rate of the concentric thermosyphon is the lowest.

ACKNOWLEDGEMENT

The author wishes to express sincere thanks to his supervisor, Dr. G.S.H. Lock, for suggesting the topic and giving thoughtful guidance throughout the course of this study.

A Teaching Assistantship from the Department of Mechanical Engineering and a Research Assistantship from the Natural Sciences and Engineering Research Council of Canada are greatly appreciated.

The author is grateful to his family in China and his friends in Canada for their emotional support and encouragement throughout his study in the University of Alberta.

Table of Contents

Chapter Page

List of Figures

Figure		Page

Figure Page

Figure | Page

Figure Page

NOMENCLATURE

A	power-law interpolation function; surface area
A_x	S/D, aspect ratio in the X-direction
A_y	L/D, aspect ratio in the Y-direction
a	coefficient of discretized algebraic equation
b	constant in the discretized algebraic equation
C_p	specific heat for isobaric process
D	flux due to diffusion; length in the Z-direction
Ek	Ekman number
F	flux due to convection
g	gravitational acceleration
H	length in defining Nu
k	thermal conductivity
L	length in the Y-direction
Nu	Nusselt number
P	pressure; cell Peclet number
p	non-dimensional pressure
Pr	Prandtl number
Q	total heat flux through the system
r	distance from the rotating axis to the local point
Ra	Rayleigh number
R_g	acceleration ratio
R_l	length ratio
$\mathcal{R}$	distance from the rotating axis to the centre of Z axis
S	length in the X-direction; source term in the model equation

T	temperature
t	time
U	velocity component in the X-direction
u	non-dimensional velocity component in the X-direction
V	velocity component in the Y-direction
v	non-dimensional velocity component in the Y-direction
W	velocity component in the Z-direction
w	non-dimensional velocity component in the Z-direction
X	coordinate
x	non-dimensional coordinate
Y	coordinate
y	non-dimensional coordinate
Z	coordinate
z	non-dimensional coordinate

Greek Letters

β	thermal expansion coefficient
Γ	diffusivity for model equation
κ	thermal diffusivity
μ	kinematic viscosity
ν	dynamic viscosity
ρ	density
ϕ	non-dimensional temperature

ψ	variable for model equation
Ω	rotating speed

Subscripts

0	reference state
B	bottom neighboring point
b	bottom interpolation point
d	dynamic
E	east neighboring point
e	east interpolation point
H	heated wall
L	cooled wall
N	north neighboring point
n	north interpolation point
P	calculated point
S	south neighboring point
s	south interpolation point
T	top neighboring point
t	top interpolation point
W	west neighboring point
w	west interpolation point

Superscript

*	guessed value
'	correction value

1. INTRODUCTION

The origin of the name "thermosyphon" is uncertain; the name appeared as early as 1928 in the sales literature of Deere and Co. to describe their cooling system. However, the idea was used by members of the Perkins family in the early 19th century in their boilers and other heat distribution systems [1] [1].

The thermosyphon is a circulating fluid system designed to transfer heat from one place to another, and is driven by thermal buoyancy forces. A temperature difference between the two end parts of the thermosyphon is all that is required for continuous operation; mechanical inputs are excluded.

According to the nature of the confining boundaries, the number or type of phases, and the nature of the body forces, thermosyphons can be categorized as (a) open or closed; (b) tubular or loop; (c) single-phase or two-phase; (d) gravitational or rotational.

In the literature, there is some confusion between the thermosyphon and the heat pipe. Actually, the heat pipe is similar in construction to the thermosyphon; in the heat pipe a wick is fixed to the inside surface of a tube, and the flow is driven by capillary forces. The wick is an integral and important part of a heat pipe. A system without a wick should be considered a thermosyphon.

---

[1] References are given numerically.

Some common industrial applications of the thermosyphon include gas turbine blade cooling, electrical machine rotor cooling, nuclear reactor cooling, heat exchangers, and cooling for internal combustion engines. Some other applications of thermosyphons include preservation of permafrost, cryogenic cool-down apparatus, and steam tubes for bakers' ovens. Because of the variety of thermosyphon characteristics, numerous future applications could be added to the list.

Probably the best known application of the rotating thermosyphon, especially in their early days, is turbine blade cooling where the centrifugal acceleration is responsible for creating a body force field. H. Holzwarth first proposed this application in 1938 [2]. E. Schmidt [3] was the first one to build an experimental apparatus to carry out an experiment with a thermosyphon cooling rotor blade. Later developmental work was reported by H. Cohen and F.J. Bayley [4] on closed and open radial thermosyphons used in blades cooling.

Another application of the rotating thermosyphon is in electrical machine rotor cooling [5,6,7]. Both concentric and eccentric types of thermosyphon were suggested in such applications.

1.1 LITERATURE REVIEW

The thermosyphon literature is extensive. A very good review paper has been written by D. Japikse [1]. A book, The Tubular Thermosyphon: Variations On a Theme, by G.S.H. Lock will soon be available [8]. Some research works on natural convection in enclosures are also relevant to this topic; for example, the review paper by I. Catton [9].

Most of the previous work has been experimental. Some empirical relations were given under different conditions. Though the empirical relations are helpful in obtaining a preliminary idea about the flow regime, and useful in industrial design, they are not very useful in helping us understand detailed flow structures and the real physical process that may lead to the future improvement of the device.

In the next section, a review of previous work on the single-phase, closed, laminar flow thermosyphon will be made. Emphasis will be given to understanding of the flow structures.

1.1.1 Stationary Closed Thermosyphon

Initial contributions to this topic paid little attention to internal flow patterns. Lock [10] and Bayley and Lock [11] reported the first comprehensive experimental and analytical study of the closed vertical thermosyphon where emphasis was given to the type of midtube exchange mechanism and the effect of Prandtl number and aspect ratio on heat transfer. In order to interpret their experimental results, Lock proposed a model with three idealized exchange mechanisms for the midtube region. When the Rayleigh number is beyond a "critical" value, as in a layer of fluid heated from beneath, there is an upward core flow with a refluent annular downward flow in the top half of the tube; in the bottom half of the tube, there is a downward core flow with a refluent annular upward flow. In the middle region, Lock suggested three exchange mechanisms coupling the two parts, as shown in Figure 1.1. At low values of the Rayleigh number, both annular flows return to their own cores, allowing only conduction across the interface. The second mechanism , termed "convection", assumes the annular flow from the bottom half becomes the top half upward core flow, while the annular flow from top half becomes the bottom half downward core flow. The third exchange mechanism, "mixing", presupposes a violent collision of the opposing streams. Lock further noted that he expected in practice that the actual coupling mechanism would probably contain elements of each of the idealized cases.

Japikse [12], Japikse, Jallouk & Winter [13], and Japikse & Winter [14] performed detailed experimental studies of a closed vertical thermosyphon with a circular horizontal cross-section. The fundamental flow process, in the sense of stable laminar flow, was observed to exist, as indicated in Figure 1.2. Flow visualization showed that the midtube exchange mechanism consists of individual streams of

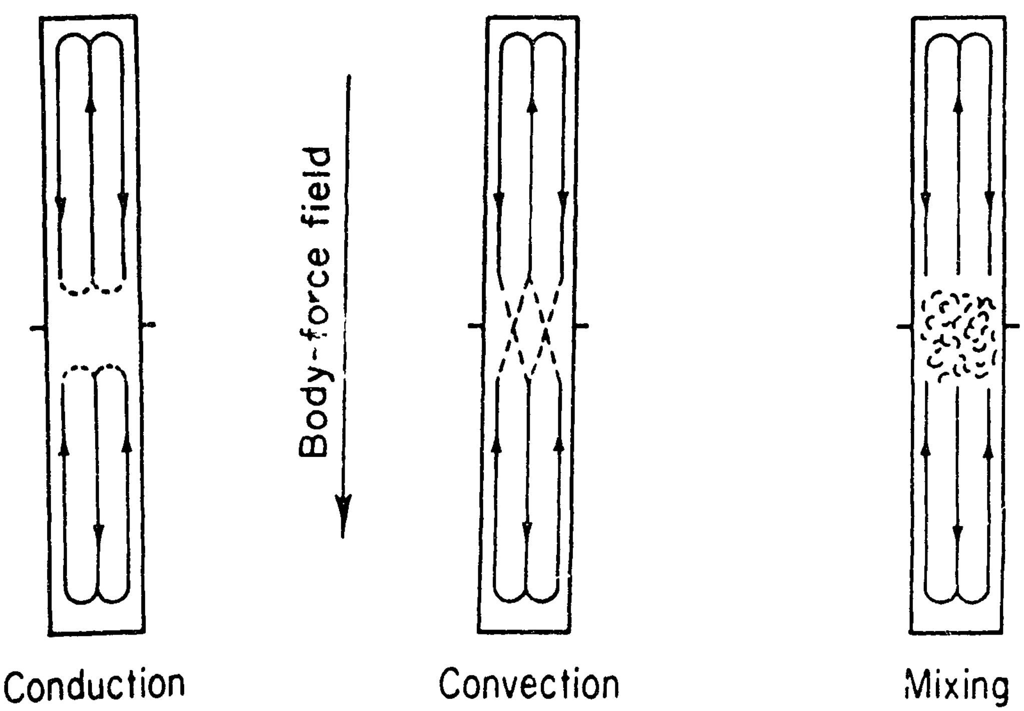

Figure 1.1 Three exchange mechanisms suggested by Lock [10].

ascending hot and descending cold fluid crossing the mid-height plane. The flow streams approach the opposite annular flow and are subsequently bent into a horizontal direction so that they proceed radially toward the tube center. At the centerline they are diverted once again continuing in their original axial direction, and thus forming a cluster of warm (or cool) streams in the cool (or warm) tube halves. The number of streams increases with Rayleigh number. As few as two up and two down, and as many as ten up and ten down were observed depending on the Rayleigh number and the Prandtl number. The Prandtl number was found to be quite important for describing flow stability. Generally, the flow is stable for $Pr>90$ and unstable for $Pr<20$.

A three dimensional numerical study was made of the laminar flow in a closed thermosyphon of square cross section by Mallinson et al.[15]. Good agreement was obtained between the finite-difference solution and the experimental visualizations of Japikse et al. [13] and themselves. The solution for a high Prandtl number fluid identified a conduction regime with a weak toroidal flow, and a convection regime in which an increasing number of individual streams cross the mid-height plane with increasing Rayleigh number. Transitions from toroidal conduction flow to two-stream convection flow, two-stream to four-stream flow and four-stream to six-stream flow were revealed.

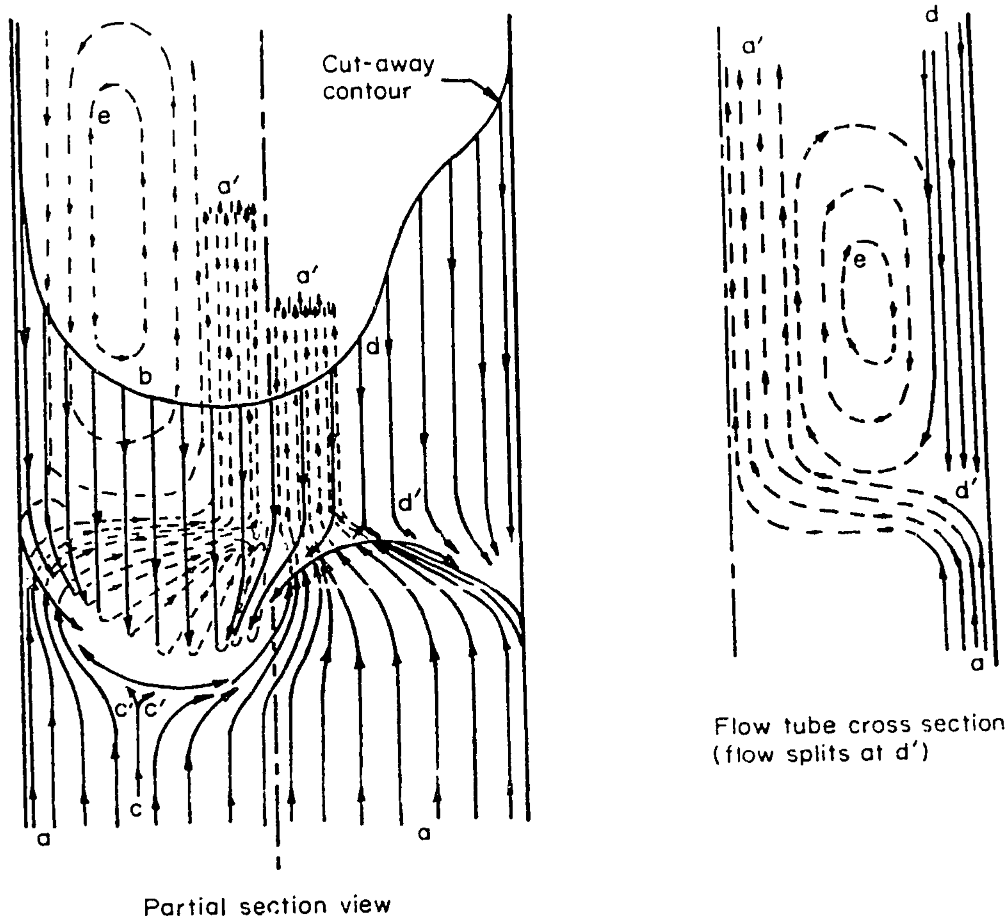

Figure 1.2 Exchange region flow patterns in the vertical closed thermosyphon obtained by Japikse et al. [12,13,14].

Three dimensional buoyancy driven flows in vertical cylindrical tubes were also simulated with a finite difference technique by Crespo et al. [16]. The complex three dimensional flow structure of the asymmetric regime with a range of moderate (1~4) aspect ratios was analysed and displayed graphically, as shown in Figure 1.3. The flow patterns were similar to those of Mallinson et al. [15].

Lock & Zhao [17] conducted a three dimensional numerical study of the laminar flow field in a water-filled, square-section, closed tube thermosyphon with an aspect ratio 5. The effect of altering the longitudinal temperature profile imposed on the long wall was revealed. In the vertical position, a refluent flow appeared at both ends and a pair of opposed filaments was retained in the central region, but a significant change occurred near the mid height position where it was observed that local symmetry of the bifilamental flow was exhibited with respect to a diagonal plane as shown in Figure 1.4. By altering the longitudinal temperature distribution, a Bénard cell in each end was found with large end temperature gradients and smaller central gradients; an extended annular refluent flow over a greater length of the tube was found with large central gradients and nearly isothermal end regions.

Due to the importance of convection in thermal insulation, metal casting and crystallization phenomena, the problem of buoyant circulation in a slender horizontal cavity has also received much attention. The works of

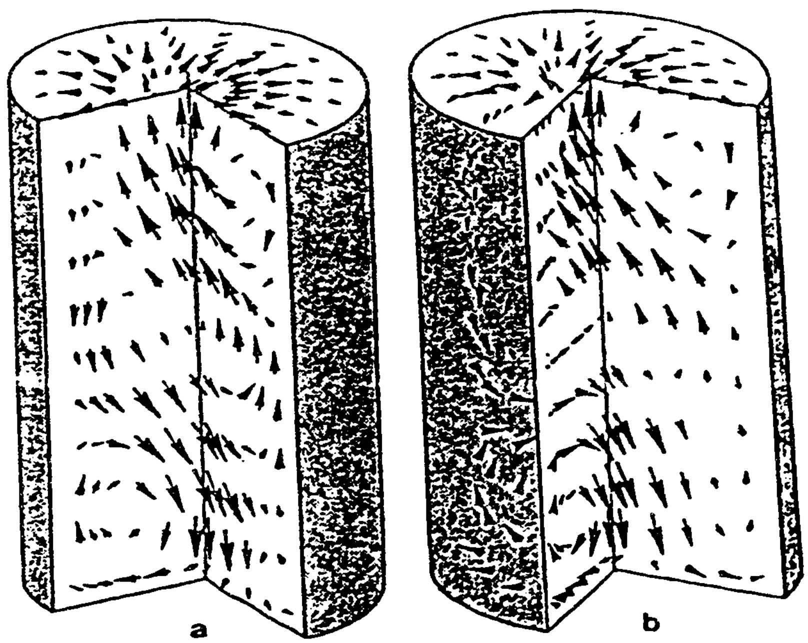

Figure 1.3 Three-dimensional velocity field obtained by Crespo et al. [16].

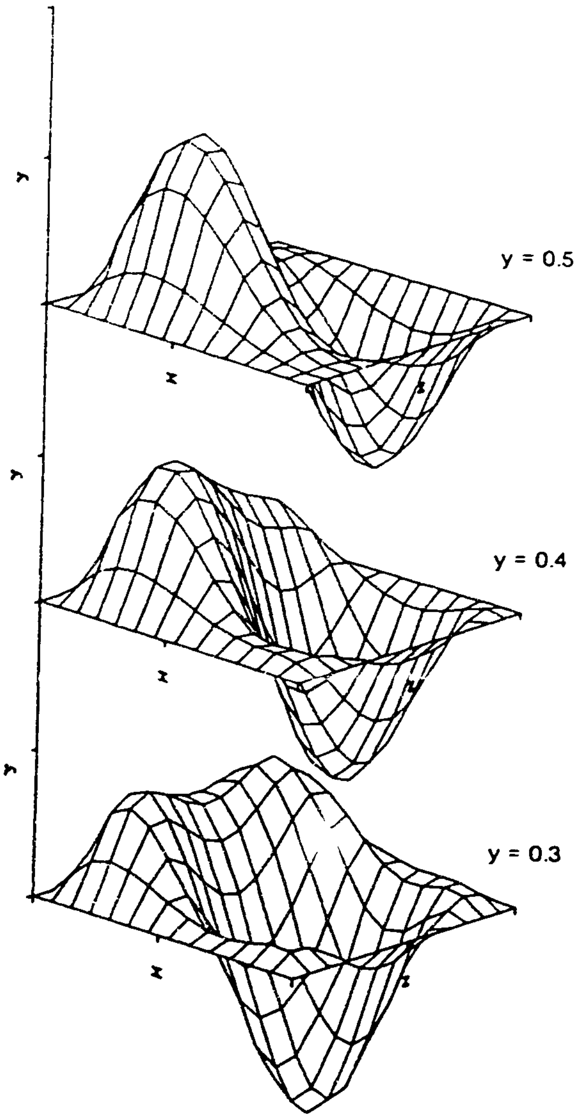

Figure 1.4 Axial velocity profile from numerical results by Lock and Zhao [17].

Cormack, Leal & Imberger [18], Cormack, Leal & Seinfield [19] and Imberger [20] provide an appropriate point of departure. These were analytic, numerical and experimental studies of a two dimensional closed rectangular cavity with the two end walls being held at different temperatures and the side walls being adiabatic. The characteristic flow structure within these slender cavities was revealed: a central bifilamental core region of essentially parallel opposite flows joins two end regions. These findings were supported later by the analysis of Bejan & Tien [21,22] using conducting side walls. A schematic of the flow is shown in Figure 1.5.

Ostrach, Loka & Kumar [23] conducted an experimental study which extend the above observations on two-dimensional cavities to higher Rayleigh numbers and lower slenderness ratios. They not only confirmed the existence of a bifilamental core region, but also discovered secondary cells in the end regions for slenderness ratios less than 5.

Experimental results for free convective flow of gases in a horizontal cylinder with different end temperatures and a linear temperature distribution along the side wall were reported by Schiroky & Rosenberger [24] using a laser Doppler anemometer. It was found that the velocity profiles in the central region near the mid-length point were the same as expected from two-dimensional models, at least for low Rayleigh numbers; for the end regions, pronounced three-dimensional flow behaviour was observed. Smutek et al.

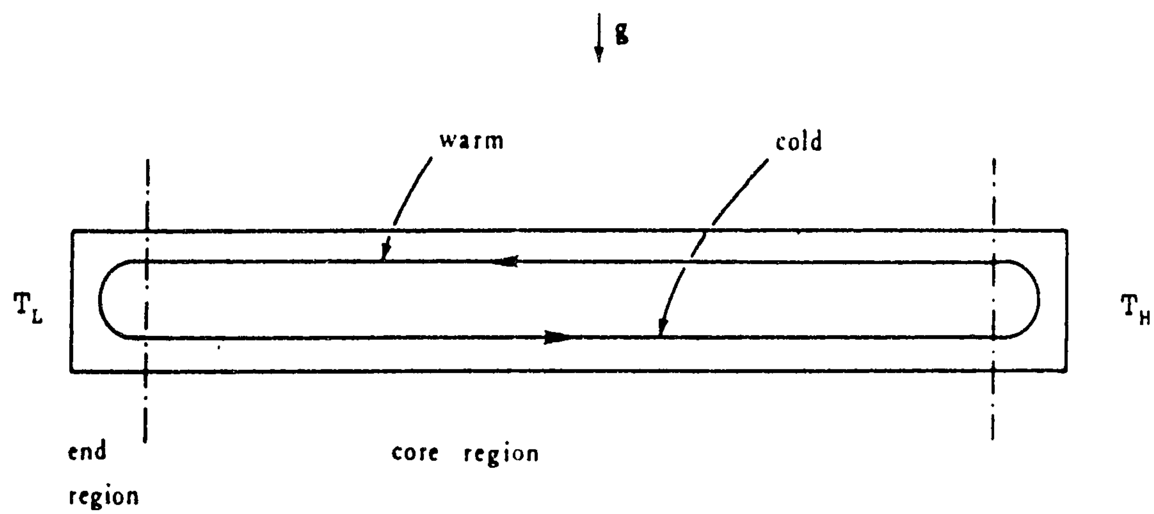

Figure 1.5 Flow pattern in a horizontal cavity with different end temperatures.

[25] conducted a three-dimensional numerical simulation in a horizontal cylinder, and discovered similar flow patterns.

Later, Bontoux et al. [26] carried out a more detailed three-dimensional numerical study of flows in circular cylindrical cavities. They revealed the existence of a paired vortical secondary flow in the mid plane as shown in Figure 1.6. In particular, they were able to reconcile the longitudinal primary circulation, driven by the difference in end wall temperatures, with the lateral secondary circulation, driven by radial temperature gradients. Subsequently, Bontoux et al. [27] systematically organized previous results, by comparing the two-dimensional approximation results and the three-dimensional analysis, to emphasize the inherently three-dimensional character of the flow in cylindrical tubes.

Recently, Han [28], Lock & Han [29], Lock & Zhao [30] performed three-dimensional numerical studies on buoyant laminar flows in an inclined, square-section cavity. Complete heat transfer curves from the conduction regime to the impeded flow regime were given. It was found that a secondary motion in the form of a vortex pair developed within the core filament in the impeded regime. Such secondary flow was found to produce a significant increase in heat transfer rate. The internal details of the flow pattern were found to be quite similar to those reported for a circular cylinder by Bontoux et al. [26].

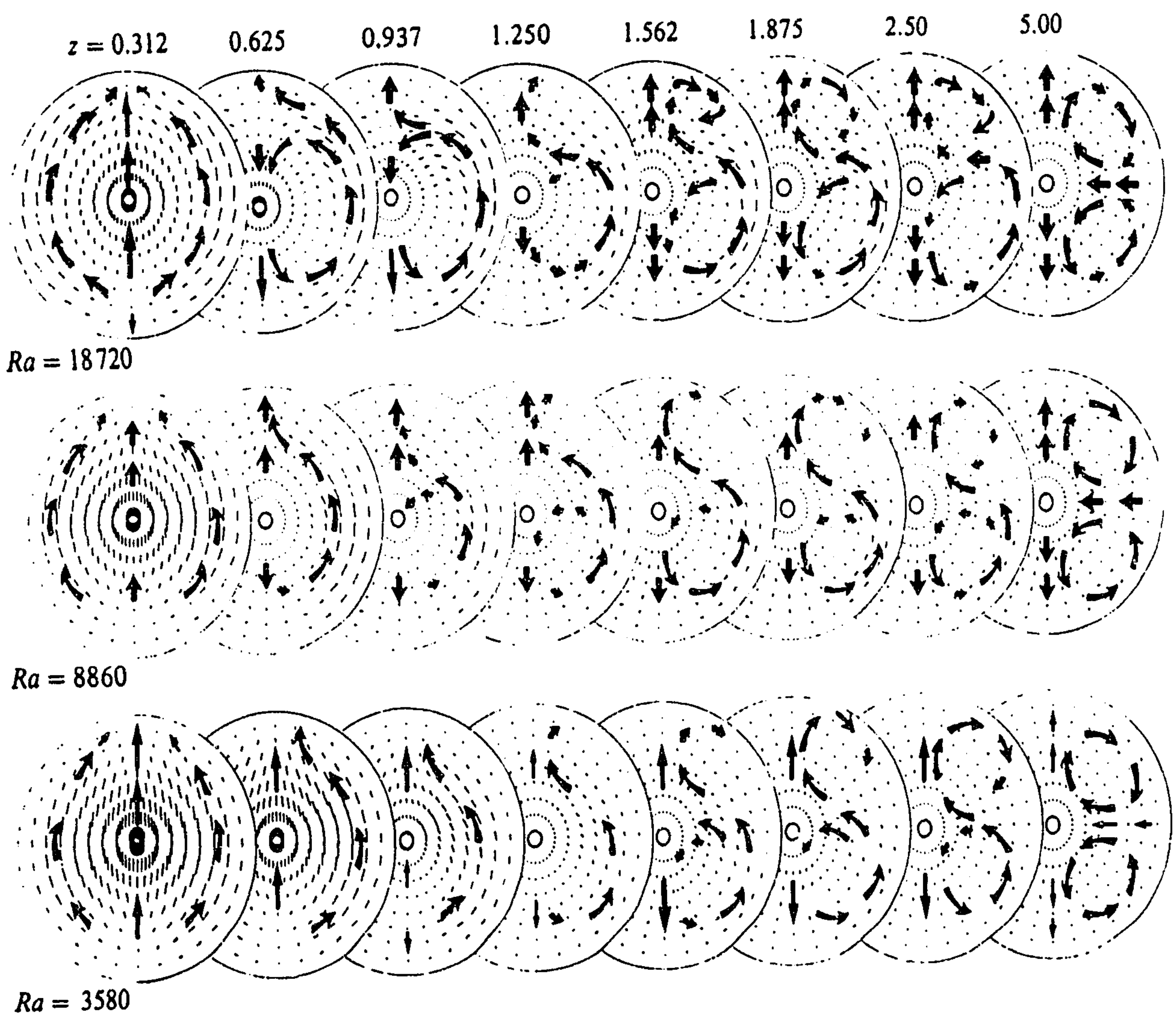

Figure 1.6 Secondary flow pattern in a horizontal cylindrical cavity obtained by Bontoux et al. [26].

1.1.2 Rotating Thermosyphon Simulation

E. Schmidt [3] was the first one to carry out an experiment using the thermosyphon as a tool for cooling rotor blades. Later H. Cohen and F.J. Bayley [4] discussed in detail the advantage of thermosyphon cooling gas turbine rotor blades. Two experiments were conducted. In the first, a rotating apparatus was used to give qualitative indications of the effectiveness of the system; and in the second a static rig was used to study the detailed heat transfer mechanism.

The Pametrada project reported by Brown [31] gave some information concerning rotational effects on closed thermosyphon performance. A liquid metal cylindrical closed thermosyphon was tested. Temperature variations between the two ends of the thermosyphon were attributed to Coriolis forces but were not of a significant magnitude to affect heat transfer.

Ogale [32] investigated a rotating closed thermosyphon for turbine blade cooling with variable diameter holes. He measured heat transfer rates for cylindrical and airfoil cross sections filled with a liquid metal.

Japikse et al. [12,13] conducted a static study of an closed thermosyphon inclined from the vertical to simulate rotation. The gravitational acceleration may then be resolved into two components, one parallel to the tube axis and one normal to it. Visualization studies were made with a transparent apparatus tilted so that the centerline of the thermosyphon was inclined up to 18° from the vertical. Experiments showed that the initial effect of inclination was to cause a gradual rearrangement of the convective exchange mechanism at the vertical position. For inclination angles larger than 12°, the bifilamental flow at the central region almost extended to the two ends.

Bontoux et al. [33] and Lock and Zhao [17] conducted three dimensional numerical studies of a thermosyphon inclined up to 30° degree from vertical. A flow pattern for the inclined thermosyphon was revealed: a deep refluent flow appeared near both ends but a pair of opposed filaments was retained in the central region. Thus, in the lower (hotter) region of the tube, a descending core of cold fluid was balanced by an annulus of warmer ascending fluid which gradually merged into a single filament flowing along the centre of the top half. This model is consistent with experimental observations [12,13,34].

1.2 PURPOSE AND SCOPE OF THIS WORK

Up to now, there appears to be no theoretical work directly related to the study of fluid flow and heat transfer in single-phase rotating thermosyphons. The details of the flow patterns are uncertain except for some knowledge of tilted stationary thermosyphons. The purpose of present work is to use the SIMPLE-C algorithm to explore the single-phase, square section, closed tube thermosyphon under laminar, rotating conditions numerically. Detailed flow patterns will be described for radial, eccentric and concentric thermosyphons rotating about a vertical axis. The effects of Rayleigh number, Ekman number, Prandtl number, gravity and eccentricity on flow pattern and heat transfer rate are revealed. In particular, the influence of the Coriolis force is discussed in detail.

2. FORMULATION AND METHOD OF SOLUTION

2.1 GEOMETRY AND COORDINATE SYSTEM

The problems were cast as natural convection in a square-section rectangular cavity rotating steadily in three different configurations: radial, eccentric and concentric, as shown in Figures 2.1, 2.2, 2.3, respectively. The geometry of the thermosyphon is specified by three lengths: S in the X direction, L in the Y direction, and D in the Z direction. We can define two dimensionless parameters, aspect ratios, to describe the geometry of the thermosyphon. The length D in the Z direction is chosen as the reference length because D is the "diameter" of the tube for all the three configurations; thus $A_x = S/D$ and $A_y = L/D$ are the two aspect ratios in the X and Y directions respectively. The coordinate system is fixed to the thermosyphon as indicated on the figures. The rotating vector Ω is parallel to the X-direction, and the gravitational vector is in the negative X-direction. $\mathcal{R}$ is the radial distance from the rotating axis to the plane Y=0. In the concentric thermosyphon, $\mathcal{R}$ equals to -L/2.

For the radial thermosyphon, the temperature of the surface Y=0 was fixed at a uniform low temperature T_L; the temperature of Y=L surface was fixed at uniform high temperature T_H. For the other four surfaces X=0, X=S, Z=0, and Z=D, the temperature was assumed to vary linearly with Y.

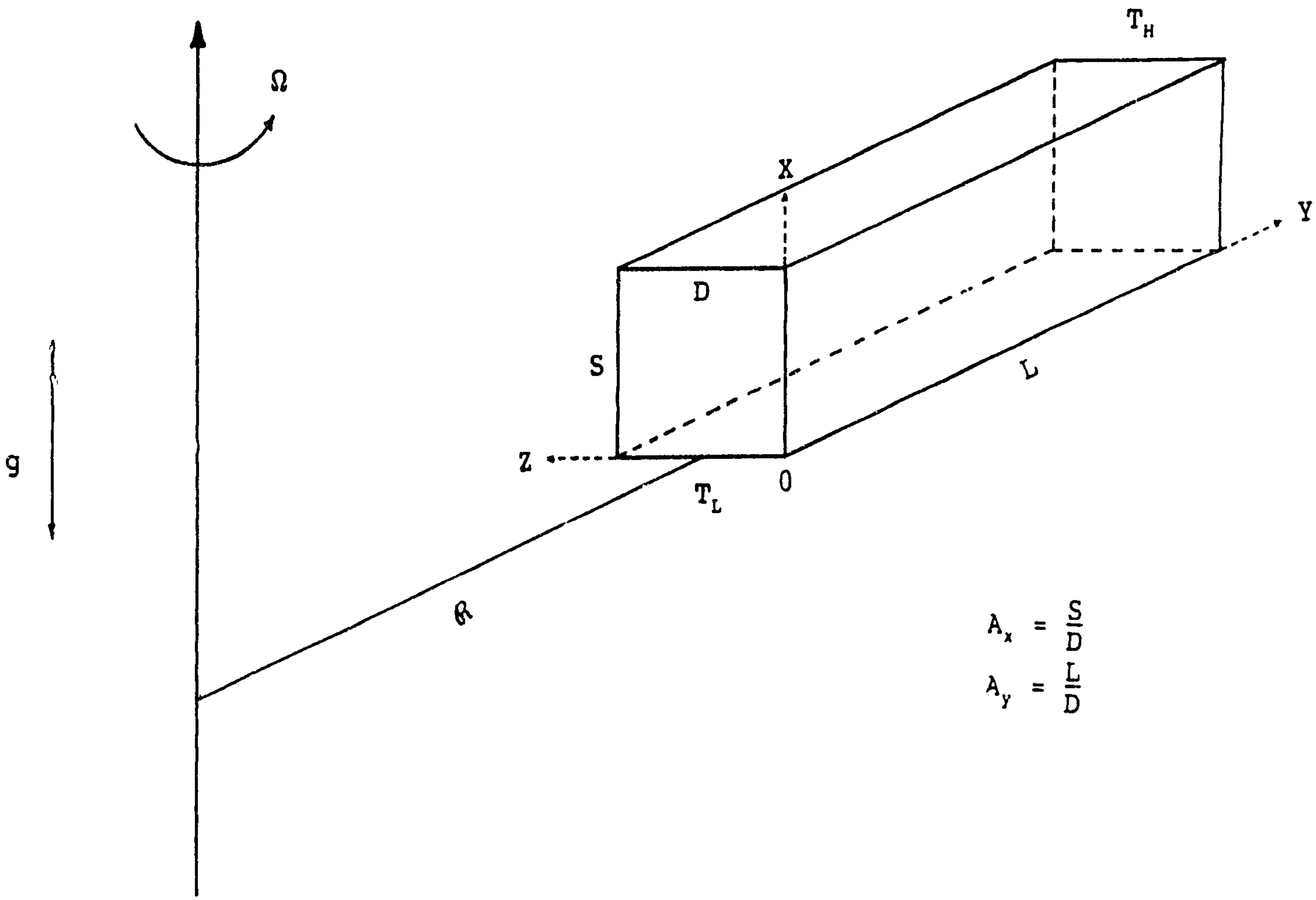

Figure 2.1 Orientation and coordinate system
for radial thermosyphon.

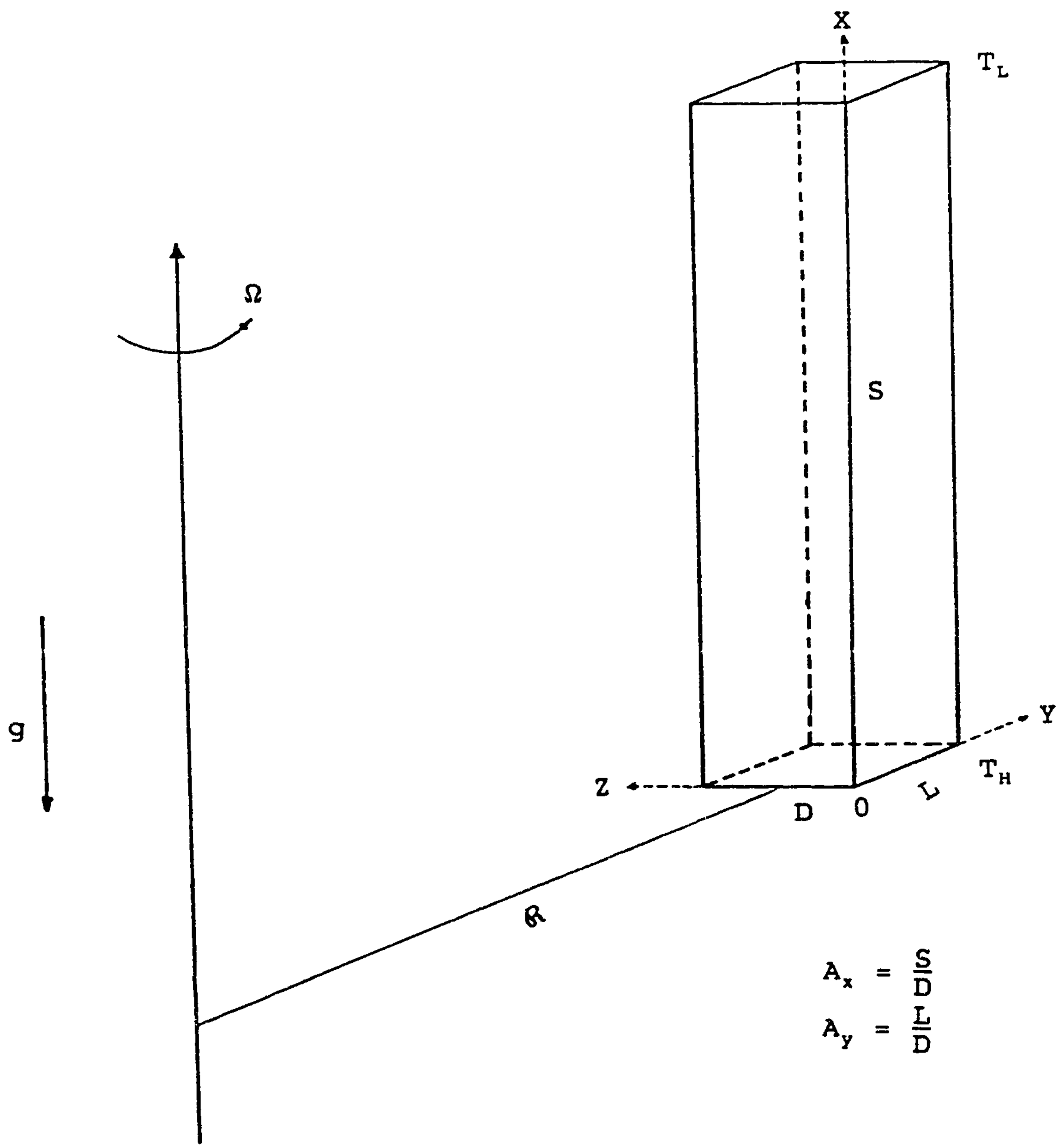

Figure 2.2 Orientation and coordinate system for eccentric thermosyphon.

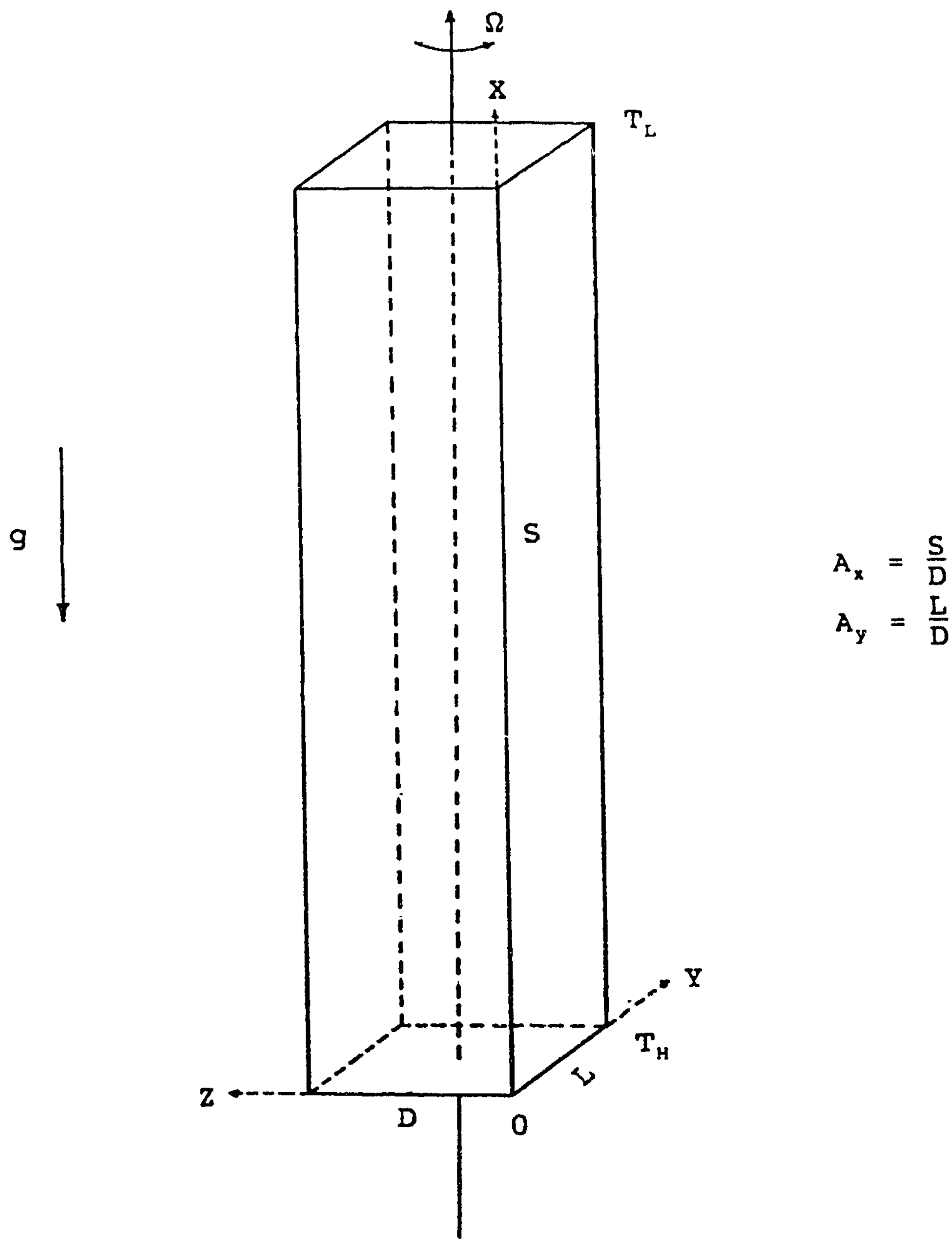

Figure 2.3 Orientation and coordinate system for concentric thermosyphon.

For the eccentric and concentric thermosyphons, the temperature of the surface X=0 was fixed at a uniform high temperature T_H, while that of X=S was fixed at a uniform low temperature T_L. At the other four surfaces Y=0, Y=L, Z=0, Z=D, the temperature varied linearly with X. Thus the boundary temperature was uniform at the ends and around the circumference at any given section.

2.2 FORMULATION OF THE PROBLEM

If the Eckert number is small, the viscous dissipation and compression work in the energy equation may be neglected. For natural convection in rotating system, the scale of velocity may be written as $V_0^2=\beta\Delta T\Omega^2\mathcal{R}D$; then

$$Ek = \frac{V^2}{C_p\Delta T} = \frac{\beta\Delta T\Omega^2\mathcal{R}D}{C_p\Delta T} = \frac{\beta\Omega^2\mathcal{R}D}{C_p}$$

The new group $\beta\Omega^2\mathcal{R}D/C_p$ has been called Ostrach number [44]. The typical range of Ostrach number for most fluid is from 10^{-5} to 10^{-6} at the largest.

For a newtonian fluid at constant rotating speed Ω, the equations for conservation of mass, momentum and energy under rotation conditions can be written as [42]:

$$\frac{D\rho}{Dt} + \rho\ \nabla\cdot\bar{V} = 0 \tag{2.1}$$

$$\rho\frac{D\bar{V}}{Dt} + 2\rho\ \bar{\Omega}\times\bar{V} + \rho\ \bar{\Omega}\times(\bar{\Omega}\times\bar{r}) = -\nabla P + \rho\bar{g} - \mu\ \nabla\times(\nabla\times\bar{V}) \tag{2.2}$$

$$\rho C_p \frac{DT}{Dt} = k \nabla^2 T \tag{2.3}$$

The D/Dt is the material derivative which consists of contributions from both the local and convective time rate of change. The $\bar{r}$ is the displacement vector from the axis of rotation.

It should be noted that, generally speaking, the physical properties of fluid in the above equations are functions of the temperature and pressure. It is difficult to solve such equations exactly. Some more assumptions have to be made to simplify the situation.

The Boussinesq approximation is used here to simplify the problem, that is,

(1) The density variation is taken to be negligible except where the body force field is concerned. (The $\rho\bar{\Omega}\times(\bar{\Omega}\times\bar{r})$ term in (2.2) is treated as a body force field, even through strictly speaking it is an inertial term.)

(2) Other physical properties of the fluid are treated as constant.

The general discussion of the validity of the Boussinesq approximation can be found in references [35,36,43]. The most demanding conditions are

$$\beta\Delta T < 0.1, \qquad \alpha\Delta T < 0.1 \tag{2.4}$$

where

$$\beta = -\frac{1}{\rho}\left(\frac{\partial \rho}{\partial T}\right)_P, \qquad a = -\frac{1}{\mu}\left(\frac{\partial \mu}{\partial T}\right)_P \tag{2.5}$$

are the thermal expansion coefficient and relative viscosity change with respect to temperature. The buoyancy terms consist of both the rotational and gravitational effects, and can be written as

$$\rho_0 \, [\bar{g} - \bar{\Omega}\times(\bar{\Omega}\times\bar{r})] - \rho\beta(T-T_0)[\bar{g} - \bar{\Omega}\times(\bar{\Omega}\times\bar{r})] \tag{2.6}$$

where T_0 is the reference temperature:

$$T_0 = 0.5(T_H + T_L) \tag{2.7}$$

The pressure may be split into two (static and dynamic) parts,

$$P = P_0 + P_d \tag{2.8}$$

where the hydrostatic part, P_0, is going to balance the "head" of fluid, and has no effect on the fluid motion; that is,

$$-\nabla P_0 + \rho_0 \, [\bar{g} - \bar{\Omega}\times(\bar{\Omega}\times\bar{r})] = 0 \tag{2.9}$$

Only the dynamic pressure P_d, affects fluid flow.

Finally, under steady state condition, the governing equations simplify to:

$$\nabla \cdot \bar{V} = 0 \tag{2.10}$$

$$(\bar{V} \cdot \nabla)\ \bar{V} + 2\ \bar{\Omega} \times \bar{V}$$
$$= \frac{1}{\rho} \nabla P_d - \beta (T - T_0) [\bar{g} - \bar{\Omega} \times (\bar{\Omega} \times \bar{r})] + \nu\ \nabla^2 \bar{V} \tag{2.11}$$

$$\bar{V} \cdot \nabla T = \kappa\ \nabla^2 T \tag{2.12}$$

The above partial differential equations can be written in component form using the Cartesian coordinate system indicated in figures (2.1 - 2.3). Thus

$$\frac{\partial U}{\partial X} + \frac{\partial V}{\partial Y} + \frac{\partial W}{\partial Z} = 0 \tag{2.13}$$

$$U\frac{\partial U}{\partial X} + V\frac{\partial U}{\partial Y} + W\frac{\partial U}{\partial Z} = -\frac{1}{\rho}\frac{\partial P_d}{\partial X}$$
$$+ \nu\left[\frac{\partial^2 U}{\partial X^2} + \frac{\partial^2 U}{\partial Y^2} + \frac{\partial^2 U}{\partial Z^2}\right] + \beta (T - T_0) g \tag{2.14}$$

$$U\frac{\partial V}{\partial X} + V\frac{\partial V}{\partial Y} + W\frac{\partial V}{\partial Z} = -\frac{1}{\rho}\frac{\partial P_d}{\partial Y}$$
$$+ \nu\left[\frac{\partial^2 V}{\partial X^2} + \frac{\partial^2 V}{\partial Y^2} + \frac{\partial^2 V}{\partial Z^2}\right] - \beta (T - T_0) \Omega^2 (\mathcal{R} + Y) + 2\Omega W \tag{2.15}$$

$$U\frac{\partial W}{\partial X} + V\frac{\partial W}{\partial Y} + W\frac{\partial W}{\partial Z} = -\frac{1}{\rho}\frac{\partial P_d}{\partial Z}$$
$$+ \nu\left[\frac{\partial^2 W}{\partial X^2} + \frac{\partial^2 W}{\partial Y^2} + \frac{\partial^2 W}{\partial Z^2}\right] - \beta (T - T_0) \Omega^2 (Z - \frac{D}{2}) - 2\Omega V \tag{2.16}$$

$$U\frac{\partial T}{\partial X} + V\frac{\partial T}{\partial Y} + W\frac{\partial T}{\partial Z}$$
$$= \kappa\left[\frac{\partial^2 T}{\partial X^2} + \frac{\partial^2 T}{\partial Y^2} + \frac{\partial^2 T}{\partial Z^2}\right] \tag{2.17}$$

The no-slip boundary conditions at all six walls will be adopted here for the three components of the velocity, i.e.

$$U = V = W = 0$$

at $X = 0$, $X = S$, $Y = 0$, $Y = L$, $Z = 0$, $Z = D$.

The temperature boundary conditions for the radial thermosyphon are:

$$T = T_L, \qquad \text{at } Y = 0$$

$$T = T_H, \qquad \text{at } Y = L$$

$$T = T_L + \frac{Y}{L}(T_H - T_L) \qquad \text{at } X = 0,\ X = S,\ Z = 0,\ Z = D.$$

In the eccentric and concentric cases, the temperature boundary condition is:

$$T = T_H, \qquad \text{at } X = 0$$

$$T = T_L, \qquad \text{at } X = S$$

$$T = T_H - \frac{X}{S}(T_H - T_L) \qquad \text{at } Y = 0,\ Y = L,\ Z = 0,\ Z = D.$$

The linear temperature distribution simulates conducting walls. In a real situation, the appropriate condition might be between a linear distribution and an adiabatic condit. ..

2.3 NON-DIMENSIONALIZATION

Non-dimensionalization will be employed here instead of normalization due to the complexity of the problem. It is obvious that there are many choices in selecting a set of scales for non-dimensionalization. For a rotating thermosyphon, the non-dimensional variables will be defined as

$$x = \frac{X}{S}$$

$$y = \frac{Y}{L}$$

$$z = \frac{Z}{D}$$

$$u = \frac{U}{A_x\sqrt{\beta(T_H-T_0)\Omega^2(\mathcal{R}+L)D}}$$

$$v = \frac{V}{A_y\sqrt{\beta(T_H-T_0)\Omega^2(\mathcal{R}+L)D}}$$

$$w = \frac{W}{\sqrt{\beta(T_H-T_0)\Omega^2(\mathcal{R}+L)D}}$$

$$\phi = \frac{T-T_0}{T_H-T_0}$$

$$p = \frac{P_d}{\rho\beta(T_H-T_0)\Omega^2(\mathcal{R}+L)D}$$

Substituting the above variables into equations (2.13-2.17), we can write the non-dimensionalized equations as follows:

$$\frac{\partial u}{\partial x} + \frac{\partial v}{\partial y} + \frac{\partial w}{\partial z} = 0 \qquad (2.18)$$

$$u\frac{\partial u}{\partial x} + v\frac{\partial u}{\partial y} + w\frac{\partial u}{\partial z} = -\frac{1}{A_x^2}\frac{\partial p}{\partial x}$$

$$+ \sqrt{\frac{2Pr}{Ra}}\left[\frac{1}{A_x^2}\frac{\partial^2 u}{\partial x^2} + \frac{1}{A_y^2}\frac{\partial^2 u}{\partial y^2} + \frac{\partial^2 u}{\partial z^2}\right] + \frac{1}{A_x R_g}\phi \qquad (2.19)$$

$$u\frac{\partial v}{\partial x} + v\frac{\partial v}{\partial y} + w\frac{\partial v}{\partial z} = -\frac{1}{A_y^2}\frac{\partial p}{\partial y}$$

$$+ \sqrt{\frac{2Pr}{Ra}}\left[\frac{1}{A_x^2}\frac{\partial^2 v}{\partial x^2}+\frac{1}{A_y^2}\frac{\partial^2 v}{\partial y^2}+\frac{\partial^2 v}{\partial z^2}\right]$$

$$- \frac{1}{A_y}\left(\frac{R_1+y}{R_1+1}\right)\phi + \frac{2}{A_y}\sqrt{\frac{2Pr}{Ra\ Ek^2}}\ w \qquad (2.20)$$

$$u\frac{\partial w}{\partial x} + v\frac{\partial w}{\partial y} + w\frac{\partial w}{\partial z} = -\frac{\partial p}{\partial z}$$

$$+ \sqrt{\frac{2Pr}{Ra}}\left[\frac{1}{A_x^2}\frac{\partial^2 w}{\partial x^2}+\frac{1}{A_y^2}\frac{\partial^2 w}{\partial y^2}+\frac{\partial^2 w}{\partial z^2}\right]$$

$$- \frac{1}{A_y}\left(\frac{z-0.5}{R_1+1}\right)\phi - 2A_y\sqrt{\frac{2Pr}{Ra\ Ek^2}}\ v \qquad (2.21)$$

$$u\frac{\partial \phi}{\partial x} + v\frac{\partial \phi}{\partial y} + w\frac{\partial \phi}{\partial z}$$

$$= \sqrt{\frac{2}{Pr\ Ra}}\left[\frac{1}{A_x^2}\frac{\partial^2 \phi}{\partial x^2}+\frac{1}{A_y^2}\frac{\partial^2 \phi}{\partial y^2}+\frac{\partial^2 \phi}{\partial z^2}\right] \qquad (2.22)$$

where

$Ra = \dfrac{\beta(T_H-T_L)\Omega^2(\mathcal{R}+L)D^3}{\nu\ \kappa}$ is the diameter based Rayleigh number.

$Ek = \dfrac{\nu}{\Omega D^2}$ is the Ekman number.

$Pr = \dfrac{\nu}{\kappa}$ is the Prandtl number.

$R_g = \dfrac{\Omega^2(\mathcal{R}+L)}{g}$ is the acceleration ratio.

$R_1 = \dfrac{\mathcal{R}}{L}$ is the eccentricity.

As a result of non-dimensionalization, five parameters appear. The Rayleigh number characterizes the relative importance of the buoyancy and viscous effects. The Ekman number is a measure of the viscous force compared to the Coriolis force. The Prandtl number is simply a property of the fluid and is the relative ability of the fluid to diffuse momentum versus heat. The acceleration ratio is the ratio of centrifugal force over the gravity force. The eccentricity is the ratio of the distance from the rotating axis to the thermosyphon and the radial length of the thermosyphon.

The non-dimensionalized hydrodynamic boundary conditions follow as

$u=v=w=0$, at $x=0$, $x=1$, $y=0$, $y=1$, $z=0$, $z=1$.

While the thermal boundary conditions for radial thermosyphon are,

$\phi=-1$, at $y=0$.

$\phi=1$, at $y=1$.

$\phi=2y-1$, at $x=0$, $x=1$, $z=0$, $z=1$.

For eccentric and concentric thermosyphons,

$\phi=1$, at $x=0$.

$\phi=-1$, at $x=1$.

$\phi=1-2x$, at $y=0$, $y=1$, $z=0$, $z=1$.

2.4 METHOD OF SOLUTION

2.4.1 General Discussion

The governing equations (2.18) to (2.22) form a set of nonlinear elliptic partial differential equations. It is impossible to use classical analytical methods to solve these equations in closed form. Fortunately, the development of numerical methods and the availability of large digital computers make it possible to solve these equations numerically.

There are quite a few procedures which can be used to solve the partial differential equations numerically. Two major classes are the finite difference method and the finite element method. Finite difference methods have been well developed for fluid flow and heat transfer. In general, finite difference methods are attractive for physical problems with geometrically simple boundaries.

One of the algorithms proven to be valid in solving convection diffusion problems, especially in three dimensions, is the SIMPLE-type algorithm [37]. Instead of using the central difference scheme, or the up-wind scheme, the power-law scheme is here adopted to solve the convection and diffusion problems. In a convection-diffusion problem where the pressure is neither prescribed nor given explicitly by an equation, the continuity equation in the SIMPLE algorithm is transformed into an equation for pressure.

In this study, a modification to the SIMPLE algorithm (Semi-Implicit Method for Pressure-Linked Equations), the SIMPLE-C (SIMPLE-consistent) algorithm of Van Doormaal and Raithby [38] will be used.

2.4.2 Discretization

The full details of derivation are described in references [37,38]. Only some major steps are given here.

To illustrate the method, if the dependent variable is denoted by ψ, the general differential equation may be written as:

$$\bar{V}\cdot\nabla\psi = \Gamma\ \nabla^2\psi + S \tag{2.23}$$

First the full spatial domain is divided into N×M×L small rectangular volumes. N is the number of divisions in the X direction, and M and L are those in the Y and Z directions, respectively. Integrating the equation (2.23) over the whole domain, gives

$$\int \bar{V}\cdot\nabla\psi\ dV = \int \Gamma\nabla^2\psi\ dV + \int S\ dV \tag{2.24}$$

One sample finite volume is depicted in Figure 2.4 to illustrate the evaluation of the integral in (2.24). 1 The centre point of the finite volume, the calculating point, is designated as P and the neighboring points as E, W, N, S, T and B correspondingly. Points on the six surfaces of the

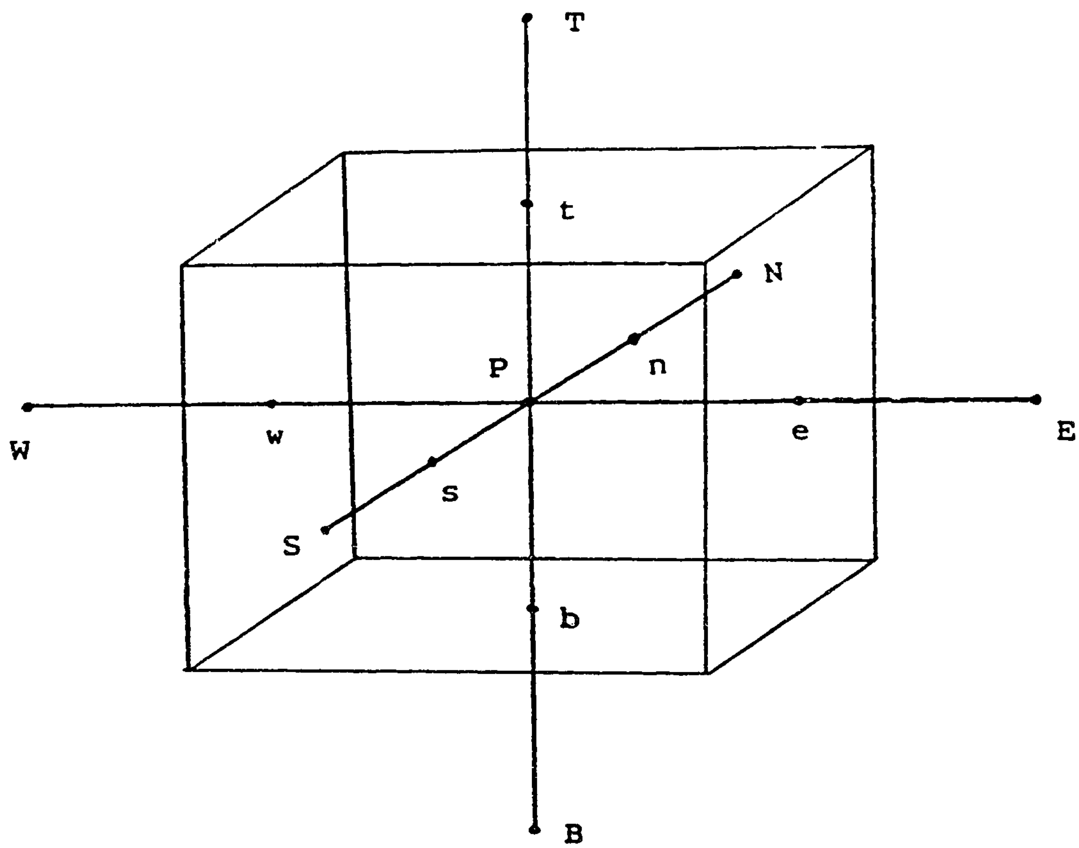

Figure 2.4 A sample finite volume.

volume are called e. w, n, s, t and b, respectively.

The final discretization equation for the point P in the form of an algebraic equation can be written as:

$$a_P\psi_P = a_E\psi_E + a_W\psi_W + a_N\psi_N + a_S\psi_S + a_T\psi_T + a_B\psi_B + b \qquad (2.25)$$

where

$$a_E = D_eA(|P_e|) + MAX(-F_e,0) \qquad (2.26a)$$

$$a_W = D_wA(|P_w|) + MAX(-F_w,0) \qquad (2.26b)$$

$$a_N = D_nA(|P_n|) + MAX(-F_n,0) \qquad (2.26c)$$

$$a_S = D_sA(|P_s|) + MAX(-F_s,0) \qquad (2.26d)$$

$$a_T = D_tA(|P_t|) + MAX(-F_t,0) \qquad (2.26e)$$

$$a_B = D_bA(|P_b|) + MAX(-F_b,0) \qquad (2.26f)$$

$$b = S\Delta x\Delta y\Delta z \qquad (2.26g)$$

$$a_P = a_E + a_W + a_N + a_S + a_T + a_B \qquad (2.26h)$$

F and D are flow rates and diffusion conductance. They are defined as

$$F_e = u_e \Delta y \Delta z \qquad D_e = \frac{\Gamma \Delta y \Delta z}{(\delta x)_e} \tag{2.27a}$$

$$F_w = u_w \Delta y \Delta z \qquad D_w = \frac{\Gamma \Delta y \Delta z}{(\delta x)_w} \tag{2.27b}$$

$$F_n = v_n \Delta z \Delta x \qquad D_n = \frac{\Gamma \Delta z \Delta x}{(\delta y)_n} \tag{2.27c}$$

$$F_s = v_s \Delta z \Delta x \qquad D_s = \frac{\Gamma \Delta z \Delta x}{(\delta y)_s} \tag{2.27d}$$

$$F_t = w_t \Delta x \Delta y \qquad D_t = \frac{\Gamma \Delta x \Delta y}{(\delta z)_t} \tag{2.27e}$$

$$F_b = w_b \Delta x \Delta y \qquad D_b = \frac{\Gamma \Delta x \Delta y}{(\delta z)_b} \tag{2.27f}$$

The Peclet number P is taken as the ratio of F and D; thus,

$$P_e = \frac{F_e}{D_e} \tag{2.28}$$

and so on.

The power-law formulation for the function $A(|P|)$ is adopted in the form

$$A(|P|) = MAX(0, (1-0.1|P|)^5) \tag{2.29}$$

Equations (2.25) for all the nodal points in the domain thus form a set of linear algebraic equations which can be solved by using the TDMA algorithm.

2.4.3 Algorithm

It has been noted that the velocities can be obtained only when the pressure field is given or is somehow estimated. Unless the correct pressure field is employed, the resulting velocity field will not satisfy the continuity equation. An imprecise velocity field based on a guessed pressure field p^* is denoted by u^*, v^*, w^*. This velocity field is obtained from the following equations:

$$a_e u_e^* = \Sigma\, a_{nb} u_{nb}^* + (p_P^* - p_E^*) A_e + b \qquad (2.30a)$$

$$a_n v_n^* = \Sigma\, a_{nb} v_{nb}^* + (p_P^* - p_N^*) A_n + b \qquad (2.30b)$$

$$a_t w_t^* = \Sigma\, a_{nb} w_{nb}^* + (p_P^* - p_T^*) A_t + b \qquad (2.30c)$$

Suppose the correct pressure p is

$$p = p^* + p' \qquad (2.31)$$

Where p' will be called the pressure correction. The coresponding velocity corrections u', v', w' can be introduced in a similar way, thus

$$u = u^* + u' \qquad (2.32a)$$

$$v = v^* + v' \qquad (2.32b)$$

$$w = w^* + w' \tag{2.32c}$$

Substituting (2.32) into (2.30), and noting that u, v, w will satisfy equations (2.30), gives

$$a_e u'_e = \Sigma\, a_{nb} u'_{nb} + (p'_P - p'_E) A_e \tag{2.33a}$$

$$a_n v'_n = \Sigma\, a_{nb} v'_{nb} + (p'_P - p'_N) A_n \tag{2.33b}$$

$$a_t w'_t = \Sigma\, a_{nb} w'_{nb} + (p'_P - p'_T) A_t \tag{2.33c}$$

Referring to reference [38], the velocity correction equations in the SIMPLE-C algorithm are obtained by subtracting the $\Sigma\, a_{nb} u'_e$ term from both sides of the equations, and the term $\Sigma\, a_{nb}(u'_{nb} - u'_e)$ on the righthand sideis neglected. This yields:

$$u'_e = d_e (p'_P - p'_E) \tag{2.34a}$$

$$v'_n = d_n (p'_P - p'_N) \tag{2.34b}$$

$$w'_t = d_t (p'_P - p'_T) \tag{2.34c}$$

where

$$d_e = \frac{A_e}{a_e - \Sigma\, a_{nb}} \tag{2.35a}$$

$$d_n = \frac{A_n}{a_n - \Sigma\, a_{nb}} \tag{2.35b}$$

$$d_t = \frac{A_t}{a_t - \Sigma\, a_{nb}} \tag{2.35c}$$

To obtain the pressure correction equation, it is necessary to integrate the continuity equation; thus,

$$(u_e - u_w)\Delta y \Delta z + (v_r - v_s)\Delta z \Delta x + (w_t - w_b)\Delta x \Delta y = 0 \tag{2.36}$$

Substituting all the velocity components given by the velocity-correction fomulas (2.32) and (2.34), yields the pressure correction equations.

$$a_P p'_P = a_E p'_E + a_W p'_W + a_N p'_N + a_S p'_S + a_T p'_T + a_B p'_B + b \tag{2.37}$$

where

$$a_E = d_e \Delta y \Delta z \tag{2.38a}$$

$$a_W = d_w \Delta y \Delta z \tag{2.38b}$$

$$a_N = d_n \Delta z \Delta x \tag{2.38c}$$

$$a_S = d_s \Delta z \Delta x \tag{2.38d}$$

$$a_T = d_t \Delta x \Delta y \tag{2.38e}$$

$$a_B = d_b \Delta x \Delta y \tag{2.38f}$$

$$a_P = a_E + a_W + a_N + a_S + a_T + a_B \tag{2.38g}$$

$$b = (u_w^* - u_e^*)\Delta y \Delta z + (v_s^* - v_n^*)\Delta z \Delta x + (w_b^* - w_t^*)\Delta x \Delta y \tag{2.38h}$$

It can be seen that the term b is essentially the left-hand side of the continuity equation (2.36) evaluated in terms of the starred velocities. If the starred velocities satisfy the continuity equation, b is zero, and no pressure correction is needed.

A step by step description of the solution procedure using the SIMPLE algorithm [37] is presented below,

1. Guess the pressure field p^*.
2. Solve the momentum equations to obtain u^*, v^* and w^*.
3. Solving the pressure correction equation (2.37) for p', by using u^*, v^* and w^* in the calculation of coefficients.
4. Calculate u, v, w from their starred values from equation (2.32) and equation (2.34). The pressure p is calculated from equation (2.31).
5. Solve the discretization energy equation for temperature.
6. Use the corrected pressure p as a new guessed pressure p^*, return to step 2, and repeat the whole procedure until a converged solution is obtained.

2.4.4 Validity and Accuracy of the Program

The algorithm was embodied in a computer program using FORTRAN-77 by Jianchiu Han [28] and modified later by the present author.

As a test of the validity of the program, the same problem treated by Mallinson & de Vahl Davis [39] (natural convection in an enclosure with one vertical wall heated and the opposite wall cooled), was re-calculated by Han [28]. Agreement within 2% in calculating the maximum velocity and the Nusselt number was obtained.

The heat transferred into and out of the system was calculated separately throughout the study, all the difference were within 5%. It is reasonable to believe that the accuracy of the program using the present mesh size in the calculation of Nusselt number is within about 5~10%. A discussion of consistency and accuracy test is presented in Appendix A.

2.5 DEFINITION OF NUSSELT NUMBER

The non-dimensionalized heat transfer coefficient, the Nusselt number, is defined as convection heat transfer coefficient over pure conduction heat transfer coefficient, representing how much the heat transfer is enhanced by convection. There are several ways to choose the heat transfer rate Q and the length H in defining Nu,

$$Nu = \frac{Q\ H}{A\ k\ \Delta T} \qquad (2.39)$$

For a thermosyphon, the heat transfer rate through all the walls of the tube is used. For a stable system, the heat in equals to the heat out. In the numerical calculation of heat transfer rate Q, a two-node formula was used for the local temperature gradient. The area A is chosen as half of the total wall area of the tube,

$$A = SL + LD + DS \tag{2.40}$$

In order to compare with the pure conduction value, the temperature difference ΔT is taken as

$$\Delta T = T_H - T_L \tag{2.41}$$

And the length H is chosen as the distance from the heated wall to the cooled wall. For a radial thermosyphon, H = L; for a eccentric or concentric thermosyphon, H = S.

3. RADIAL THERMOSYPHON

The behaviour of the radial thermosyphon shown in Figure 2.1 will be studied in this chapter. The effects of Rayleigh number, Ekman number, Prandtl number, acceleration ratio and eccentricity on the heat transfer rate and flow pattern will be explored by using the Nusselt number curve and primary and secondary flow profiles.

In this case, A_x in those governing equations is fixed to 1, and A_y is fixed at 5. Due to the anticipated characteristics of the flow, a non-uniform $15\times 51\times 15$ mesh network was used with dense grid points applying to the boundaries near the walls at the X and Z directions.

3.1 THE EFFECT OF RAYLEIGH NUMBER

In this section, the effect of Rayleigh number on the heat transfer rate and flow pattern will be studied. All other parameters will be fixed: $Ek=5\times 10^{-3}$, $Pr=100$, $R_g=100$, $R_l=100$.

Because the $R_g=\Omega^2(\mathcal{R}+L)/g$ is 100, the influence of gravity on the system is negligible. The body force is the centrifugal force only. Since $R_l=\mathcal{R}/L$ is 100, the body force created by rotation is almost uniform over the whole tube. $Pr=100$ implies a relatively viscous fluid. The Ekman number $Ek=\nu/\Omega D^2$ is chosen to be 5×10^{-3} almost the lowest value for which we can obtain converged solution.

It has been noted that the thermal and hydrodynamic regimes of the tubular thermosyphon are reflected in the plot of Nusselt number against Rayleigh number. Figure 3.1 shows such a plot. It is evident that convection has a negligible effect on heat transfer rate for sufficiently low Rayleigh numbers, but convection eventually appears as the Rayleigh number increases beyond $Ra=10^4$. The results confirm the expectation that, beyond the critical (conduction maximum) Rayleigh number, the behaviour of the system spanned two established regimes: impeded and boundary layer. It seems that the impeded regime lies in a very short range, and then a boundary layer regime develops.

A previous stationary vertical thermosyphon result [17] is also plotted in Figure 3.1; in which the $\Omega^2(\mathcal{R}+L)$ in the definition of Ra is replaced by g. It is evident that the rotating thermosyphon does not give a significantly higher heat transfer rate for the same Rayleigh number, at least not for the conditions examined here near $Ek=5\times10^{-3}$. This finding is contrary to the expectation that Coriolis force would increase the heat transfer rate by increasing the secondary flow. Inspection of the governing equations reveals that the Coriolis acceleration does increase the secondary flow (the flow in the Z direction), but at the same time it reduces the primary flow (the flow in the Y direction). The two processes roughly balance each other.

Figure 3.2 shows the velocity field in a longitudinal horizontal plane (the mid x plane perpendicular to the rotating axis) for $Ra=5\times10^4$. As in a vertical thermosyphon, this reveals that the deep flow, i.e. near the closed ends,

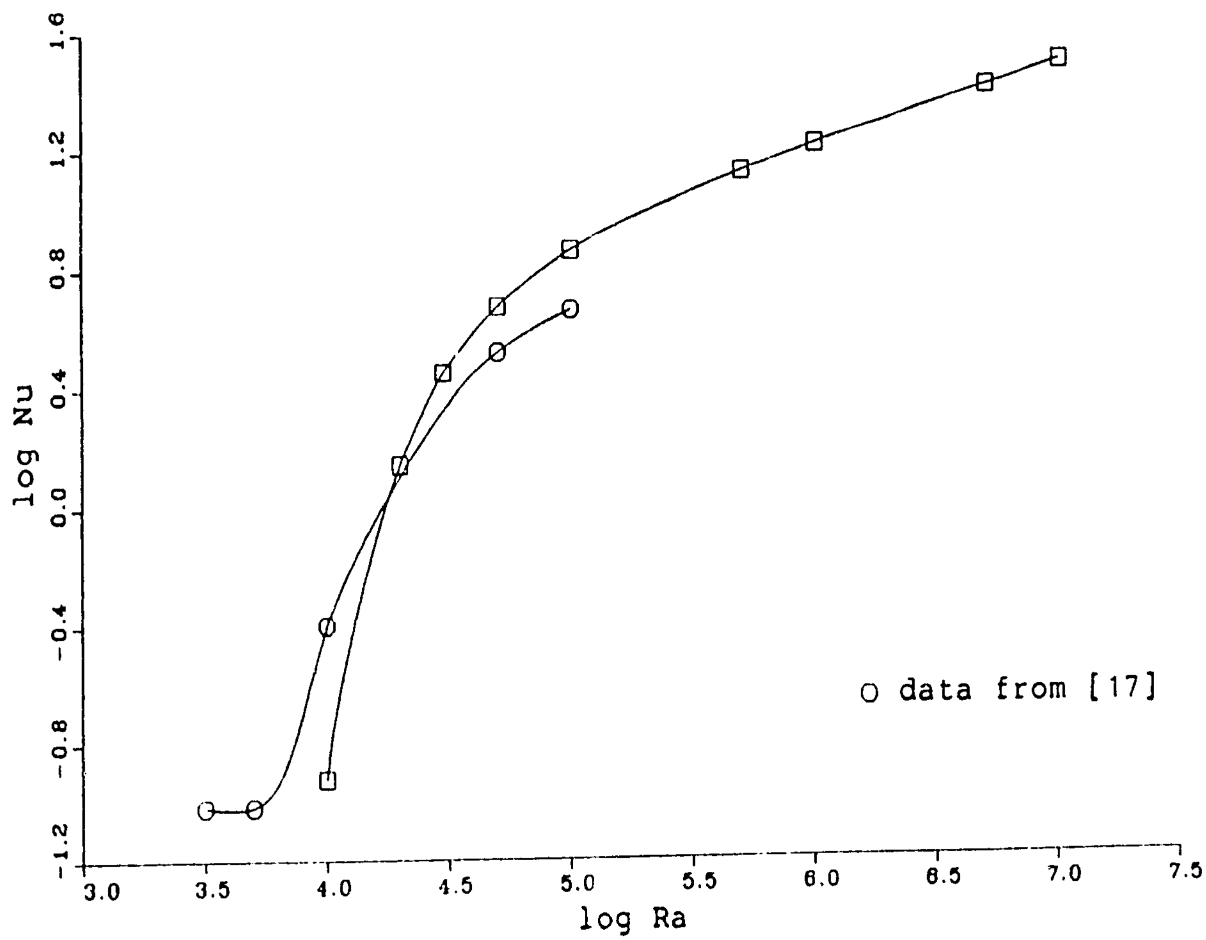

Figure 3.1 Effect of Rayleigh number on heat transfer in a radial thermosyphon at $Ek=5\times10^{-3}$, $Pr=100$, $R_g=100$, $R_l=100$.

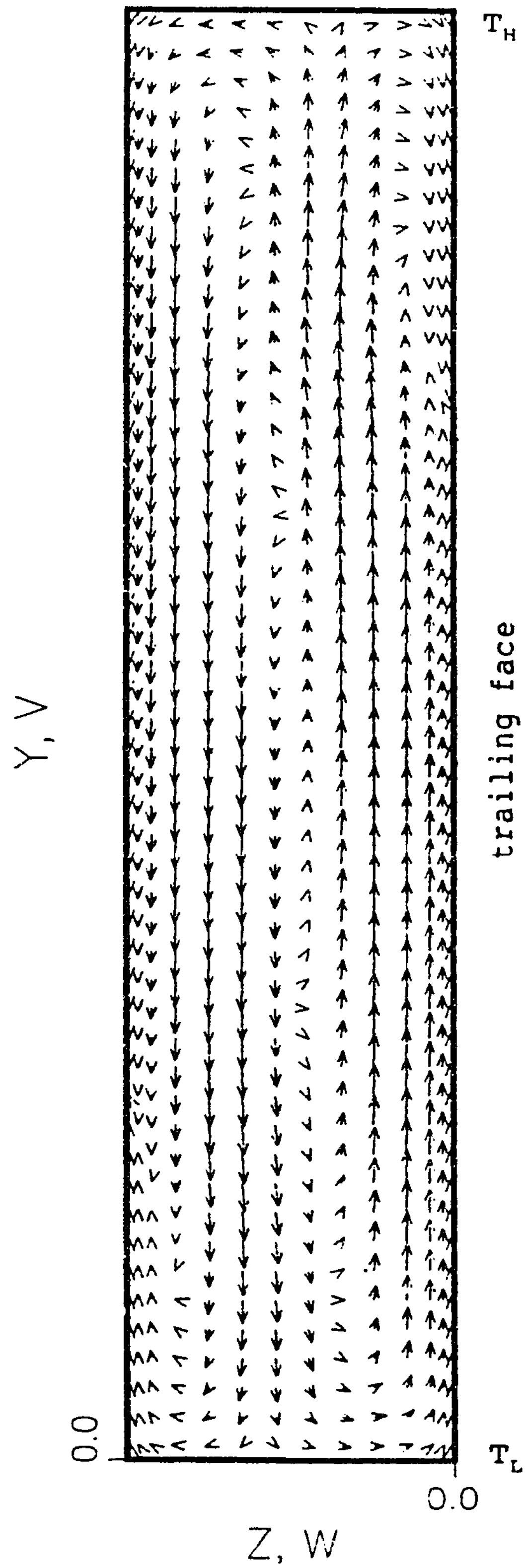

Figure 3.2 Velocity field in mid plane of rotation x=0.5 for Ra=5×10^4 at Ek=5×10^{-3}, Pr=100, R_g=100, R_l=100.

has an annular refluent form. In the mid length region, however, the flow is evidently bifilamental with hot fluid moving radially inward over the leading face supplying the core flow in the cooled section while cold fluid moving radially outward over the trailing face to supply the heated section core flow. The bifilamental central region occupies about half of the tube length.

Figure 3.3 illustrates the development of the axial velocity profile for the same conditions used in Figure 3.2. It is immediately obvious from this figure that the bifilamental flow gradually develops from the annular flow near the ends; and it is equally obvious that the annular flow does not extend around all four sides of the tube, as in a vertical thermosyphon. The Coriolis acceleration has flattened the flow, making it look almost two-dimensional. A similar flattening of the velocity profiles has been reported by Kheshgi and Scriven [40] and Speziale [41] for forced flow in rotating rectangular ducts.

The transverse velocity field is provided in Figure 3.4. This secondary motion is caused solely by Coriolis acceleration. The velocity vectors are almost all in the Z direction, which has the Coriolis force component. Near the closed (cooled) end, the flow splits at the centre on the leading face and begins moving towards the top and bottom walls. Then the fluid turns around moving towards the trailing face. On planes progressively further from the end, two pairs of vortices appear and develop gradually. At the

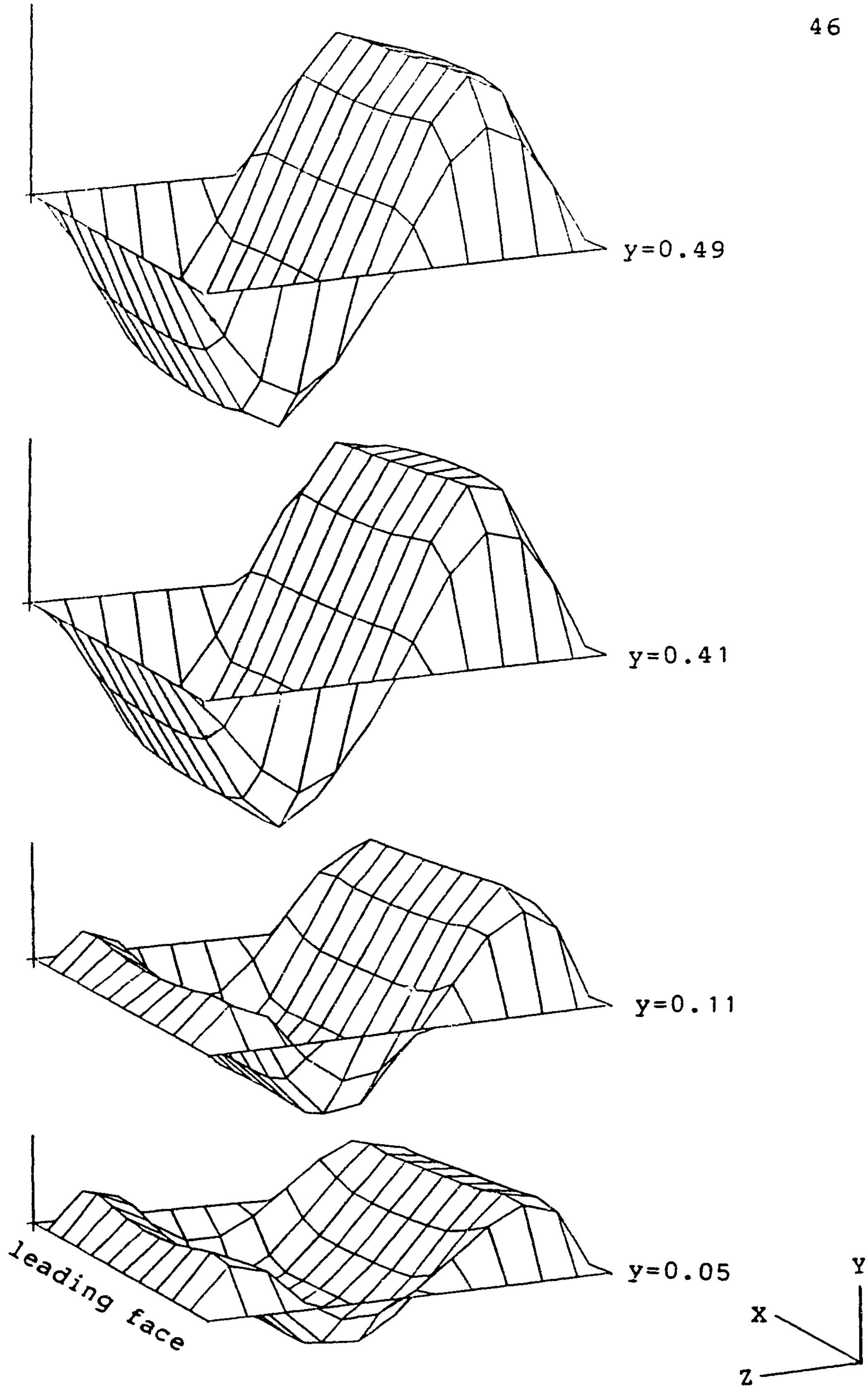

Figure 3.3 Development of the axial velocity profile for $Ra=5\times10^4$ at $Ek=5\times10^{-3}$, $Pr=100$, $R_g=100$, $R_1=100$.

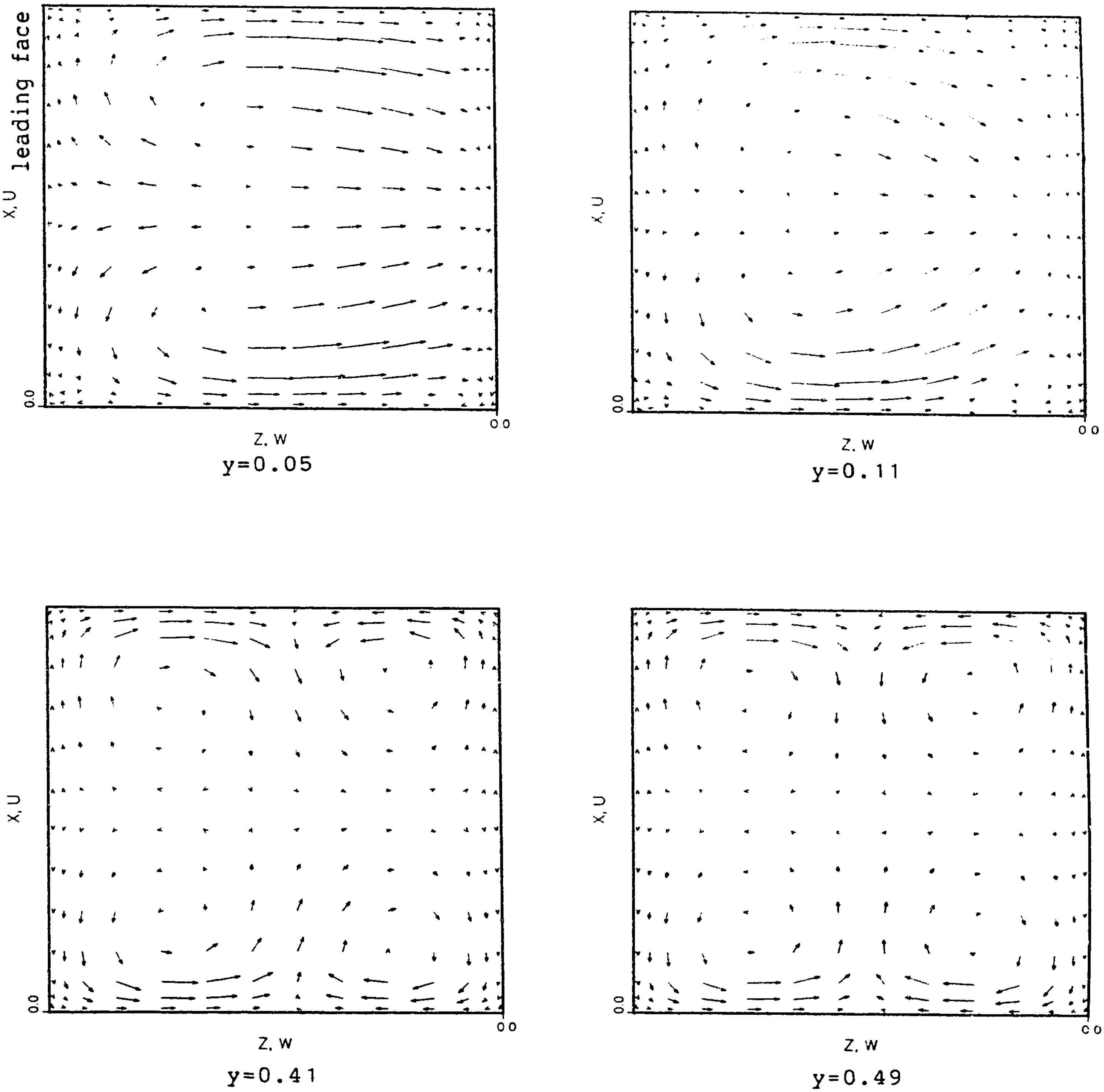

Figure 3.4 Development of the transverse velocity field for $Ra=5\times10^{4}$ at $Ek=5\times10^{-3}$, $Pr=100$, $R_g=100$, $R_l=100$.

mid length plane, there are two symmetric pairs of vortices mainly in the Ekman layers, the regions near the top and bottom walls. This behaviour is reminiscent of that observed in the highly tilted thermosyphons [28,29,30], and is also reported for forced flow in rotating rectangular channels [40,41].

The ratio of the magnitudes of main flow velocity to secondary flow velocity is found to be about one, indicating that the main flow and the secondary flow have the same importance on heat transfer. The vortical secondary flow continuously turns the outside fluid in and the inside fluid out, making the four side walls heat transfer up to about 80% of the total, as discussed later.

Figures 3.5, 3.6, 3.7 show the velocity at the longitudinal mid x plane, the axial velocity profile and the transverse velocity field for $Ra=2\times10^4$. Basically the flow pattern is the same as for $Ra=5\times10^4$. Considering the scale here is half the scale for $Ra=5\times10^4$ we conclude that the flow here is much weaker than the flow at $Ra=5\times10^4$ as suggested by the Nu~Ra plot in Figure 3.1. The Nusselt number is about one third of that at $Ra=5\times10^4$. It is interesting to note that the side wall heat transfer jumps to 90% of the total, indicating that for lower Rayleigh numbers, the secondary flow induced by the Coriolis force plays an even bigger relative role.

For quite high Rayleigh numbers, $Ra=10^7$, the longitudinal velocity field at the mid x plane, axial

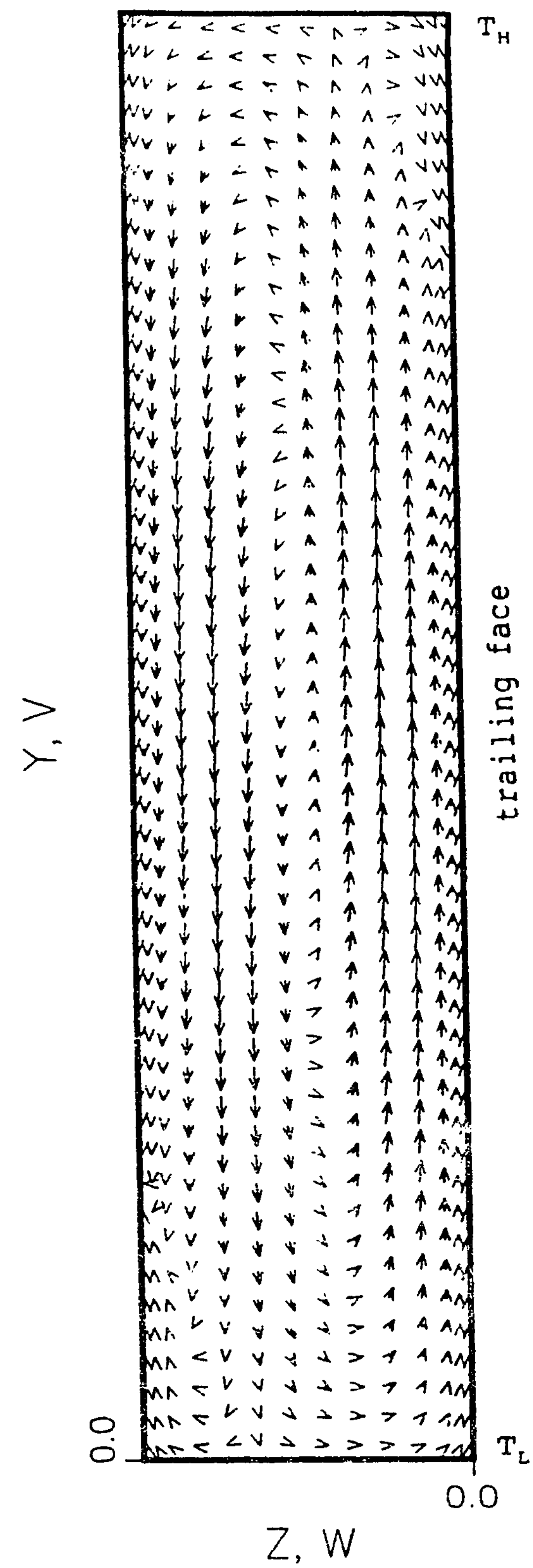

Figure 3.5 Velocity field in mid plane of rotation x=0.5 for Ra=2×10^4 at Ek=5×10^{-3}, Pr=100, R_g=100, R_1=100.

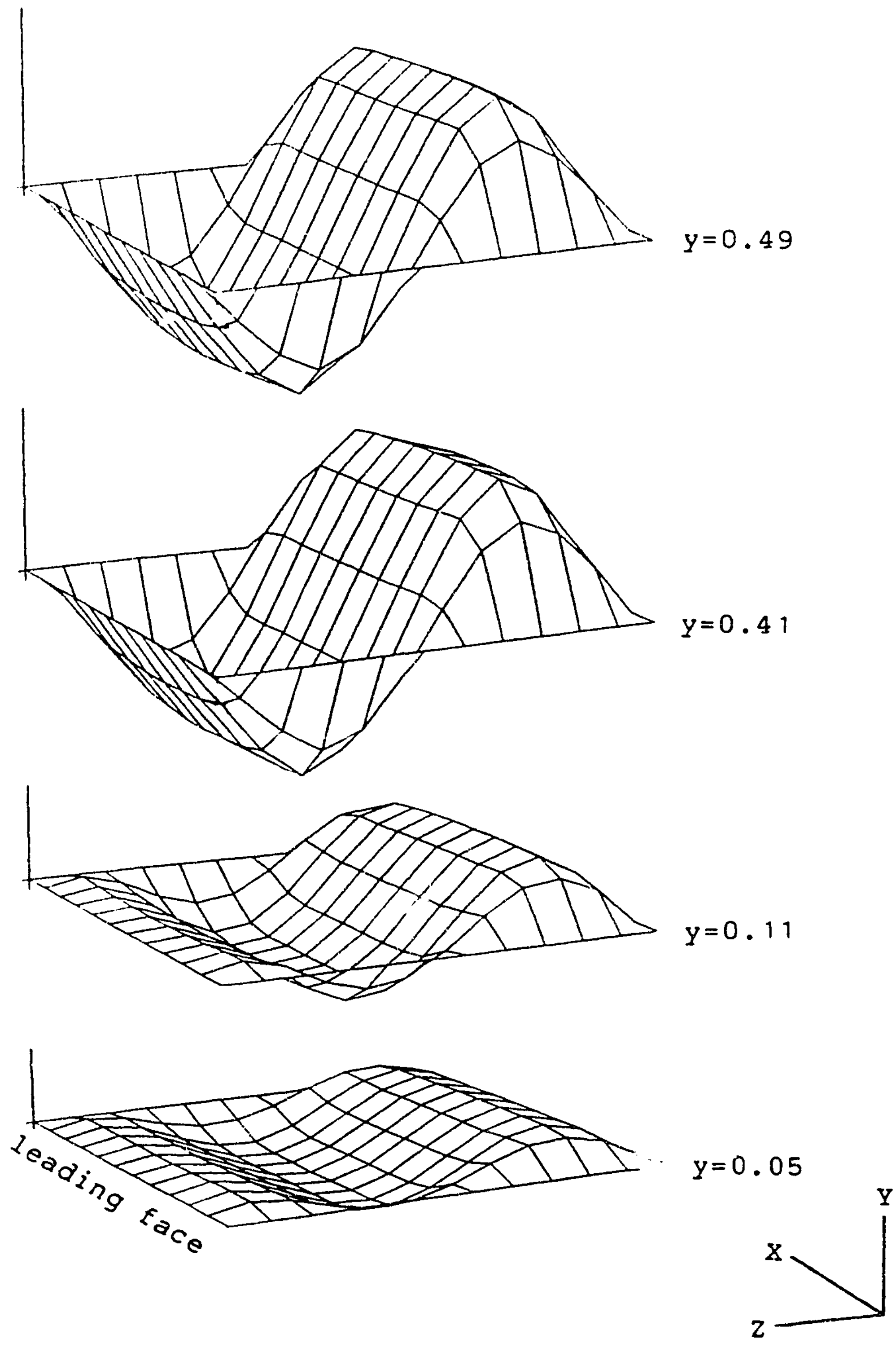

Figure 3.6 Development of the axial velocity profile for $Ra=2\times10^4$ at $Ek=5\times10^{-3}$, $Pr=100$, $R_g=100$, $R_1=100$.

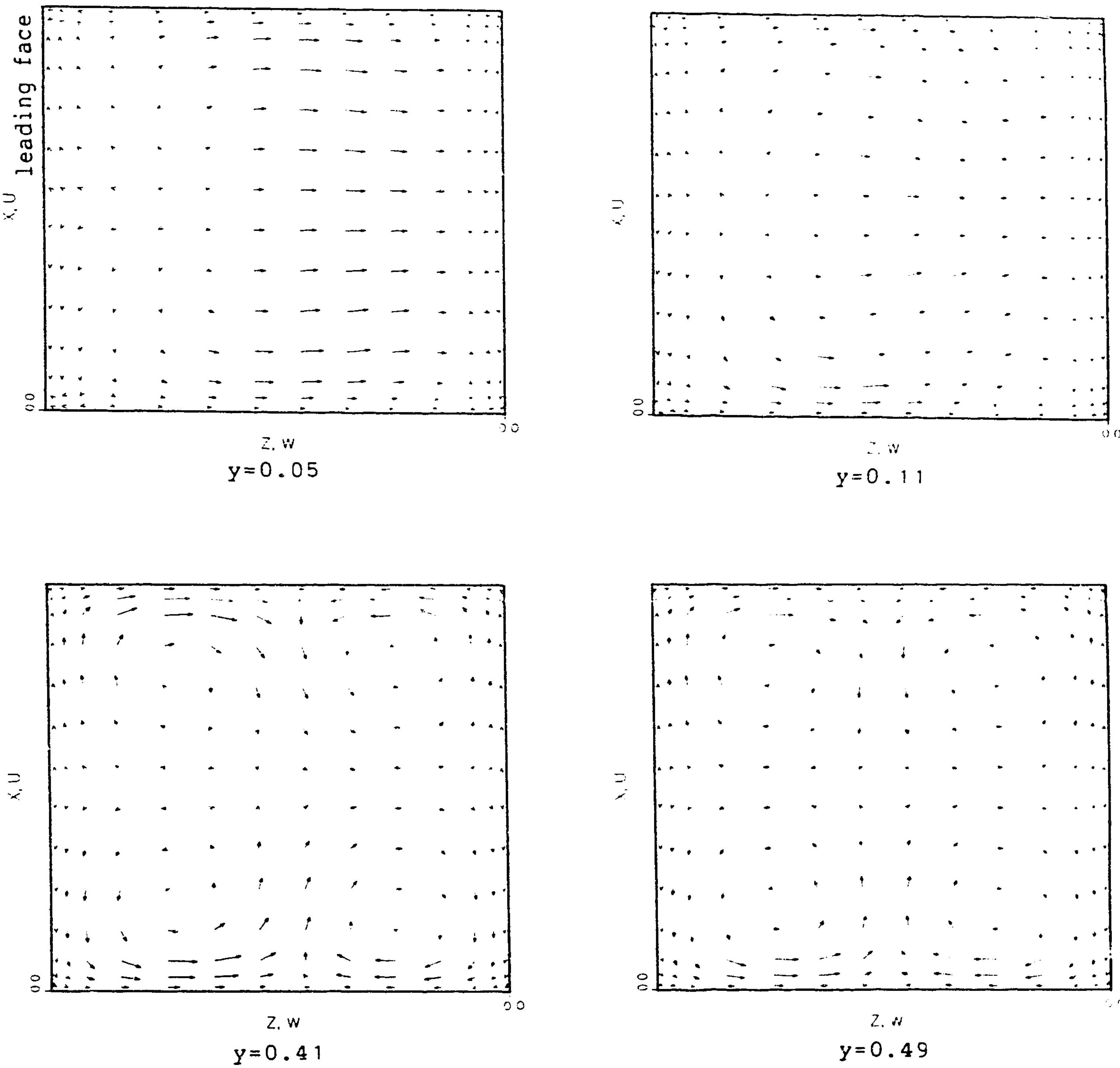

Figure 3.7 Development of the transverse velocity field for $Ra=2\times10^{4}$ at $Ek=5\times10^{-3}$, $Pr=100$, $R_g=100$, $R_l=100$.

velocity profile v and transverse velocity field are given in Figures 3.8, 3.9 and 3.10, respectively. The basic flow patterns are maintained, while transition to another flow pattern appears. The bifilamental flow at the mid length shrinks to about only one third of the tube length, and begins to [illegible] through to form a vortex at the mid length region. By looking at the axial velocity profile v in Figure 3.9, it is evident that the symmetry about the mid X plane is broken; and near the top and the bottom of the tube (that is within the Ekman layers), the axial velocity shows maxima. The interesting maxima were also reported by Kheshgi and Scriven [40] and Speziale [41] for forced convection in rotating channels. The symmetry about the mid x plane is also lost in the transverse secondary flow field. Near the end region, the Ekman layer is more obvious; and in the mid length region, a complex flow pattern appears. This also indicates a transition from this flow pattern to another more complex, probably unstable flow pattern.

The details of the heat transfer contribution attributable to each of the five faces are shown in Figure 3.11. As Ra increases, the heat transfer through the leading face contributes more to the total heat transfer rate. This is consistent with the finding that the refluent flow at the end extends as Ra increases. The heat transfer through the end wall contributes about 20% or less for most Rayleigh numbers; except at $Ra=10^4$, where the end/total ratio is 76%.

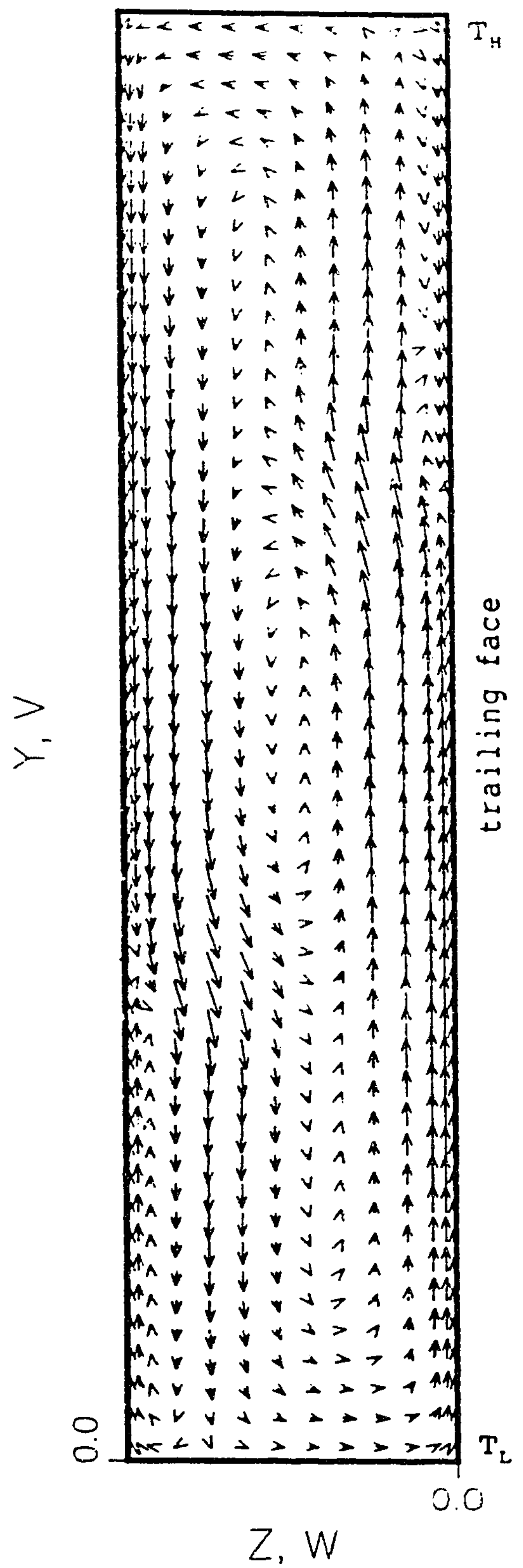

Figure 3.8 Velocity field in mid plane of rotation x=0.5 for Ra=10^7 at Ek=5×10^{-3}, Pr=100, R_g=100, R_l=100.

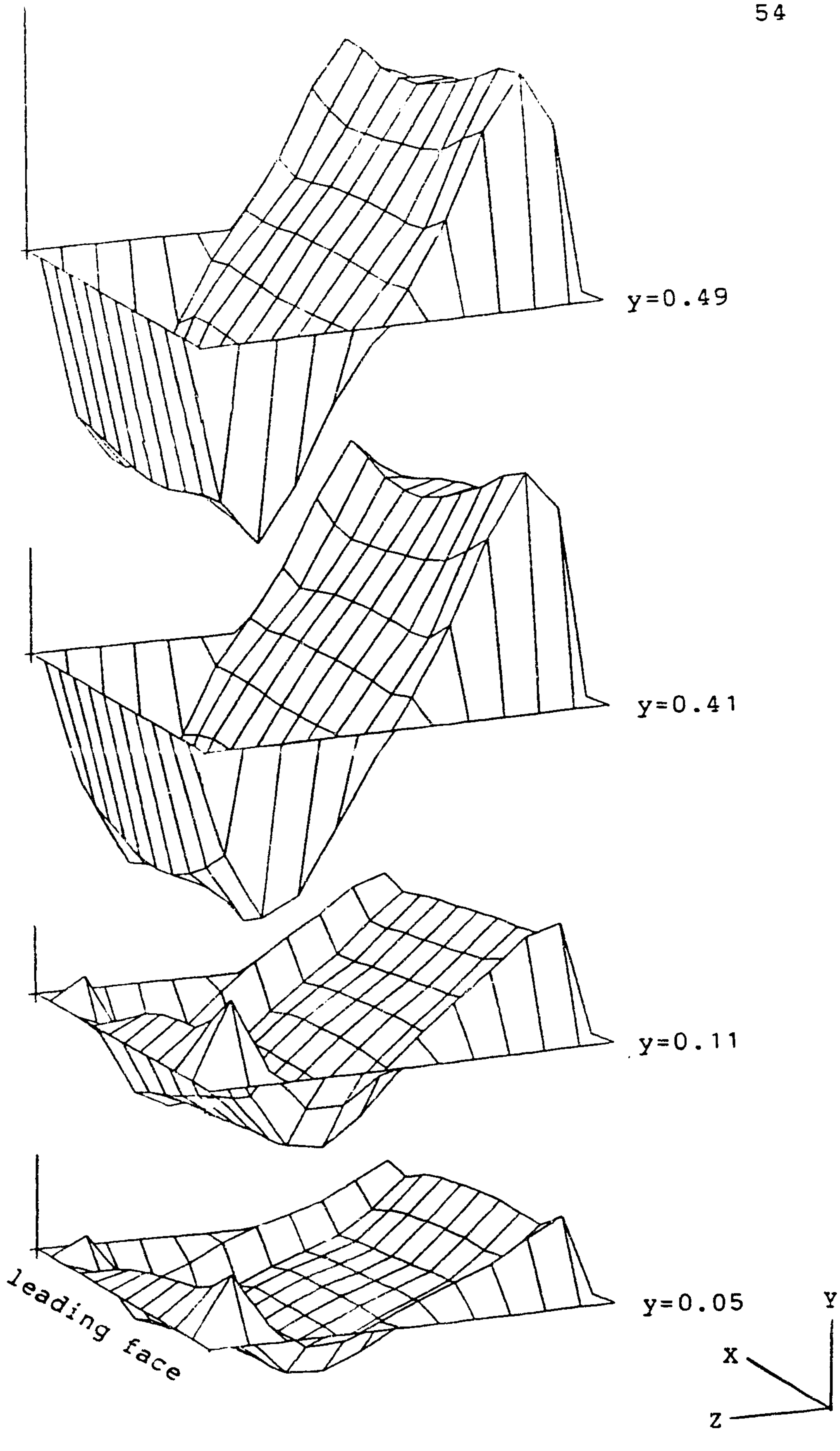

Figure 3.9 Development of the axial velocity profile for $Ra=10^7$ at $Ek=5\times10^{-3}$, $Pr=100$, $R_g=100$, $R_l=100$.

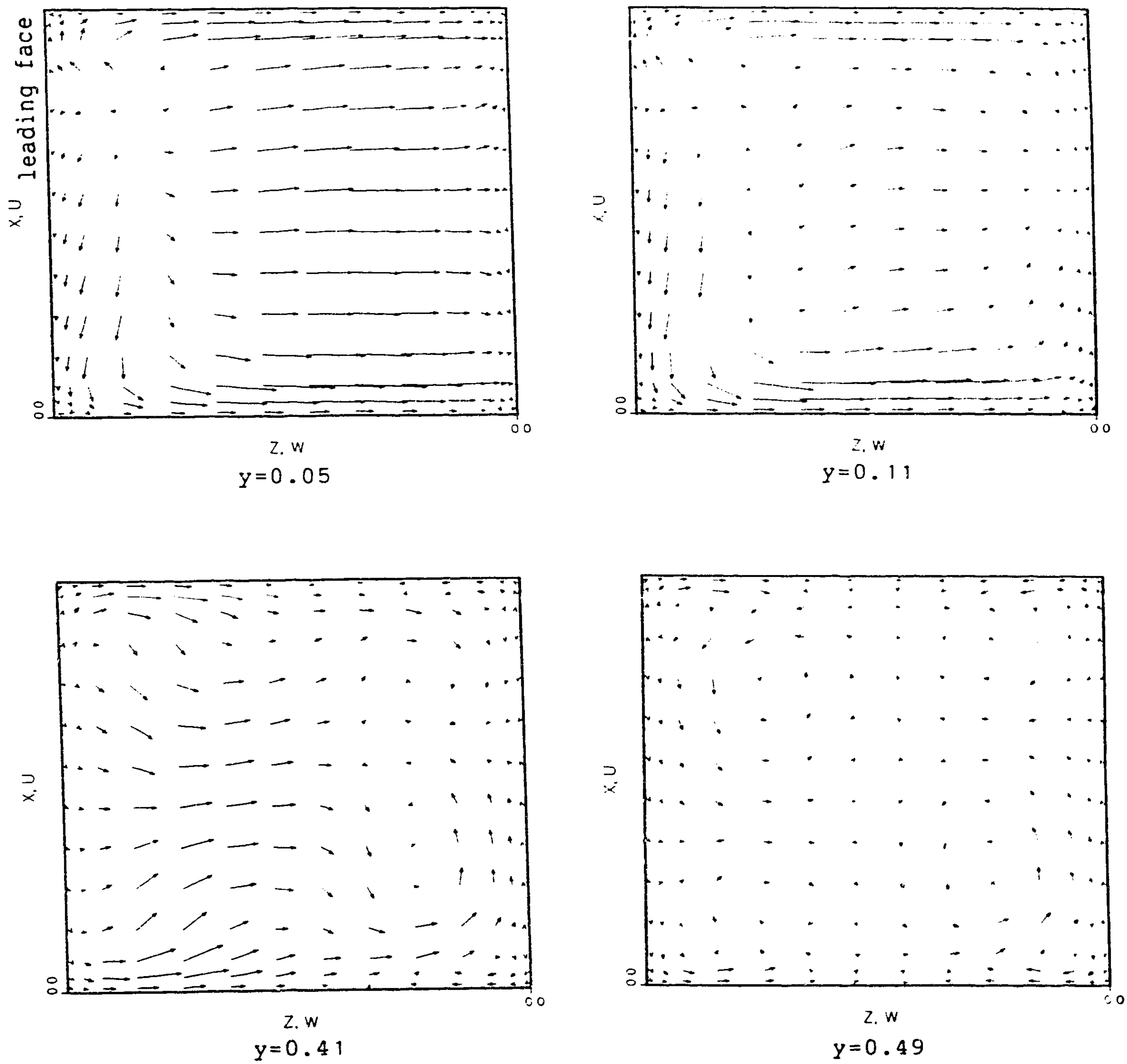

Figure 3.10 Development of the transverse velocity field for $Ra=10^7$ at $Ek=5\times10^{-3}$, $Pr=100$, $R_g=100$, $R_1=100$.

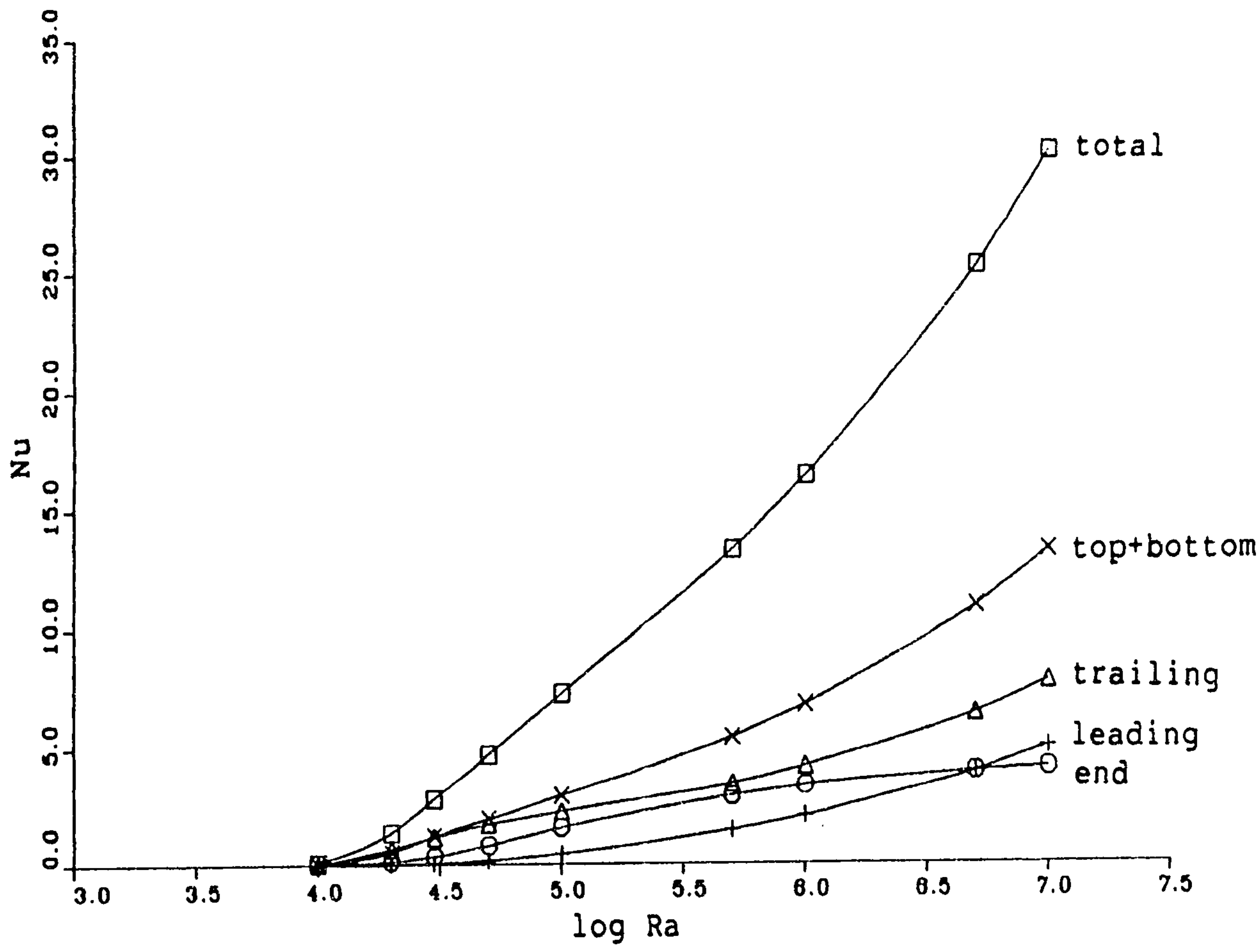

Figure 3.11 Components of the heat transfer rate at $Ek=5\times10^{-3}$, $Pr=100$, $R_g=100$, $R_l=100$.

3.2 THE EFFECT OF EKMAN NUMBER

The Ekman number, defined as $Ek=\nu/\Omega D^2$, represents the relative importance of the viscous force in relation to the Coriolis force. The effect of Ek will be tested here with other parameters fixed. A Rayleigh number of $Ra=5\times10^4$ will be chosen as a reference value, and Pr=100, $R_g=100$, $R_l=100$ are the same as in section 3.1.

It might be expected that as the Ekman number decreases, the heat transfer rate should increase in the laminar flow region; that is the Coriolis effect would increase. This was not always true, as illustrated by Figure 3.12. As the Ekman number decreases below 1, indicating a faster rotating speed and higher Coriolis force, the Nusselt number increases first, reaches a maximum at about $Ek=10^{-2}$, and then drops quickly. Below about $Ek=2\times10^{-3}$, it was difficult to get a stable, converged solution. Some preliminary probing beyond this point suggests that the system may break from the present flow pattern to several "cats eye' cells in the main flow; the heat transfer rate then appears to jump to a very much higher value.

It seems that in order to fully describe the thermal and hydrodynamic regimes of a rotating thermosyphon, in addition to the Nu~Ra curve, the plot of Nu~Ek is also needed. The flow regime is thus a function of both Ra and Ek. Generally speaking, as the Ekman number decreases, the Coriolis force plays a bigger role. At the beginning, the heat transfer rate increases through secondary circulation

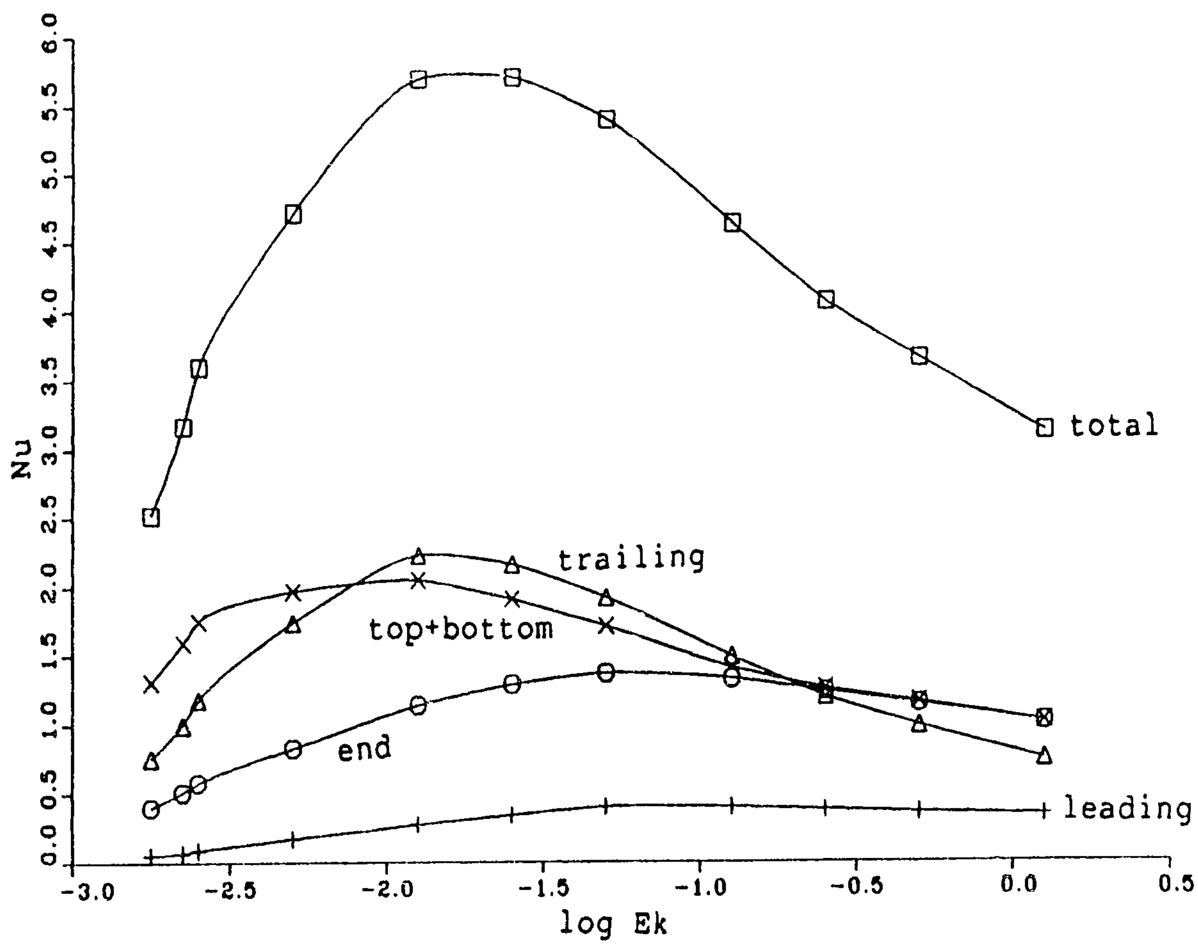

Figure 3.12 Effect of Ekman number on heat transfer at $Ra=5\times10^4$, $Pr=100$, $R_g=100$, $R_l=100$.

as Ek decreases, while at the same time, the main flow is retarded. When these two processes balance each other, the heat transfer rate reaches a maximum. For this regime, we might call it Coriolis-enhanced regime. As Ek decreases further, the heat transfer rate decreases quickly due to reduced main flow. We might name this regime as Coriolis-impeded.

As Ekman number increase from $Ek=5\times10^{-3}$ to $Ek=2.5\times10^{-2}$, the same flow pattern is maintained, as shown in Figure 3.13. That is a bifilamental flow at the mid length region with an annular refluent flow at the two ends. The refluent main flow near the ends covers all four sides of the tube as shown in Figure 3.14; the Coriolis effect is obvious in the secondary flow as indicated in Figure 3.15. Two pairs of vortices are obtained at the mid length plane, and heat transfer rate reaches a maximum. At this Ekman number and below, the majority of viscous shear is in the Ekman layers along the top and bottom walls.

For $Ek=5\times10^{-1}$, the velocity field in the longitudinal horizontal plane is shown in Figure 3.16. The bifilamental flow shrinks to about two fifth of the total length, and the refluent end flow extends and is symmetric about the mid z plane. Figures 3.17 and 3.18 show the main flow profile and the transverse secondary flow. The main flow profile is quite similar to that observed in stationary thermosyphons tilted from the vertical [17]. The refluent main flow extends more around all four sides of the tube, and the

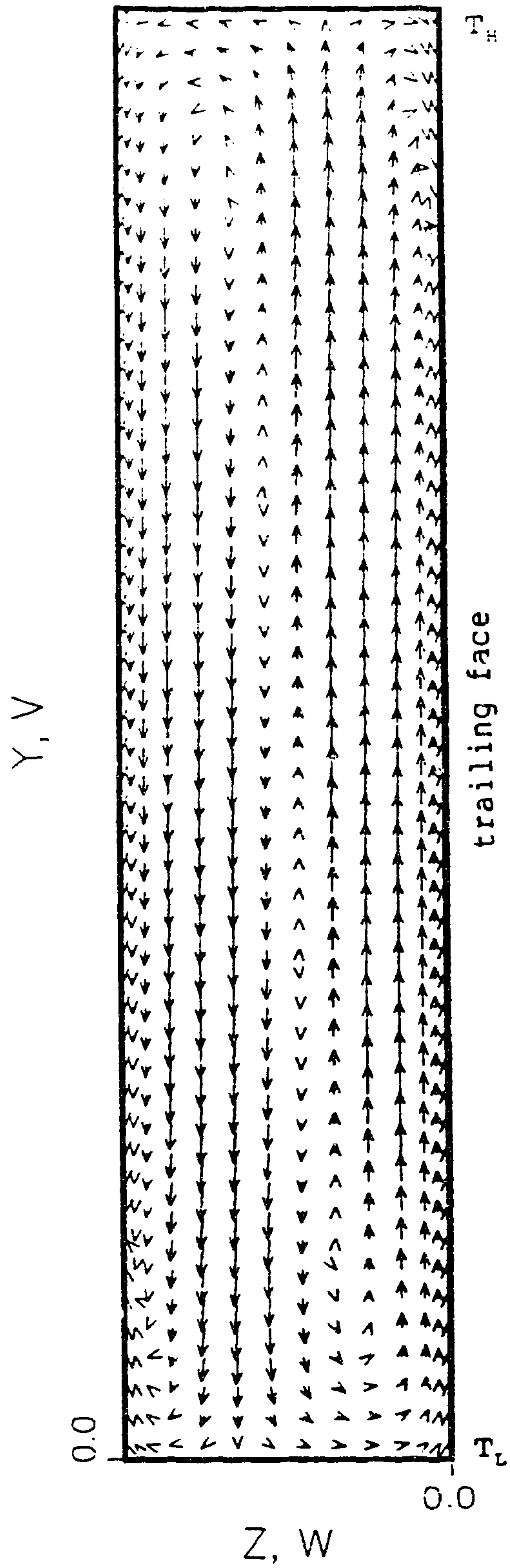

Figure 3.13 Velocity field in mid plane of rotation x=0.5 for Ek=2.5×10^{-2} at Ra=5×10^{4}, Pr=100, R_g=100, R_l=100.

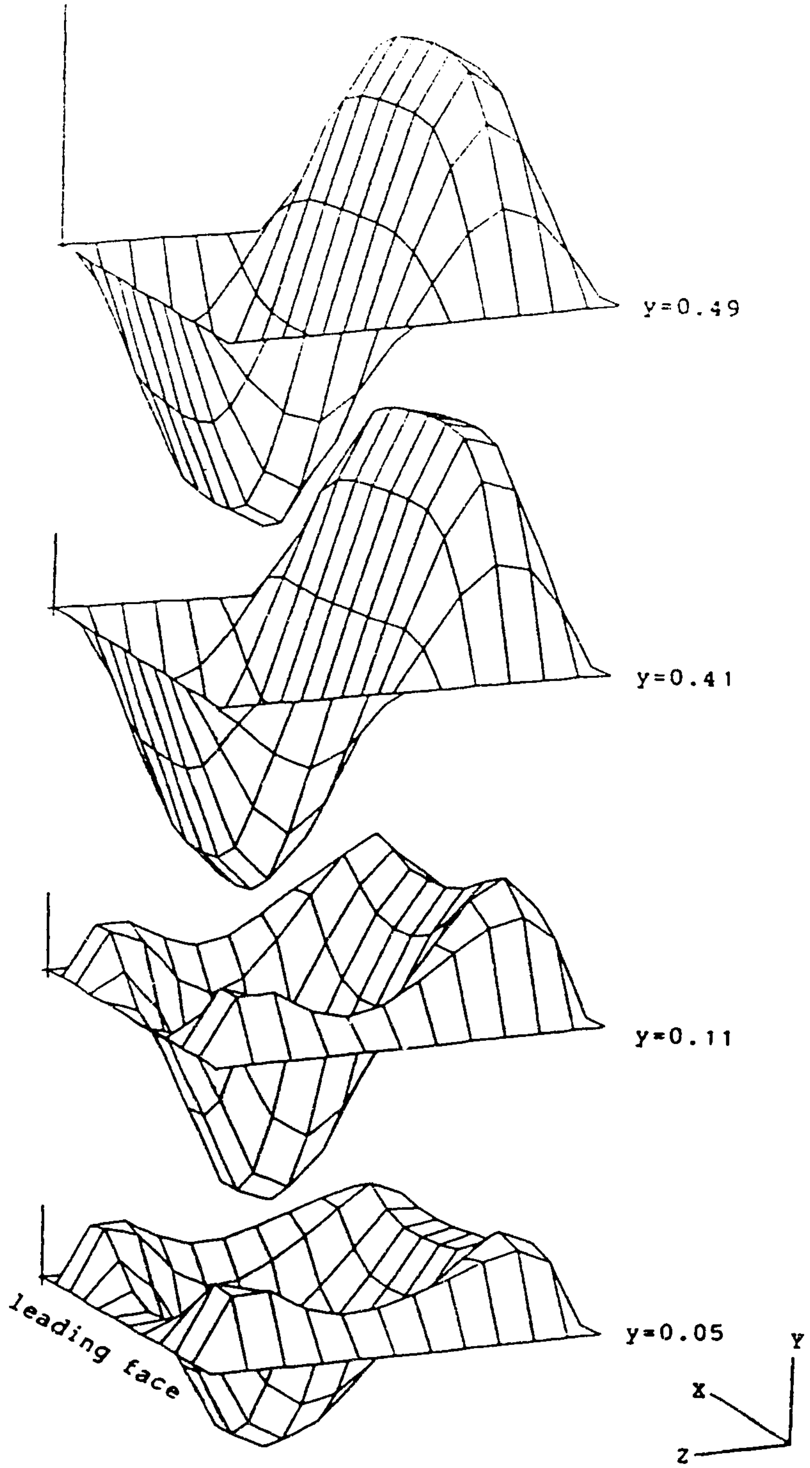

Figure 3.14 Development of the axial velocity profile for $Ek=2.5\times10^{-2}$ at $Ra=5\times10^{4}$, $Pr=100$, $R_g=100$, $R_l=100$.

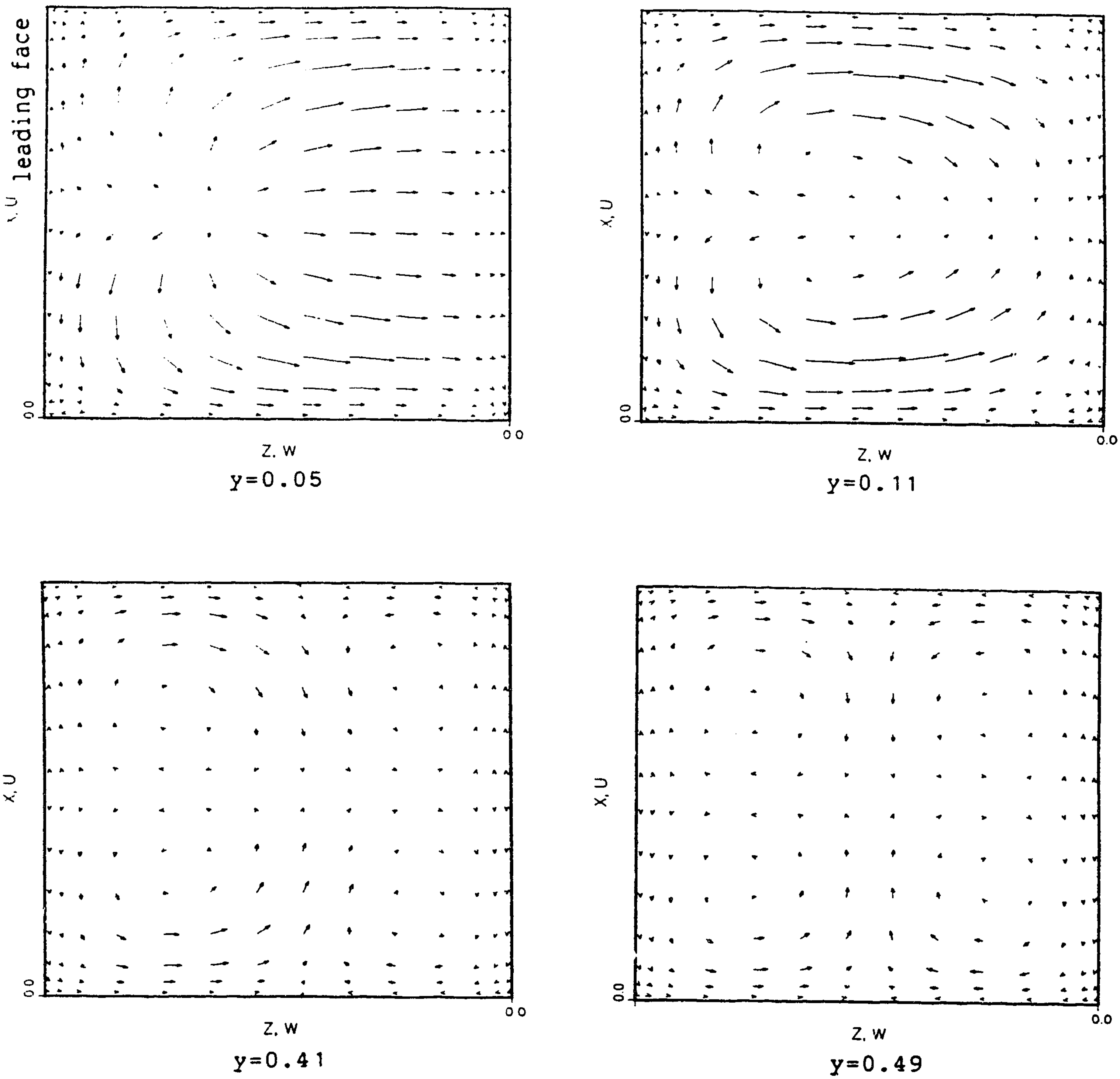

Figure 3.15 Development of the transverse velocity field for $Ek=2.5\times10^{-2}$ at $Ra=5\times10^{4}$, $Pr=100$, $R_g=100$, $R_1=100$.

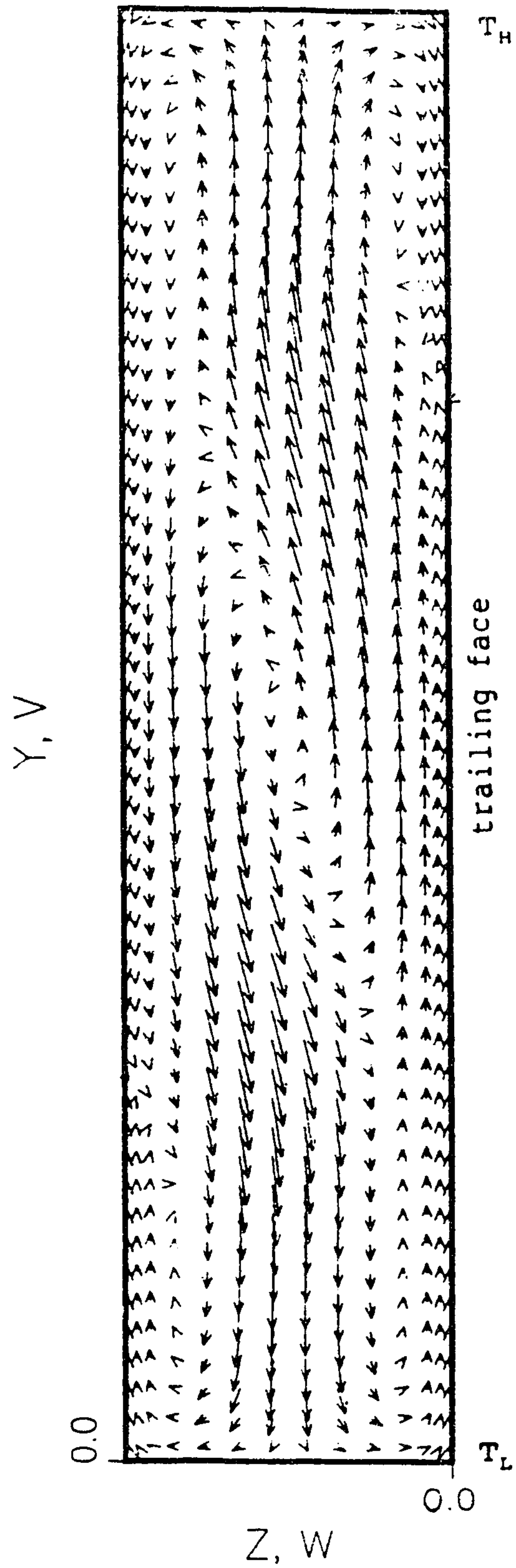

Figure 3.16 Velocity field in mid plane of rotation x=0.5 for $Ek=5\times10^{-1}$ at $Ra=5\times10^{4}$, $Pr=100$, $R_g=100$, $R_l=100$.

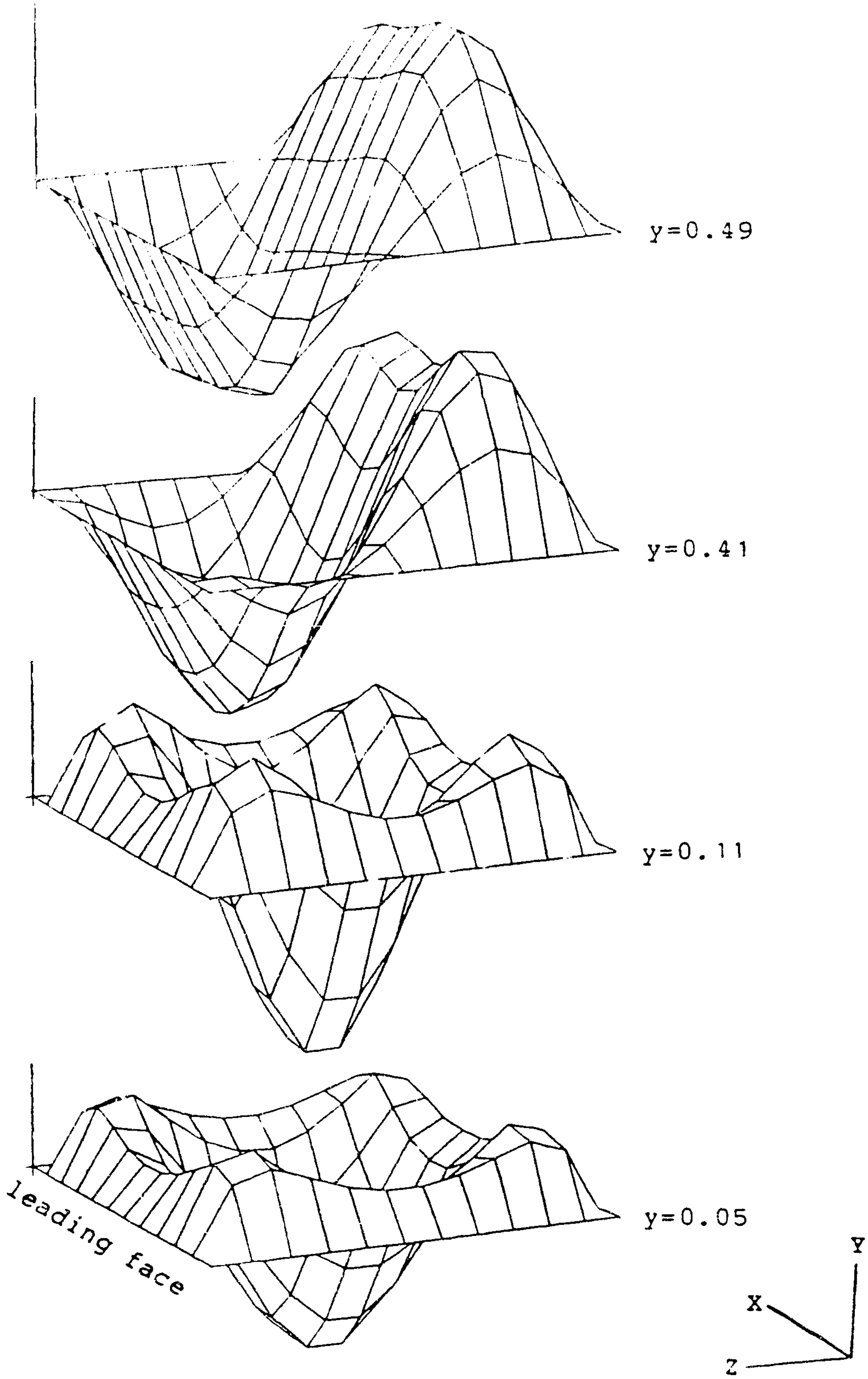

Figure 3.17 Development of the axial velocity profile for $Ek=5\times10^{-1}$ at $Ra=5\times10^{4}$, $Pr=100$, $R_g=100$, $R_l=100$.

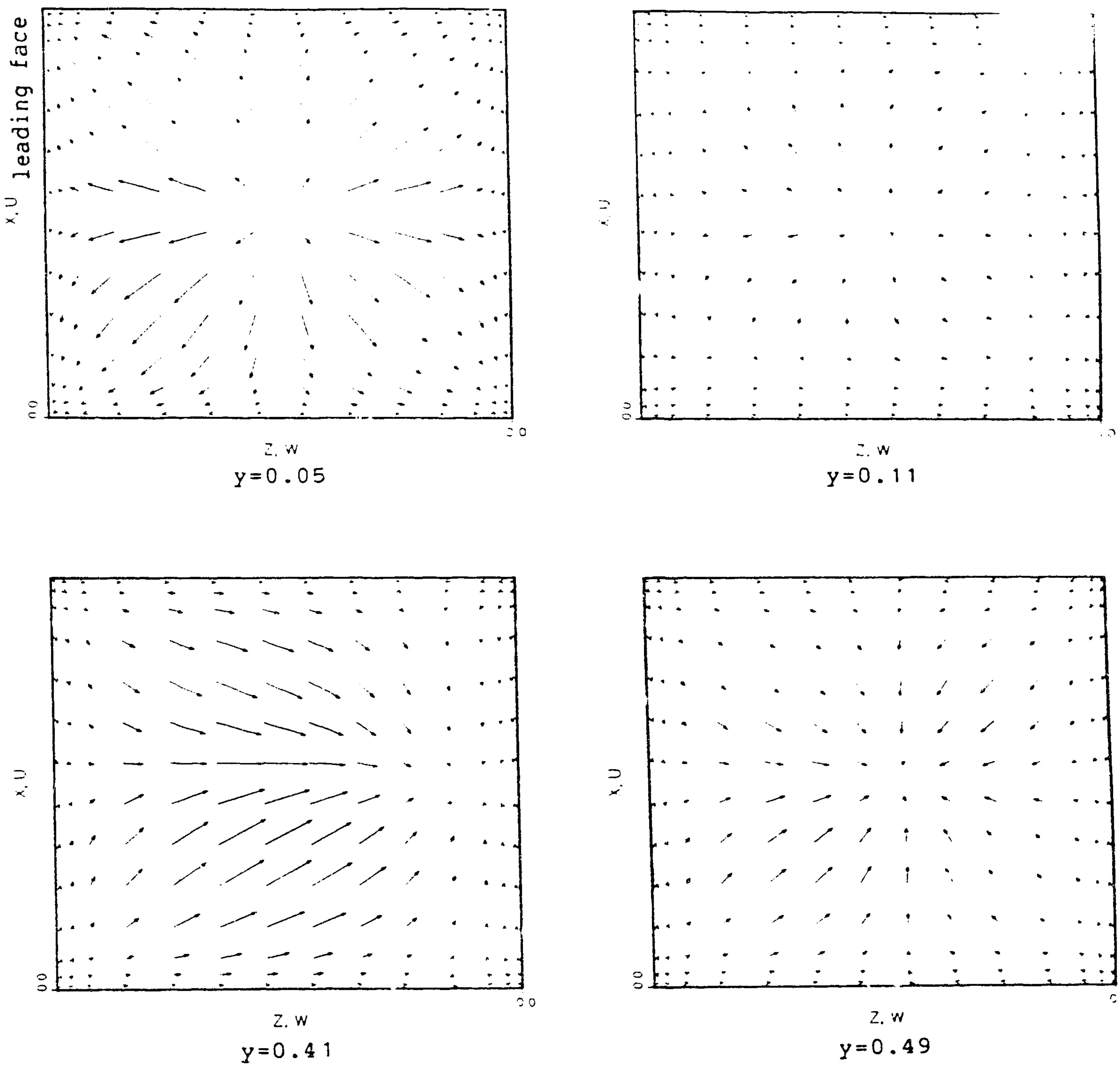

Figure 3.18 Development of the transverse velocity field for $Ek=5\times10^{-1}$ at $Ra=5\times10^{4}$, $Pr=100$, $R_g=100$, $R_l=100$.

Coriolis effect is imperceptible in the secondary flow.

3.3 THE EFFECT OF PRANDTL NUMBER

The Prandtl number, ν/κ, represents the relative diffusion rates of momentum and heat in the fluid. It is well known that the Prandtl number has little effect on Nusselt number in natural convection when Pr>1.

For $Ra=5\times10^4$, $Ek=5\times10^{-3}$, $R_g=100$, $R_i=100$, the curve of Nusselt number as a function of Prandtl number is given in Figure 3.19. The Nusselt number is almost constant at 4.7 for Prandtl numbers from 1 to 100. It drops to about 1 at Pr=0.01. Compared to Nu=0.[illegible] for pure conduction, it is still a significant heat transfer rate.

The Nusselt number may be defined as the convection heat transfer coefficient over the conduction heat transfer coefficient, indicating how much heat transfer may be attributed to convection. For small Prandtl numbers, representing a high thermal conductivity, the increase on heat transfer rate due to convection is relatively small.

How the Prandtl number alters the flow pattern is hard to predict. Figure 3.20 shows the velocity field in the longitudinal mid x plane for Pr=0.01. Considering the scale is fifteen times that in Figure 3.2 for Pr=100, it is evident that the flow is very vigorous. The bifilamental flow in the central region is greatly extended, and the annular refluent flow at the two ends shrinks to only one fifth of the length. The whole flow field looks quite close

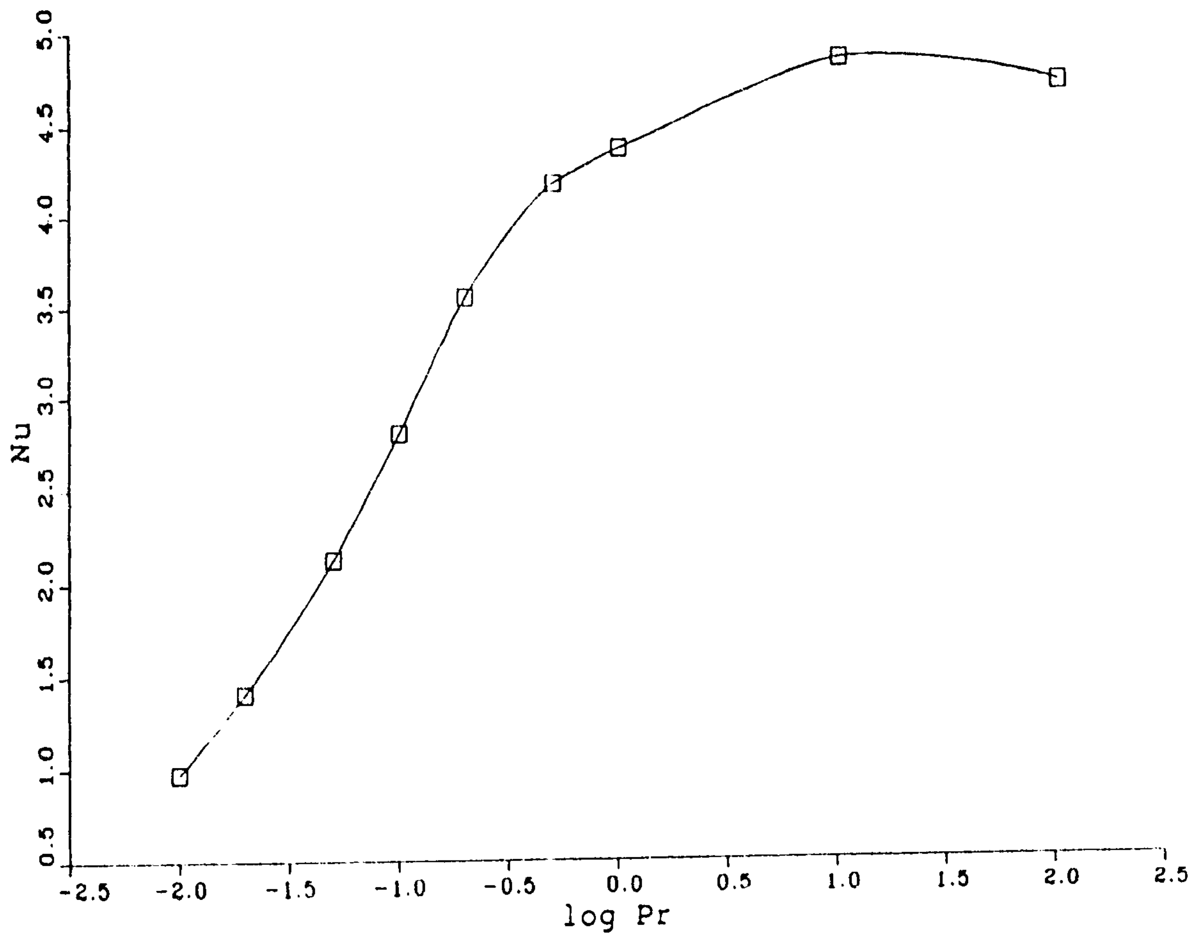

Figure 3.19 Effect of Prandtl number on heat transfer at $Ra=5\times10^{4}$, $Ek=5\times10^{-}$[illegible], $R_g=100$, $R_l=100$.

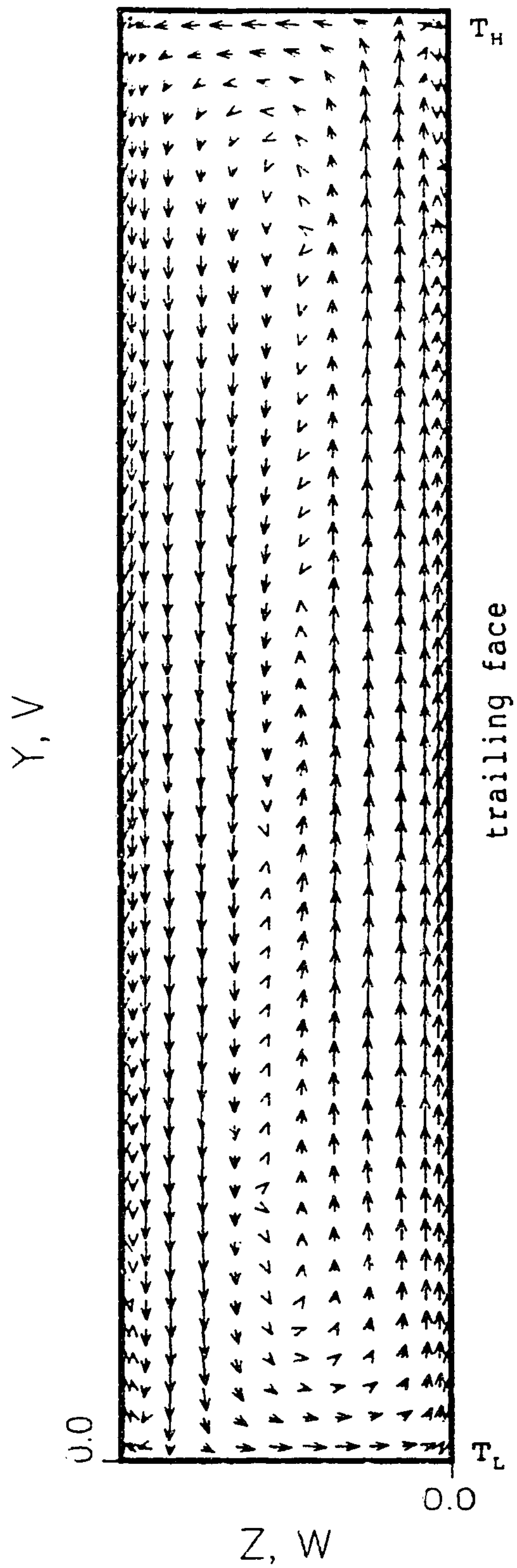

Figure 3.20 Velocity field in mid plane of rotation x=0.5 for Pr=0.01, at Ra=5×10^4, Ek=5×10^{-3}, R_g=100, R_l=100.

to uni-cellular flow found in the stationary horizontal thermosyphon.

Small viscosity also represents a low rotation speed for a constant Ekman number, implying that the influence of Coriolis effect will be smaller. Figure 3.21 and Figure 3.22 represent the main flow profile and the secondary flow, respectively. The flattened, two-dimensional shape of the main flow found before is barely detectable, especially in the central region. Two maxima appear in the main flow profile near the end, Basically the secondary flow is the same as in Figure 3.4 caused by Coriolis force, except at the mid length region, the flow is not symmetric.

3.4 THE EFFECT OF ACCELERATION RATIO

The above results were obtained for an acceleration ratio $R_g=\Omega^2(R+L)/g=100$. The body force field is then created purely by centrifugal force; gravity is negligible. In this section, by fixing other parameters, i.e. $Ra=5\times10^4$, $Ek=5\times10^{-3}$, $Pr=100$, $R_1=100$, the effects of gravity on heat transfer rate and flow will be explored.

When the acceleration ratio decreases, gravity becomes more important for constant of Ra and Ek. It may be expected that the heat transfer rate will increase as Rg approaches one due to increased body force field. Figure 3.23 confirms this trend. Because gravity acts perpendicular to the main flow direction, the increase in heat transfer is small. When Rg decreases from 100 to 1, the heat transfer rate increases

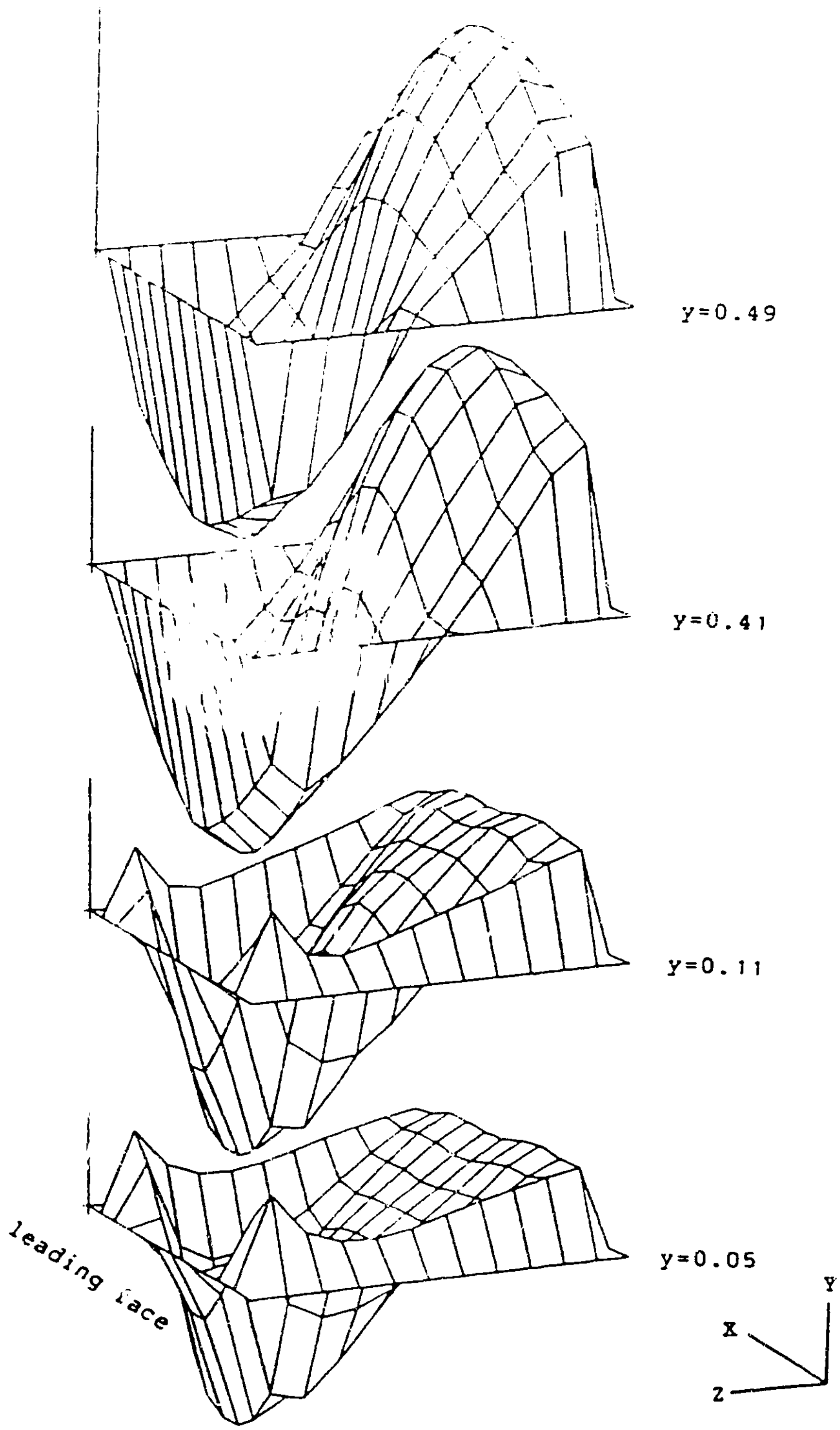

Figure 3.21 Development of the axial velocity profile for Pr=0.01, at $Ra=5\times10^4$, $Ek=5\times10^{-3}$, $R_g=100$, $R_1=100$.

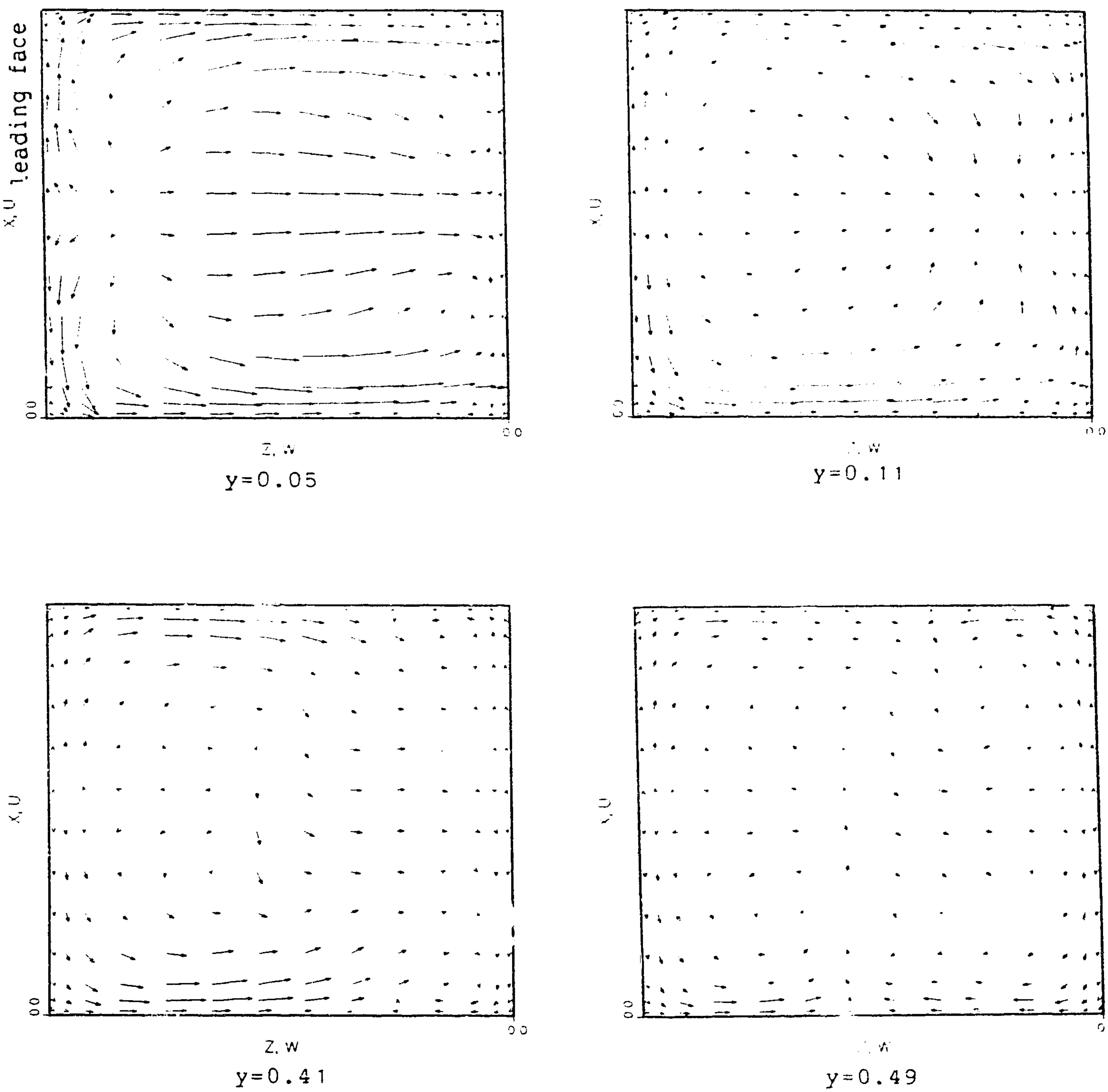

Figure 3.22 Development of the transverse velocity field for Pr=0.01, at $Ra=5\times10^4$, $Ek=5\times10^{-3}$, $R_g=100$, $R_l=100$.

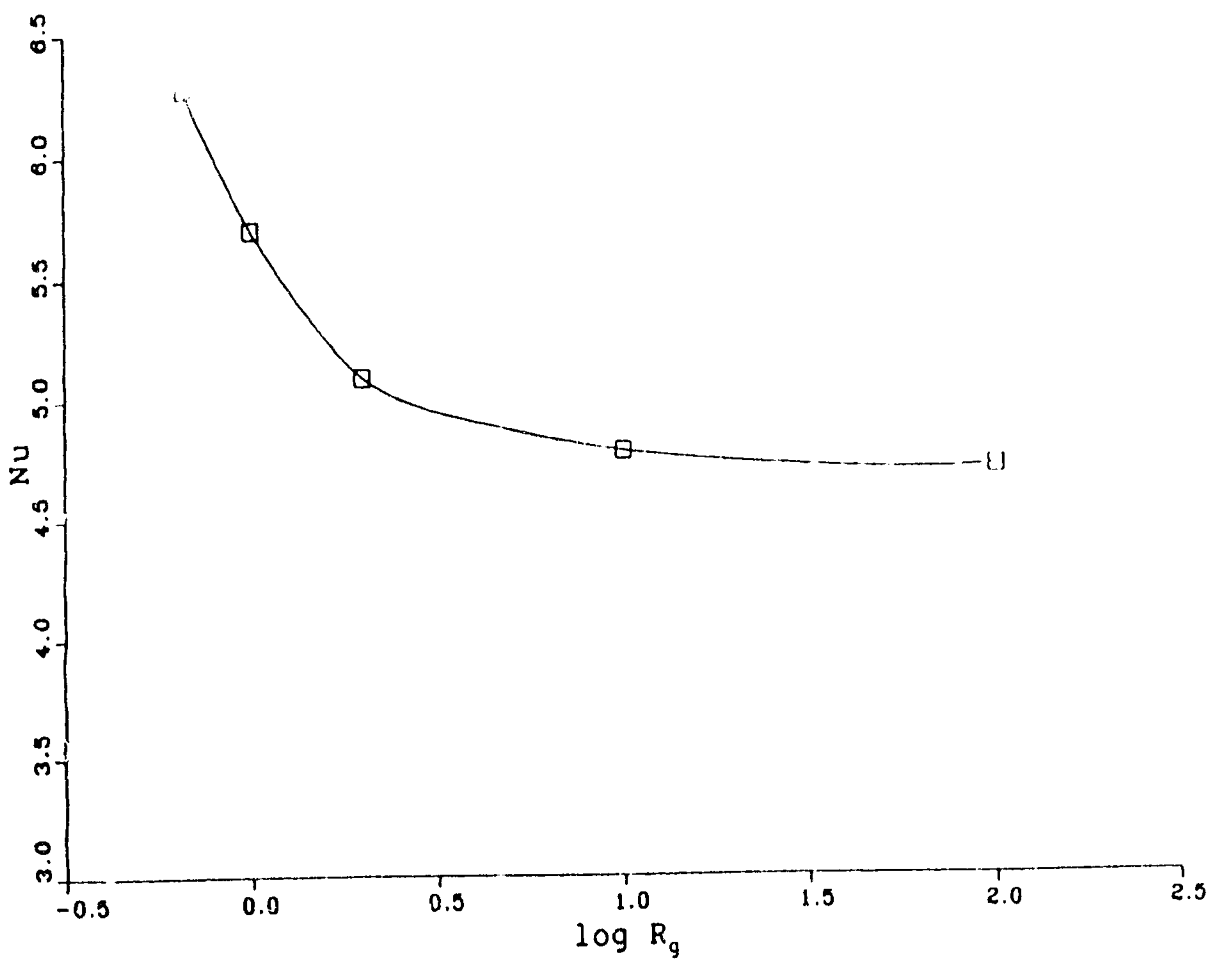

Figure 3.23 Effect of acceleration ratio on heat transfer at $Ra=5\times10^4$, $Ek=5\times10^{-3}$, $Pr=100$, $R_1=100$.

about 20%.

When $R_g=1$, both the gravity force and the centrifugal force have the same magnitude, but the centrifugal force acts in the same direction as the main flow, whereas the gravity acts on the secondary flow. Hence as R_g decreases, the primary flow tends to change its orientation. Figure 3.24 clearly illustrates the change in orientation. By comparison with Figure 3.3, it is evident that the indirect buoyancy forces alter the shape and location of the opposed filaments in the mid length region and is reflected along the entire length of the tube. The tendency for the Coriolis force to generate a two-dimensional flow is thus modified by gravity.

Figure 3.25 reveals how the Coriolis force, acting tangentially on the Z direction, combines with gravity, acting vertically on the X direction, to produce a complex secondary flow pattern. Near the closed end, lateral motion away from a stagnation point is still observed but thermal buoyancy augments any downward flow, especially near the leading face. This distortion continues with increasing distance from the closed end, but apparently has little effect on the mid length region. The vortices in the mid length region were found to be slightly anti-symmetric. The effect of the gravitational acceleration in the midddle of the thermosyphon is evidently slight, as heralded in the axial velocity profile.

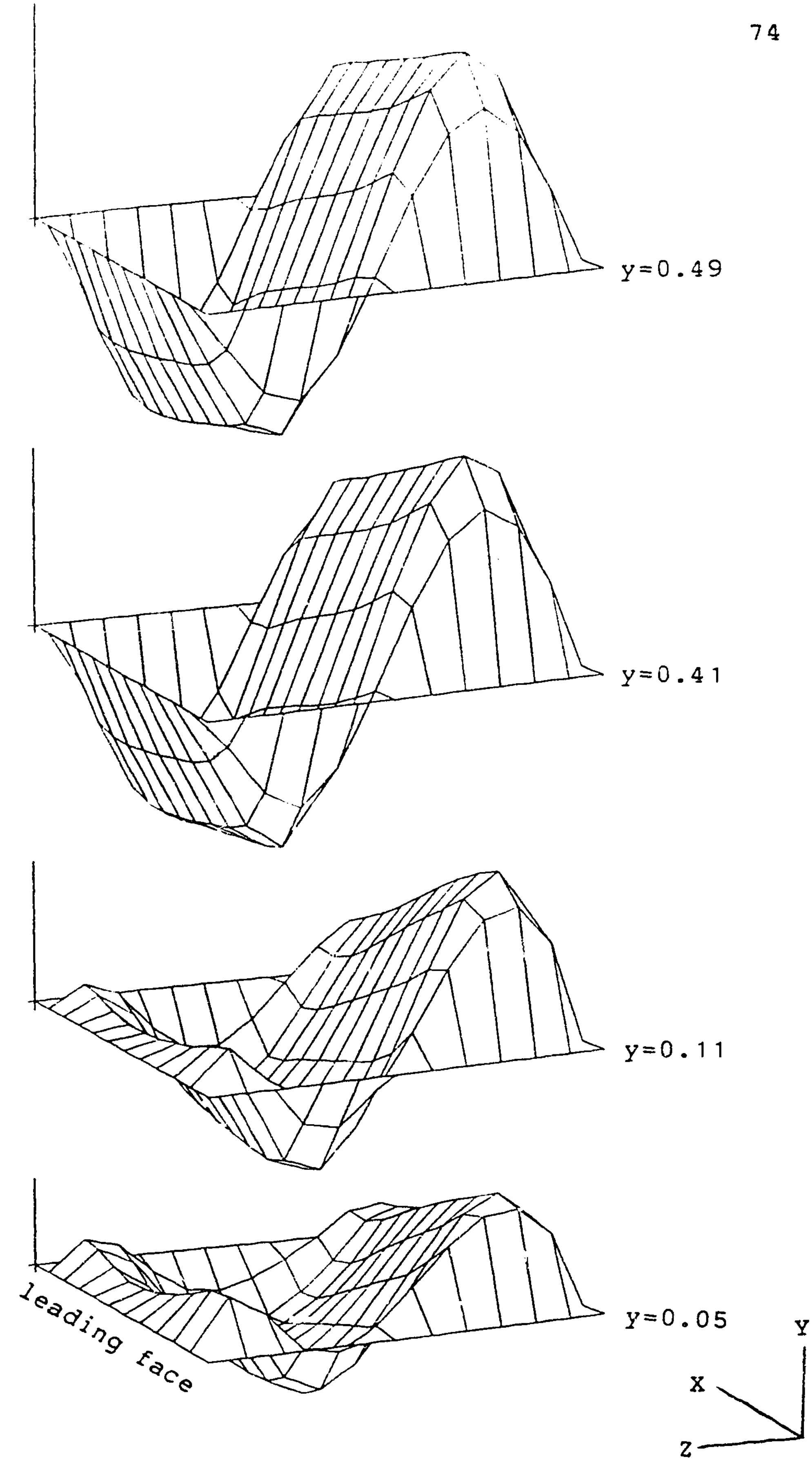

Figure 3.24 Development of the axial velocity profile for $R_g=1$, at $Ra=5\times10^4$, $Ek=5\times10^{-3}$, $Pr=100$, $R_1=100$.

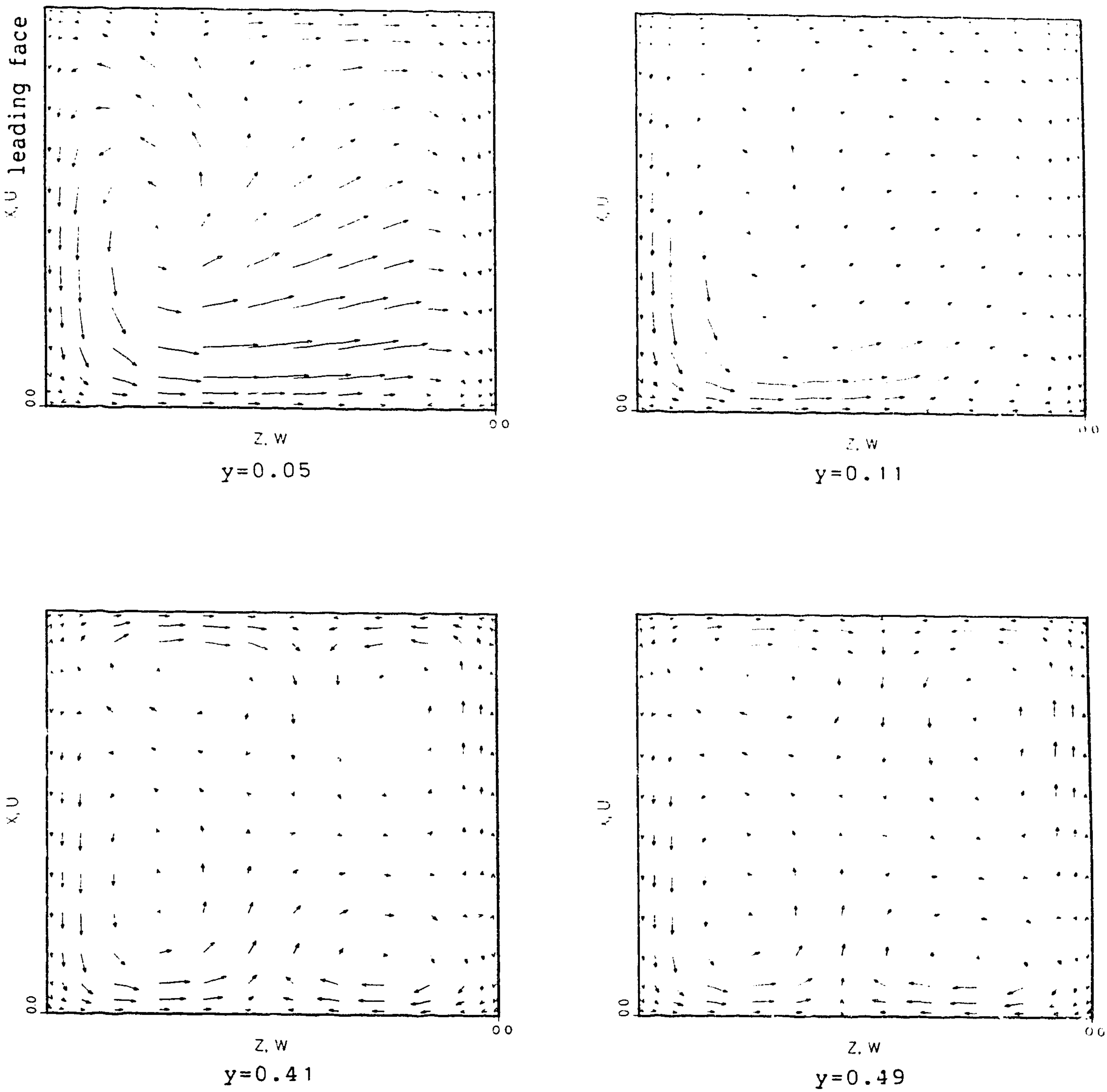

Figure 3.25 Development of the transverse velocity field for $R_g=1$, at $Ra=5\times10^4$, $Ek=5\times10^{-3}$, $Pr=100$, $R_1=100$.

3.5 THE EFFECT OF ECCENTRICITY

All of above results were obtained for an eccentricity $R_1=R/L=100$, when the body force field is almost uniform along the whole system. When the thermosyphon is closer to the rotating axis, the body force is weaker and is no longer uniform. With the other parameters constant ($Ra=5\times10^4$, $Ek=5\times10^{-3}$, $Pr=100$, $R_g=100$), it may be expected, that the Nusselt number will decrease when the length ratio decreases. As shown in Figure 3.26, when $R_1=1$, the Nusselt number is 77% of that when $R_1=100$; when $R_1=0$, the Nusselt number is 1.86, 40% of that when $R_1=100$.

When $R_1=1$, both the primary circulation and the main flow profile are almost the same as for $R_1=100$, except they are weaker. The secondary flow, as shown in Figure 3.27, is somewhat different in the mid length region. The mid length symmetry found for $R_1=100$ is now lost. The pair of vortices in the hot fluid coming from the outer end occupies a bigger area because the body force in the outer end is stronger.

When the $R_1=0$, the cold end reaches the axis of rotation, the main circulation is no longer the same; the change is illustrated in Figure 3.28. At the cold end, flow in almost one fifth of the tube length is very weak if not stagnant, and heat is transferred by conduction in this region; the fluid circulates elsewhere. Since the centrifugal force has a component in the Z direction, the secondary flow is caused by this component and the Coriolis force; the flow pattern is changed accordingly, as

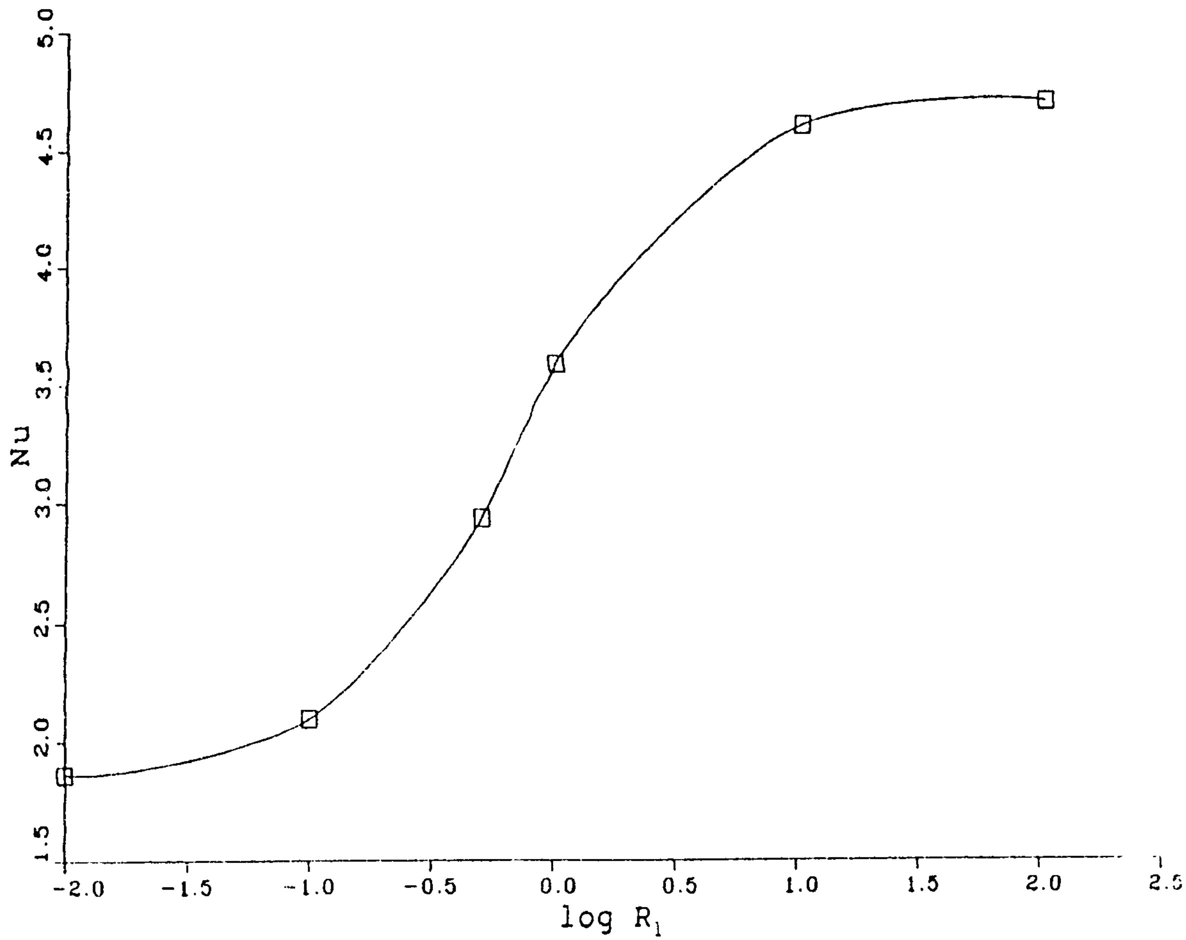

Figure 3.26 Effect of eccentricity on heat transfer at $Ra=5\times10^4$, $Ek=5\times10^{-3}$, $Pr=100$, $R_g=100$.

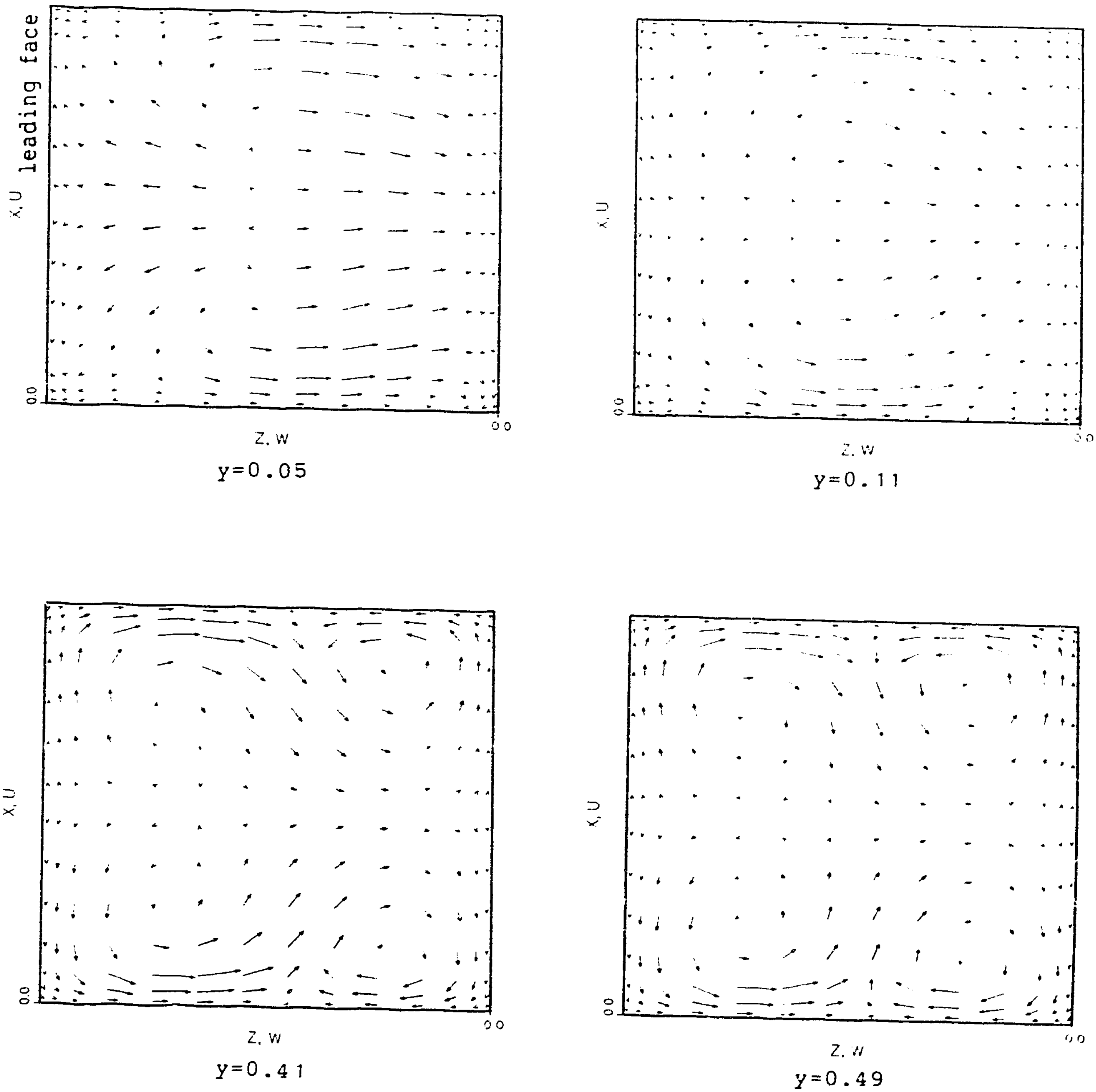

Figure 3.27 Development of the transverse velocity field for $R_1=1$, at $Ra=5\times10^4$, $Ek=5\times10^{-3}$, $Pr=100$, $R_g=100$.

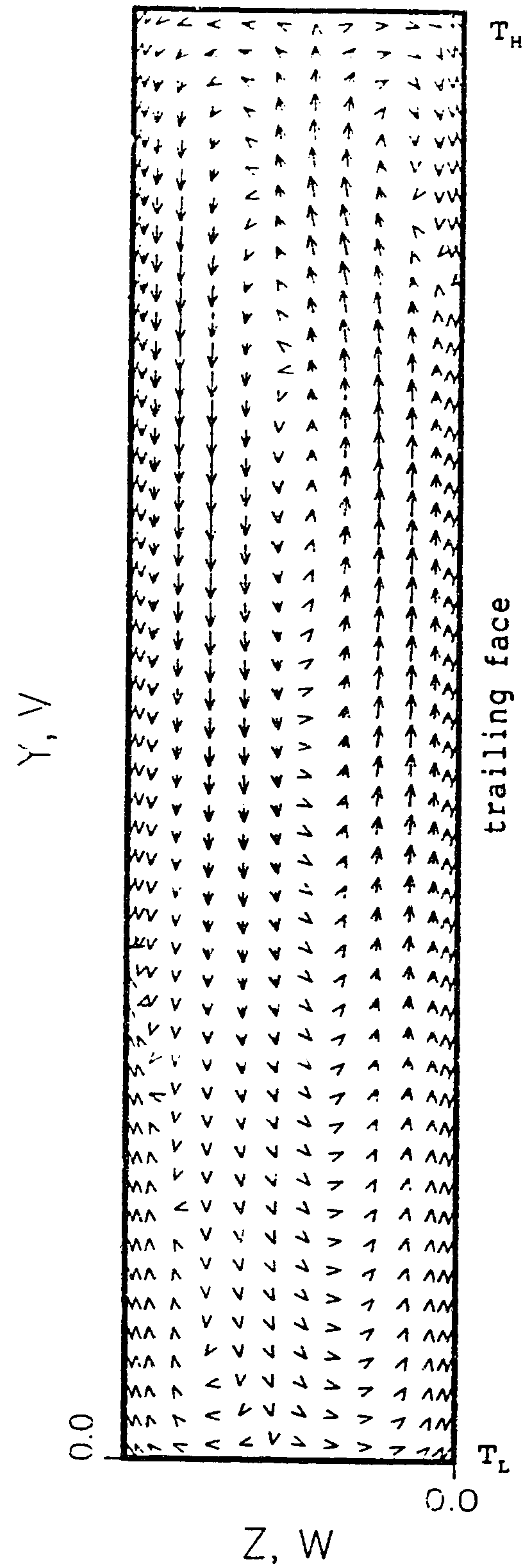

Figure 3.28 Velocity field in mid plane of rotation x=0.5 for R_1=0, at Ra=5×10^4, Ek=5×10^{-3}, Pr=100, R_g=100.

illustrated in Figure 3.29.

3.6 CONCLUSIONS

In this chapter, the three dimensional flow structure and heat transfer properties of a single-phase, radial thermosyphon in the laminar flow region were explored with the axis of rotation vertical.

Basically, the flow pattern consists of an annular refluent flow at the two closed ends combined with a bifilamental flow in the mid length region; hot fluid moves over the leading face and cold fluid moves over the trailing face. The distinctive characteristic of the rotating thermosyphon is that the Coriolis force may flatten the axial velocity profile, making it look almost two-dimensional. The secondary motion is caused mainly by Coriolis acceleration. Two pairs of vortices with strength mainly in the Ekman layers appear at the mid length region, reminiscent of the behaviour in a tilted, gravitational system.

Varying the Rayleigh number does not significantly alter the flow pattern, except that as Ra increases, the refluent flow at the two ends extends. At the highest Rayleigh number, for which we have a converged solution, transition to a new flow pattern appears.

The plot of Nusselt number against Rayleigh number was used to reflect the thermal regimes. Above the conduction maximum Rayleigh number, the behaviour of the system spanned

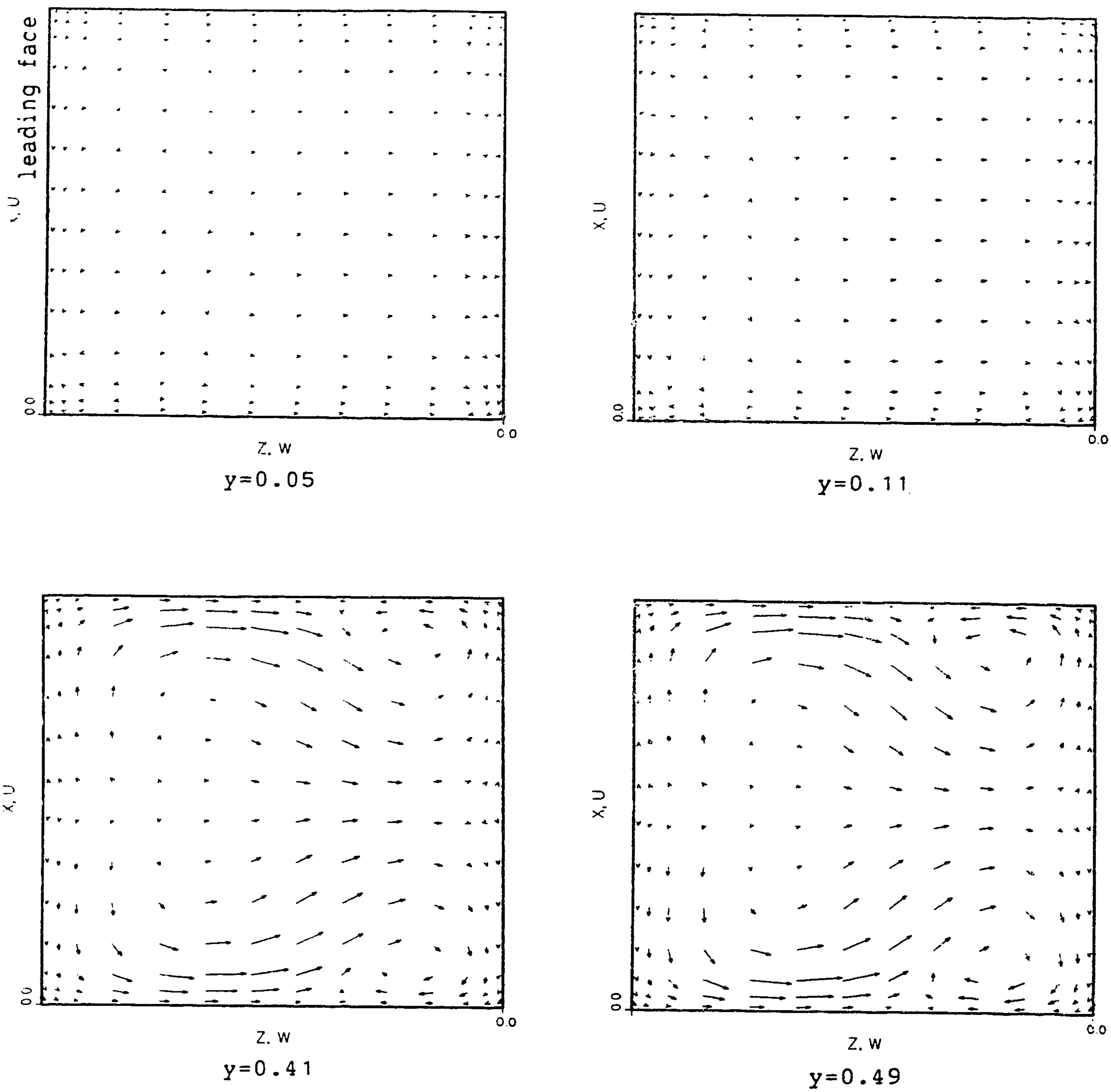

Figure 3.29 Development of the transverse velocity field for $R_l=0$, at $Ra=5\times10^4$, $Ek=5\times10^{-3}$, $Pr=100$, $R_g=100$.

two established regimes: impeded and boundary layer. It was found that the rotating thermosyphon does not give a higher heat transfer rate for this Ekman number range compared to the stationary thermosyphon.

As Ekman number increases, the flow pattern remains, but the flattened two-dimensional main flow profile gradually disappears due to the decreasing Coriolis force. At $Ek=5\times10^{-1}$, the flow pattern is quite similar to that observed in stationary vertical thermosyphon.

As the Ekman number decreases, indicating a faster rotating speed and higher Coriolis force, the Nusselt number increases first, reaches a maximum and then drops quickly. This is because the Coriolis force increase the secondary flow, but reduces the primary flow at the same time; the two processes evidently balance each other. It seems that the thermal and hydrodynamic regimes of a rotating thermosyphon are defined by both Ra and Ek.

For Pr<<1, the flow is much more vigorous. The bifilamental flow in the central region is extended, and the whole flow field is quite close to unicellular flow. Decreasing the Prandtl number will decrease the Nusselt number. It does not mean a decrease in heat transfer rate, but implies that the effect of convection is reduced.

By taking gravity into consideration, it was found that the indirect buoyancy force alters the shape and location of the opposed filaments in the mid length region and is reflected along the entire length of the tube. As the acceleration ratio becomes one, that means gravity becomes equally important to the centrifugal force, the heat transfer rate increases about 20%.

As expected, reducing the length ratio gives a weaker flow. For $R_l=0$, the inner part of the fluid becomes stagnant, leaving fluid circulating in the outer part of the tube; the heat transfer rate drops by 60% at $R_l=0$.

4. ECCENTRIC THERMOSYPHON

In this chapter, fluid flow and heat transfer in the rotating eccentric thermosyphon, shown in Figure 2.2, will be studied in the laminar flow regime. The vertical axis of rotation is parallel to its centre line. The thermosyphon is heated from below and cooled at the top. When the thermosyphon rotates, the centrifugal force will create a body force field similar to that in a horizontal stationary thermosyphon. The centrifugal force field is thus perpendicular to the main temperature gradient.

According to the geometry of the thermosyphon, the two aspect ratios will be set as: $A_x=5$ and $A_y=1$; the axial length is five times that of the side. A uniform $51\times15\times15$ mesh network was used.

4.1 THE EFFECT OF RAYLEIGH NUMBER

The basic flow pattern and the effect of Rayleigh number on heat transfer rate and fluid flow will be studied in this section. All other parameters will be fixed at: $Ek=2\times10^{-3}$, $Pr=100$, $R_g=100$ and $R_l=100$.

Overall Nusselt number as a function of Rayleigh number is given in Figure 4.1. The shape and magnitudes shown are similar to those of the stationary horizontal thermosyphon [28,29,30], also plotted in Figure 4.1, where, in the definition of Ra, $\Omega^2(\mathcal{R}+L)$ is replaced by g. For Rayleigh number less than $10^{2.5}$, heat is transferred mainly by conduction, even though convection occurs theoretically as

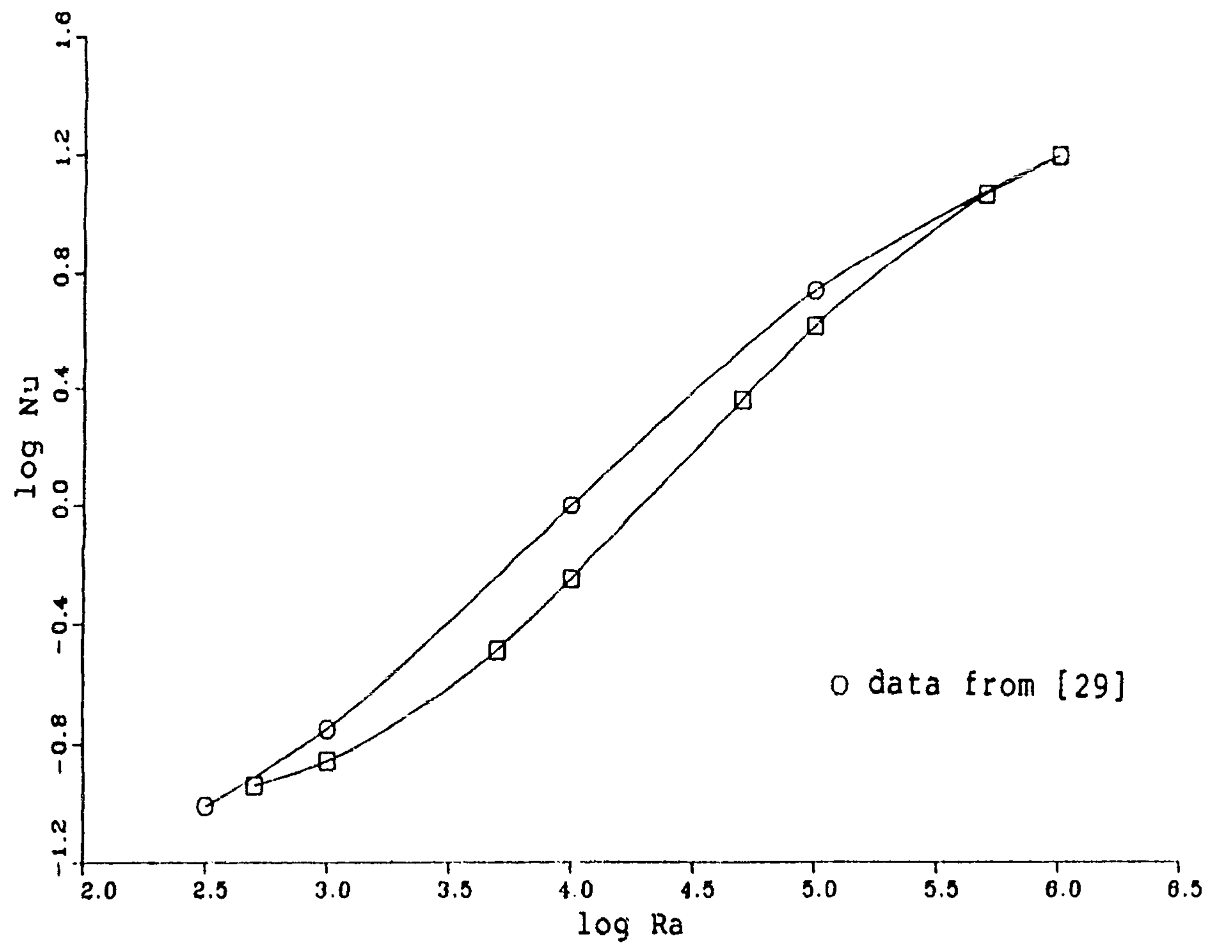

Figure 4.1 Effect of Rayleigh number on heat transfer in a eccentric thermosyphon at $Ek=2\times10^{-3}$, $Pr=100$, $R_g=100$, $R_l=100$.

long as there is a temperature difference between the two ends. After this "critical point", convection gradually becomes more important, and heat transfer increases significantly. As indicated by Lock and Han [29], the boundary layer flow regime begins at about $Ra=10^7$ for this slenderness ratio ($A_x=5$). The range in which Ra is larger than $10^{2.5}$ and smaller than 10^6 might be appropriately described as an impeded regime. In Figure 4.1, a slope of about 0.9 occurs in the range of Ra from 10^4 to 10^5. On the left half of the impeded regime, a concave curve joins the conduction regime; and on the right half, a convex curve joins the boundary layer regime. The impeded regime acts like an extended transition between the conduction and boundary layer regimes. The details of heat transfer from each faces are shown in Figure 4.2. The distributions and variations are similar to that of the horizontal stationary thermosyphon [28,29].

The basic flow pattern in a stationary horizontal thermosyphon exposed to different end temperatures consists of a simple primary loop upon which is superimposed a secondary circulation induced by lateral temperature gradients. Figure 4.3 illustrates the primary flow of the eccentric thermosyphon at $Ra=5\times10^4$. In the mid-length region, the familiar two-filament flow is evident, but near the two ends the flow is complicated. Figures 4.4 and 4.5 show the main flow profile and the secondary flow respectively. At the hot end, under the influence of the

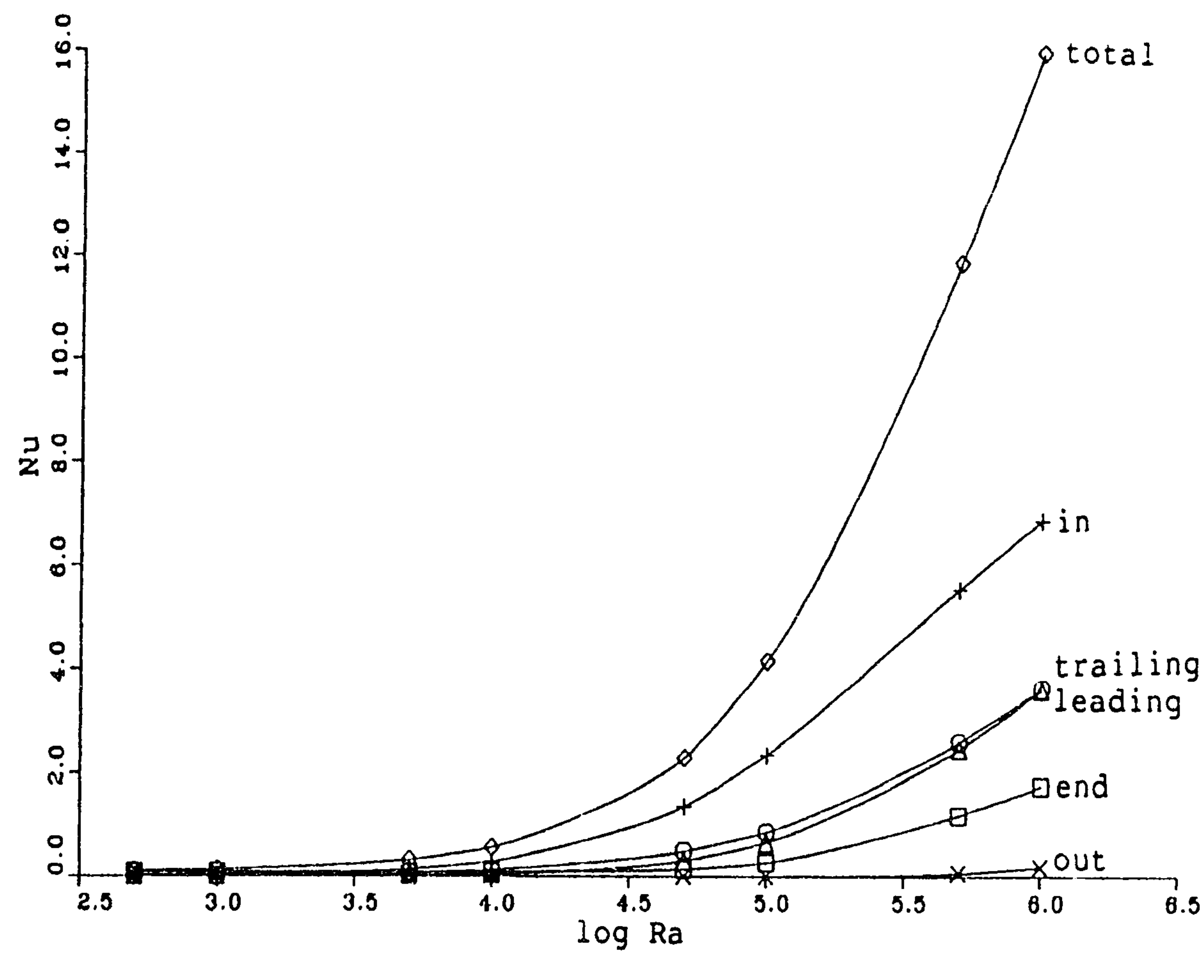

Figure 4.2 Components of the heat transfer rate at $Ek=2\times10^{-3}$, $Pr=100$, $R_g=100$, $R_l=100$.

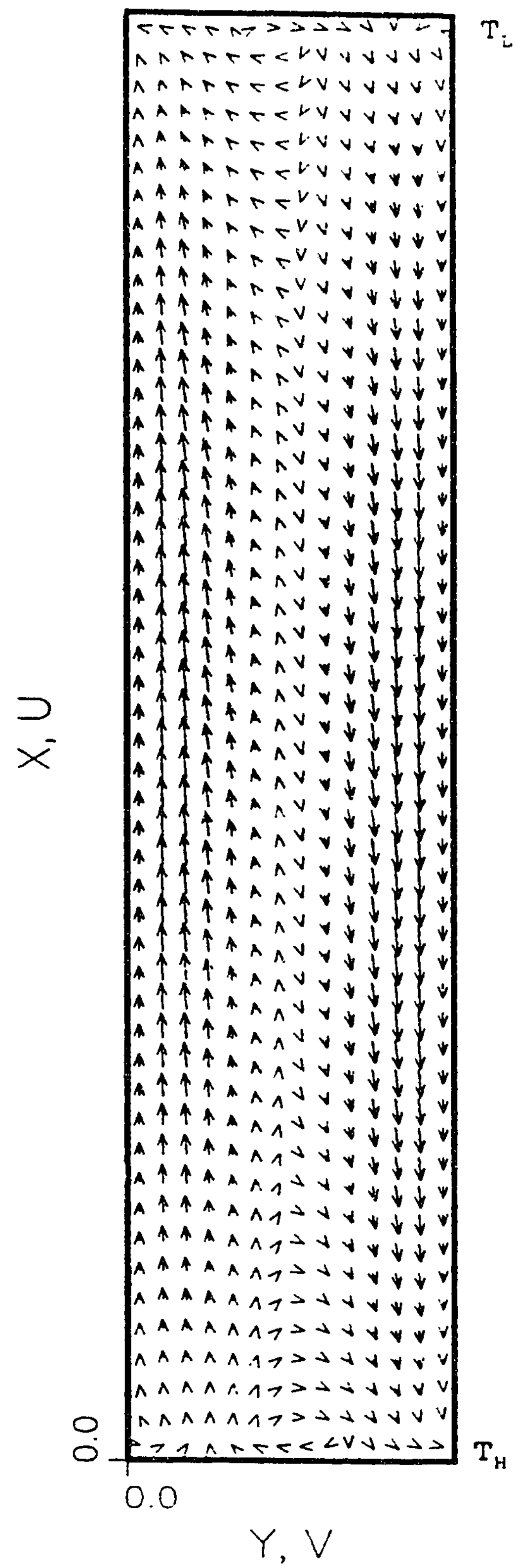

Figure 4.3 Velocity field in plane z=0.46

for $Ra=5\times10^4$ at $Ek=2\times10^{-3}$, $Pr=100$, $R_g=100$, $R_l=100$.

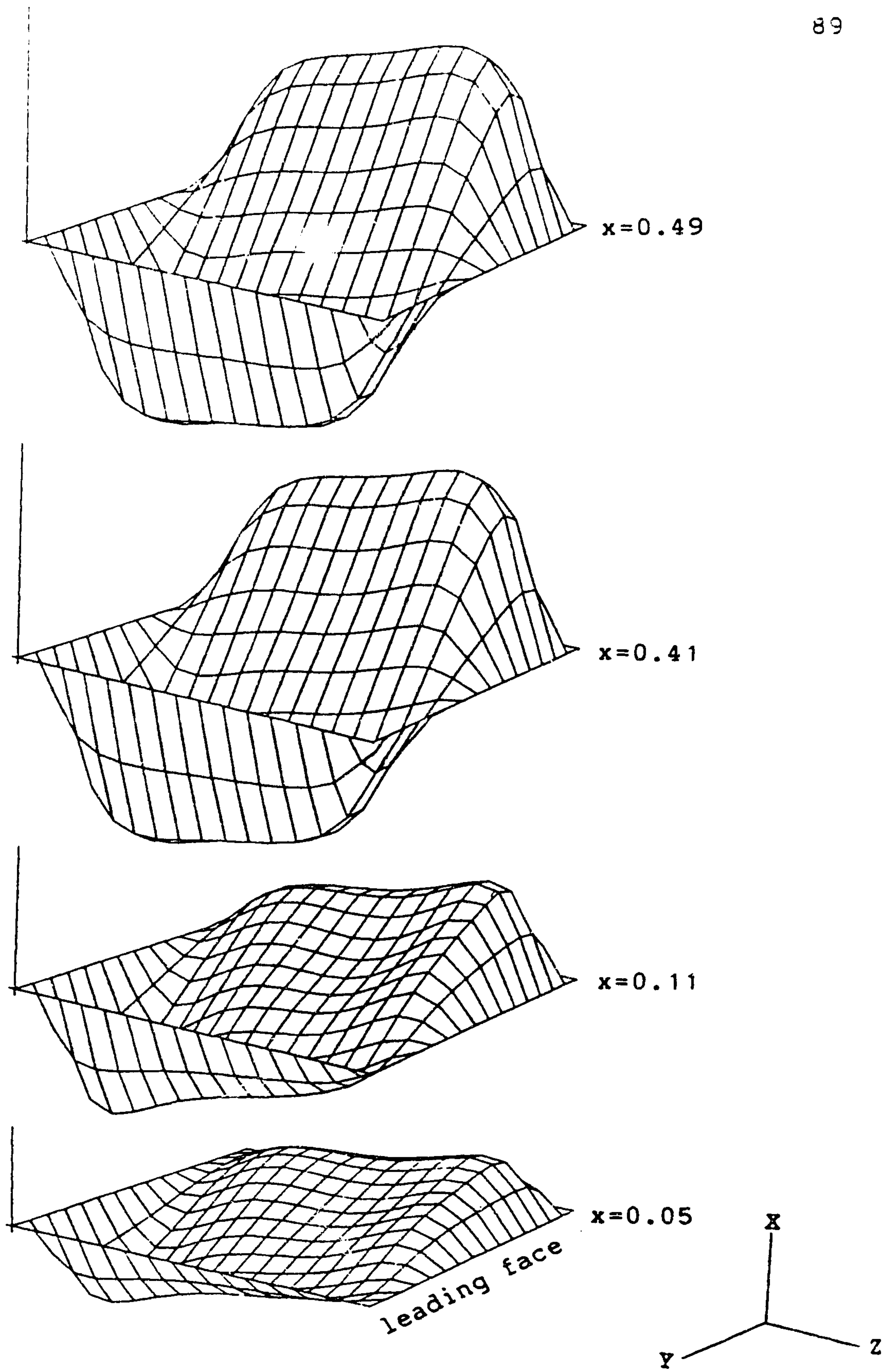

Figure 4.4 Development of the main flow velocity profile for $Ra=5\times10^4$ at $Ek=2\times10^{-3}$, $Pr=100$, $R_g=100$, $R_1=100$.

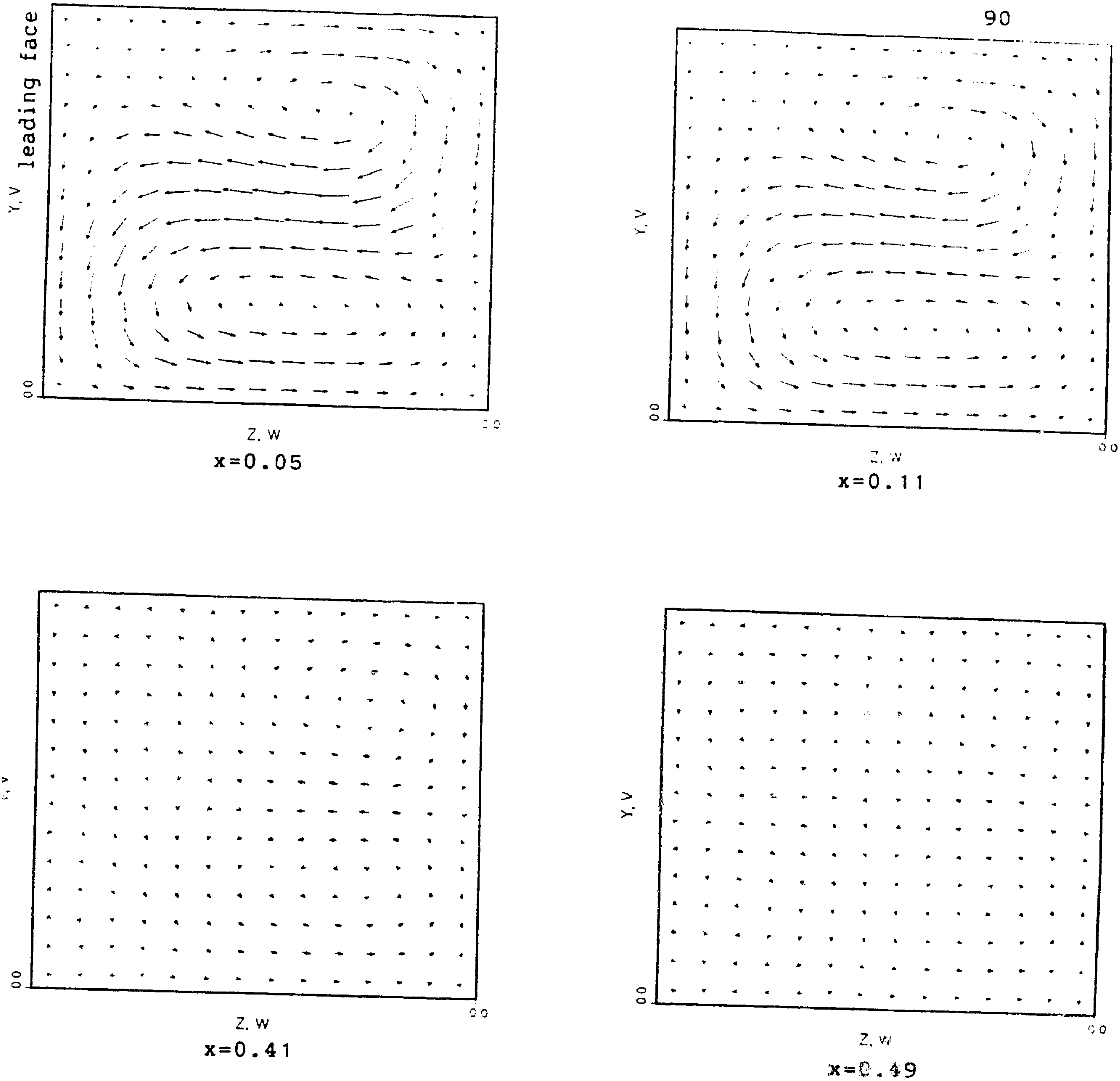

Figure 4.5 Development of the transverse velocity field for $Ra=5\times10^{4}$ at $Ek=2\times10^{-3}$, $Pr=100$, $R_g=100$, $R_l=100$.

direct buoyancy force, as in stationary horizontal thermosyphon, the fluid in a lateral plane will flow in the Y direction to complete the main flow cycle. Also under the influence of the Coriolis force, the flow in the Y direction will induce a flow in the Z direction. Since these two forces act together, the secondary flow is changed to the present S shape (actually reverse of S). As seen in Figure 4.5, it is a clockwise vortical motion in the upper part (the cold fluid filament), and an anti-clockwise vortical motion in the lower part (the hot fluid filament). This vortical motion may be transmitted to the filaments by a shearing action which causes it to rotate. Reflected on the main flow, it produces the twisted shape, and the profile is not flat. Away from the ends, the Coriolis effect becomes weaker. At the mid length plane, two pairs of weak vortices, both induced by the lateral temperature gradient. are found. Over the length of the tube, these must become reconciled with the S-pattern in the end regions.

Referring to the governing equations, if the Ekman number is fixed, when Rayleigh number decreases, the magnitude of the Coriolis term will increase relative to the buoyancy force. Hence, for smaller Rayleigh numbers, a stronger Coriolis effect will result; and for larger Rayleigh numbers, the opposite will be true.

The primary circulation and the main flow profile at $Ra=5\times 10^3$ are the same as for $Ra=5\times 10^4$, except they are weaker. Figure 4.6 shows the secondary flow field. Near the

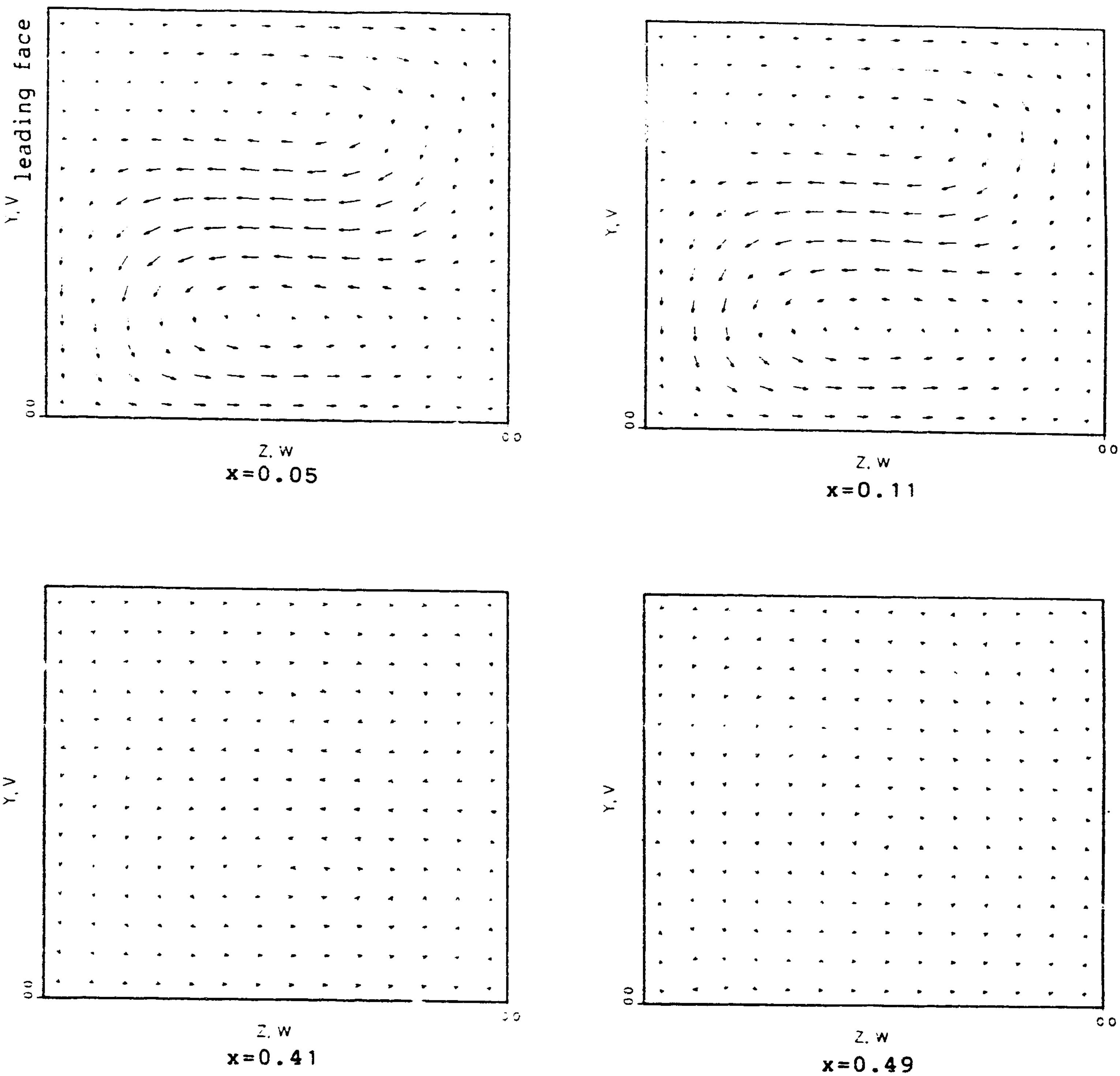

Figure 4.6 Development of the transverse velocity field for $Ra=5\times10^3$ at $Ek=2\times10^{-3}$, $Pr=100$, $R_g=100$, $R_1=100$.

hot end, the secondary flow is the same as for $Ra=5\times10^4$ in Figure 4.5. But here, the Coriolis force is relatively stronger, so the end flow is propagated further towards the mid length plane. The two pairs of vortices found in Figure 4.5 are absent here.

With $Ra=10^6$, the primary circulation, the main flow profile and the secondary flow field are shown in Figures 4.7, 4.8, 4.9 respectively. For a higher Rayleigh number, relative to buoyancy force, the Coriolis force is weaker. As a result, the secondary flow in the end region is closer to those found in the stationary horizontal thermosyphon. The two pairs of vortices in the mid length region are stronger, and the main flow profile in the region is more smooth. The twist of the main flow profile near the ends is restricted to near the side wall.

4.2 THE EFFECT OF EKMAN NUMBER

The Ekman number, representing the relative importance of viscous and Coriolis effects, is always of major interest in the study of rotating systems. For higher Ekman numbers, meaning a smaller Coriolis effect, the system will behave more like a stationary system.

With other parameters constant ($Ra=5\times10^4$, $Pr=100$, $R_g=100$, $R_1=100$), the flow pattern with $Ek=2\times10^{-3}$ is already known. For a higher Ekman number, $Ek=2\times10^{-2}$, the primary flow circulation, the main flow profile and the secondary flow field are shown in Figures 4.10, 4.11, 4.12,

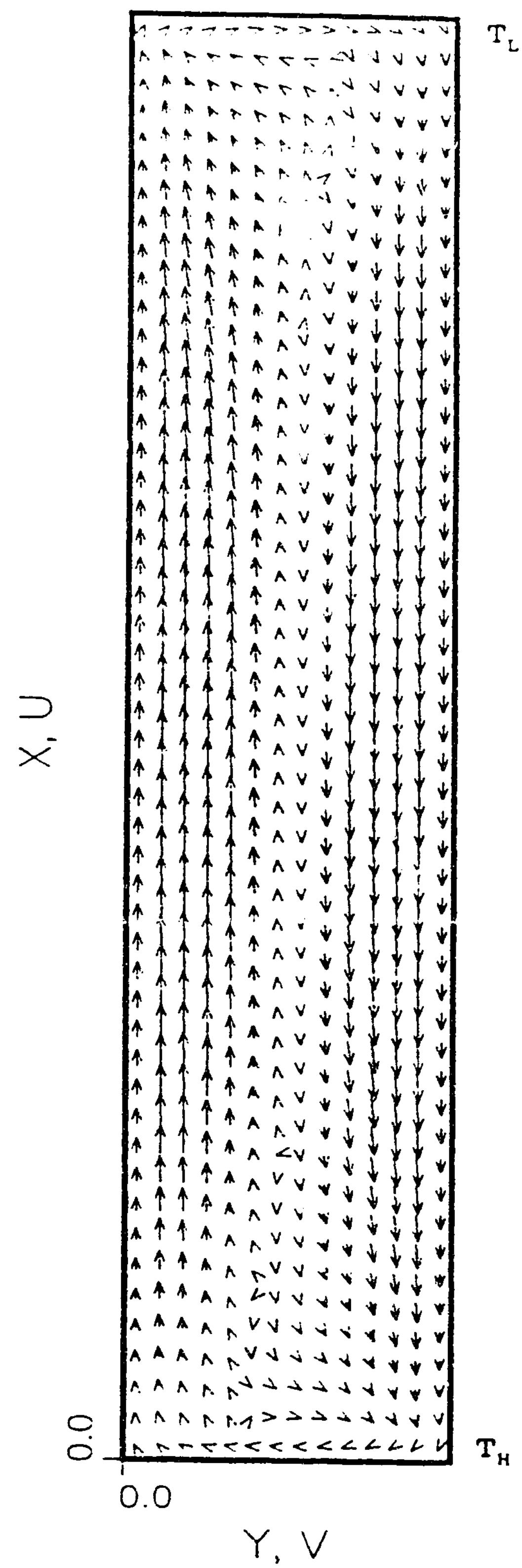

Figure 4.7 Velocity field in plane z=0.46 for $Ra=10^6$ at $Ek=2\times10^{-3}$, $Pr=100$, $R_q=100$, $R_l=100$.

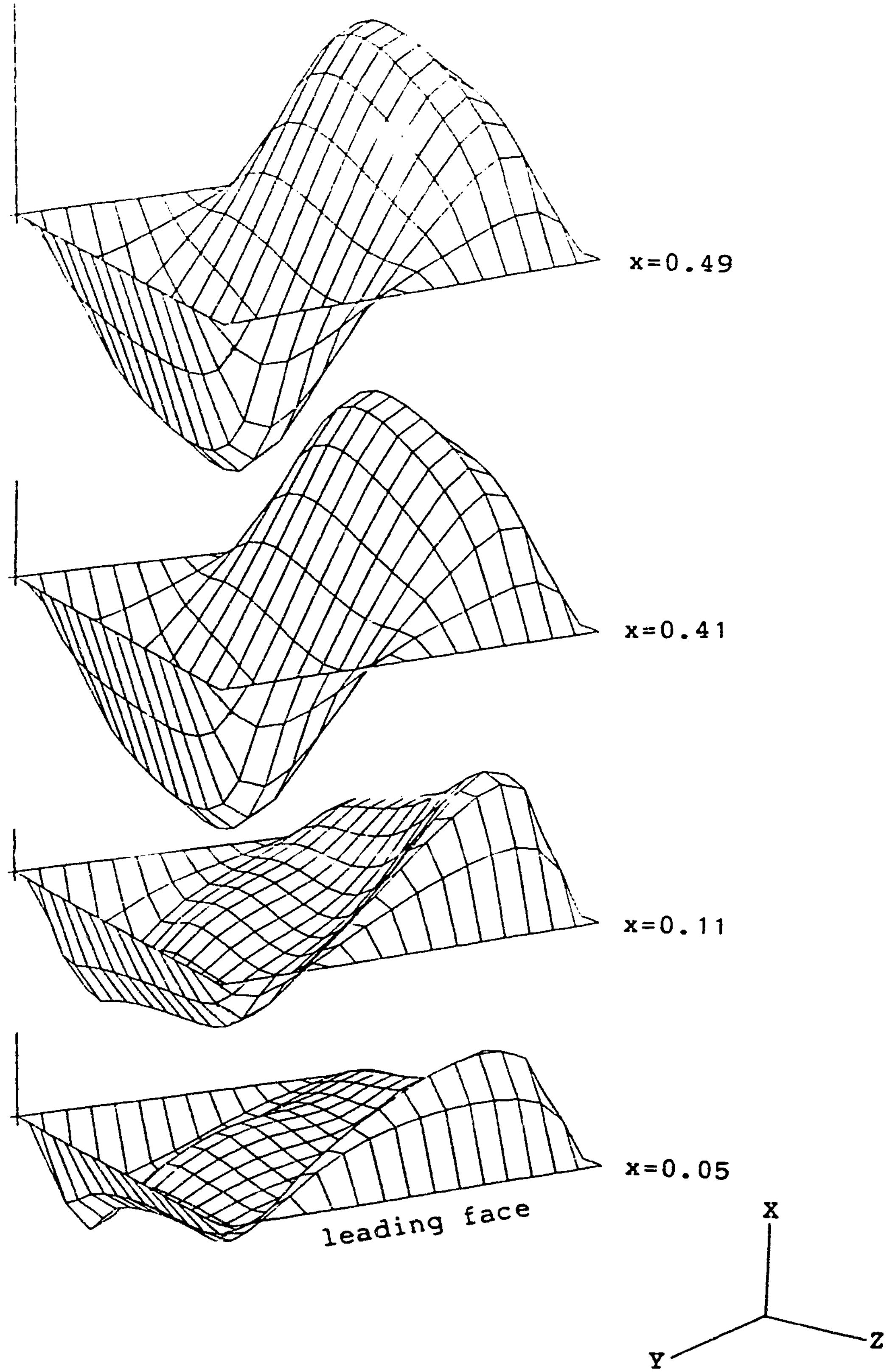

Figure 4.8 Development of the main flow velocity profile for $Ra=10^6$ at $Ek=2\times10^{-3}$, $Pr=100$, $R_g=100$, $R_l=100$.

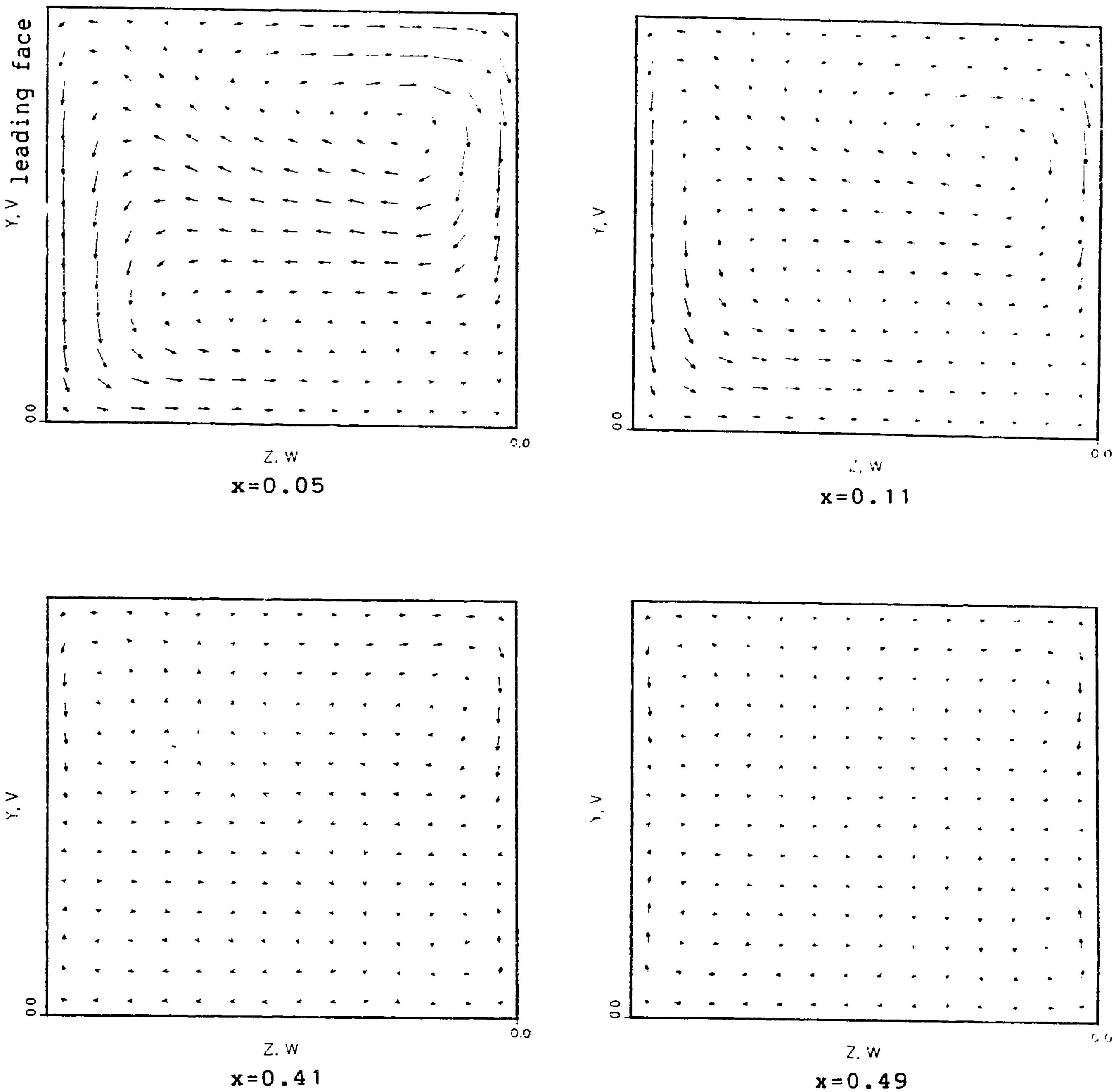

Figure 4.9 Development of the transverse velocity field for $Ra=10^6$ at $Ek=2\times10^{-1}$, $Pr=100$, $R_g=100$, $R_l=100$.

respectively. The primary circulation is a single cell. Near the end, the secondary flow is only slightly modified by the Coriolis force at the centre of the tube. This modification is reflected in the main flow profile; the flow is slightly twisted and is 50% stronger than that at $Ek=2\times10^{-3}$. In the mid length region of the thermosyphon, a bifilamental main flow is developed, and two pairs of vortices induced by lateral temperature gradients are formed.

The individual surface heat transfer rates as functions of Ekman number are plotted in Figure 4.13. For Ekman numbers from 10^{-1} to 10^{-2}, the heat transfer rate decreases only slightly. Below $Ek=10^{-2}$, the heat transfer rate drops more quickly. This is because, as Ek decreases, meaning the Coriolis effect increases, the secondary flow near the end is twisted more to a S shape; the buoyancy force is then balanced more by the Coriolis force. As a result, the main flow velocity is retarded and the heat transfer rate drops. This behaviour is found to correspond to a Coriolis impeded regime in which the heat transfer rate decreases as the Ekman number decreases.

4.3 THE EFFECT OF PRANDTL NUMBER

The flow pattern for high Prandtl number is already known. Figure 4.14 shows the main flow circulation at Pr=0.01. Near the end, it is an annular refluent flow not found before. The flow gradually develops to a bifilamental flow at the mid length region with the cooler fluid moving

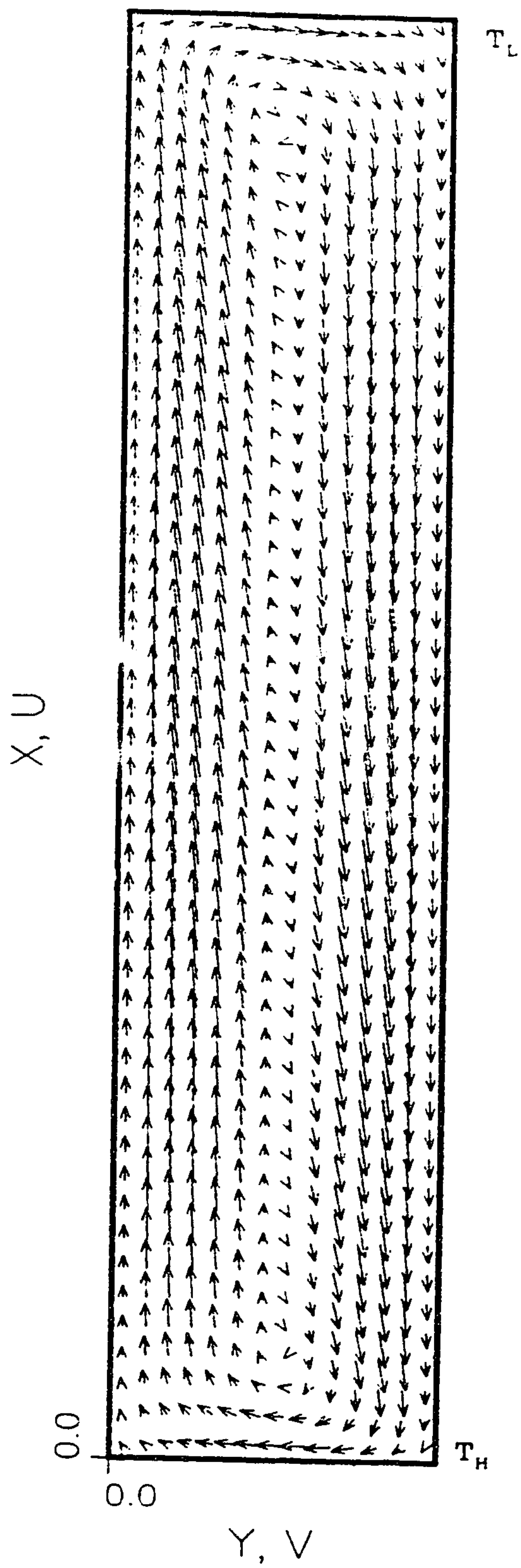

Figure 4.10 Velocity field in plane z=0.46

for $Ek=2\times10^{-2}$ at $Ra=5\times10^{4}$, $Pr=100$, $R_g=100$, $R_l=100$.

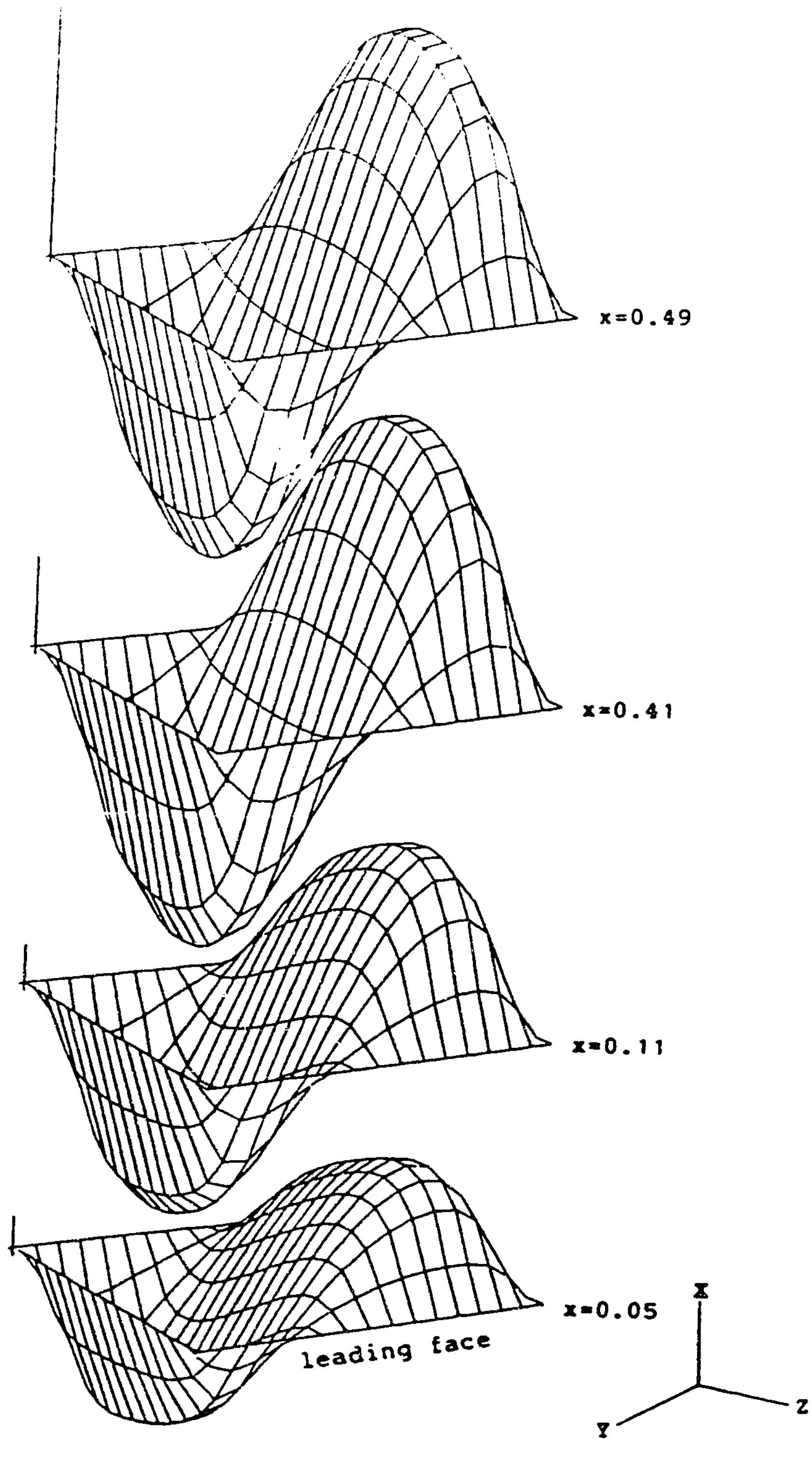

Figure 4.11 Development of the main flow velocity profile for $Ek=2\times10^{-2}$ at $Ra=5\times10^{4}$, $Pr=100$, $R_g=100$, $R_l=100$.

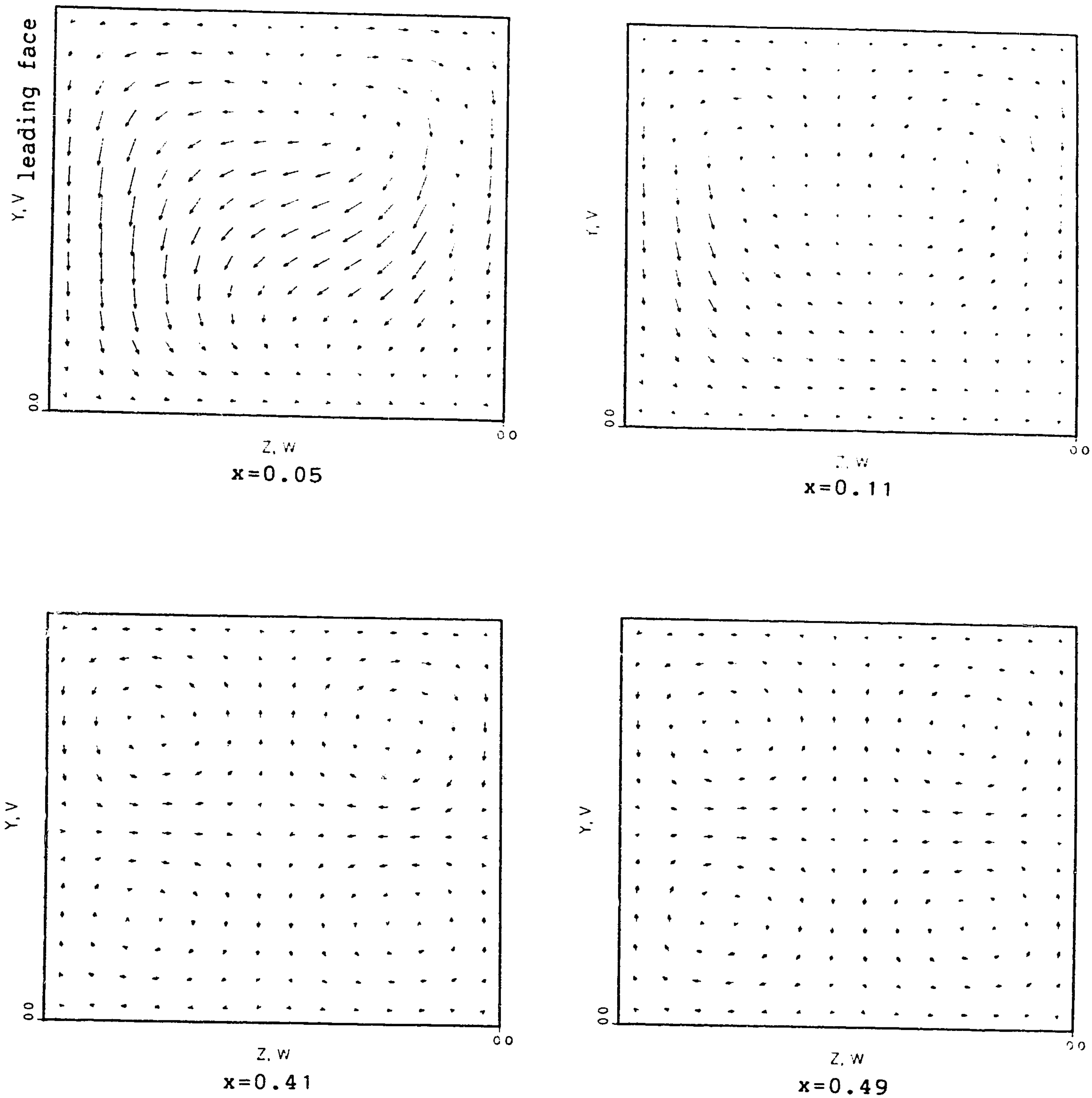

Figure 4.12 Development of the transverse velocity field for $Ek=2\times10^{-2}$ at $Ra=5\times10^{4}$, $Pr=100$, $R_g=100$, $R_l=100$.

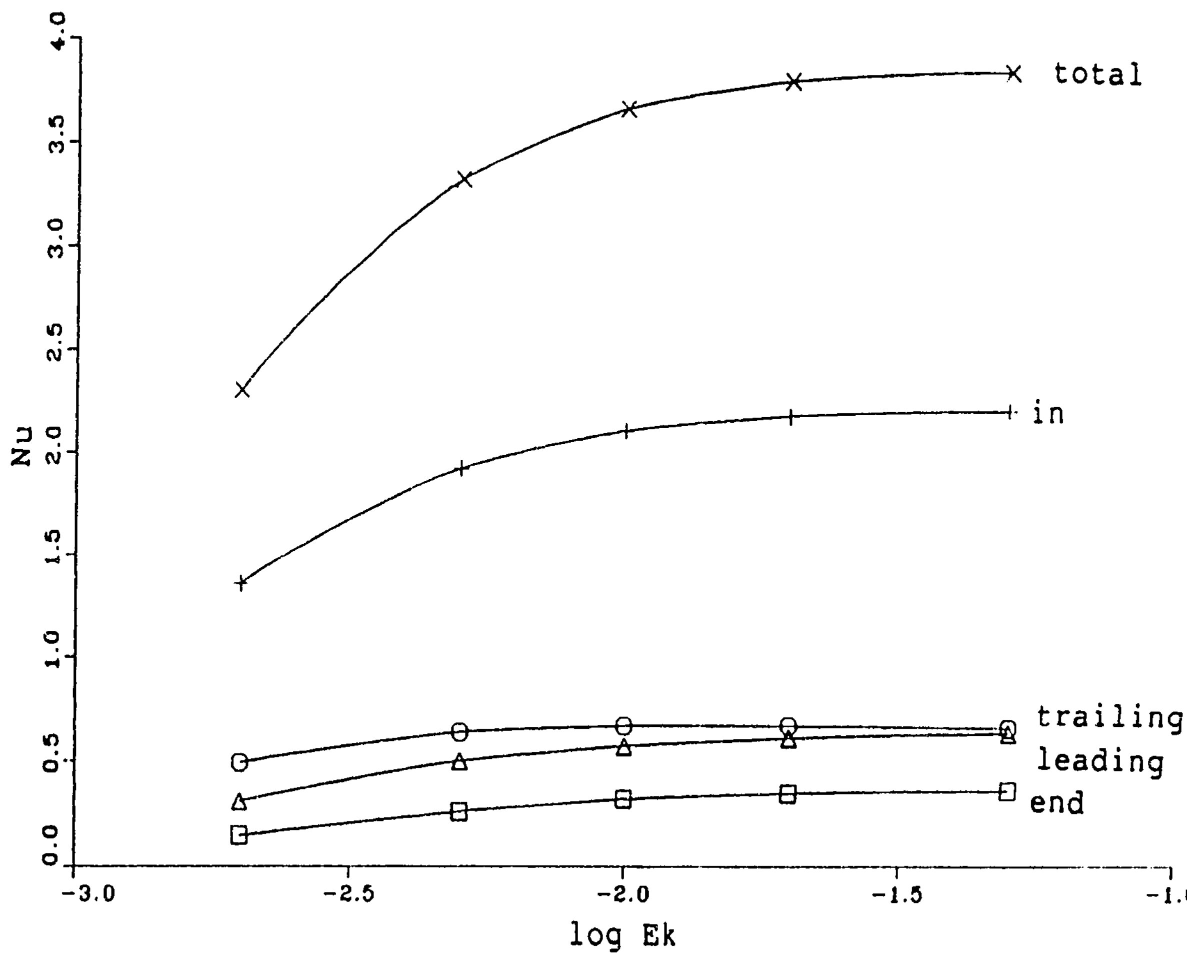

Figure 4.13 Effect of Ekman number on heat transfer at $Ra=5\times10^4$, $Pr=100$, $R_g=100$, $R_l=100$.

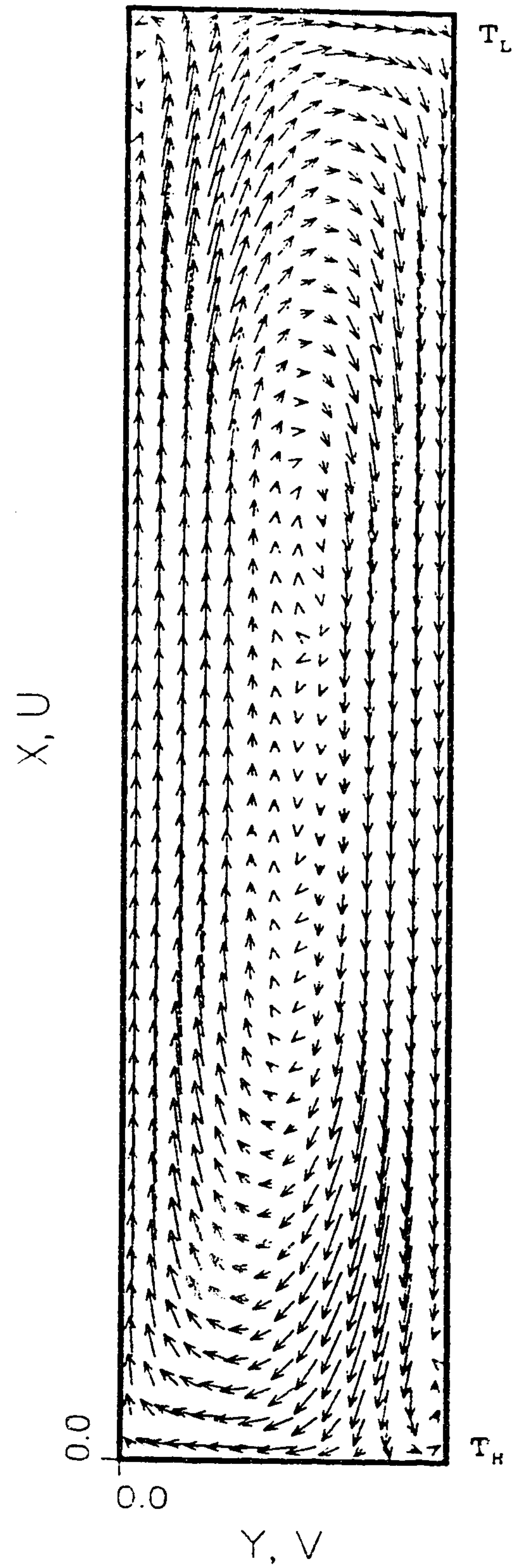

Figure 4.14 Velocity field in plane z=0.46 for Pr=0.01, at $Ra=5\times10^4$, $Ek=2\times10^{-3}$, $R_g=100$, $R_l=100$.

down at the outer surface, and the hotter fluid moving up at the inner surface. Superimposed upon this flow, as shown in Figure 4.15, there is a large cell in the mid length region with cold fluid down the leading face and hot fluid up the trailing face. This flow is more clearly shown on the main flow profile in Figure 4.16. In the secondary flow shown in Figure 4.17, the Coriolis effect is almost absent. The cell flow in the mid length region appears to be caused solely by the lateral temperature gradient.

For Prandtl number larger than 0.1, the Nusselt number was found to remain almost constant at about 2.3. Then, it drops rapidly to 1.3 at Pr=0.01. This reveals that the heat transfer rate increase caused by convection over conduction is less for a liquid metal.

4.4 THE EFFECT OF ACCELERATION RATIO

As the acceleration ratio $R_g=\Omega^2(\mathcal{R}+L)/g$ decreases, gravity becomes important. Gravity introduces a body force field that is in the opposite direction to the temperature gradient for the arrangement being considered. The system is then under the action of both direct and indirect buoyancy forces. The heat transfer rate may be expected to increase with a decrease in R_g if other parameters remain constant.

For R_g from 100 down to 10, the heat transfer rate changes very little. This suggests that as long as R_g is larger than 10, gravity can be neglected without any serious error in calculating the Nusselt number. When R_g decreases

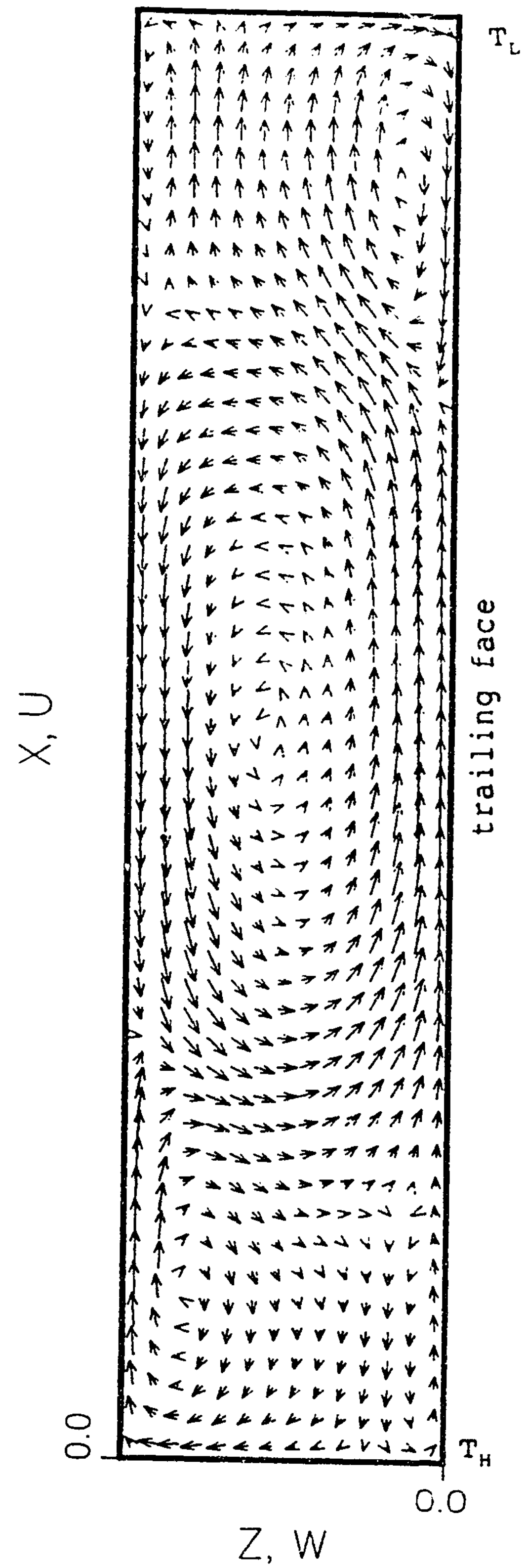

Figure 4.15 Velocity field in plane y=0.46 for Pr=0.01, at $Ra=5\times10^4$, $Ek=2\times10^{-3}$, $R_g=100$, $R_l=100$.

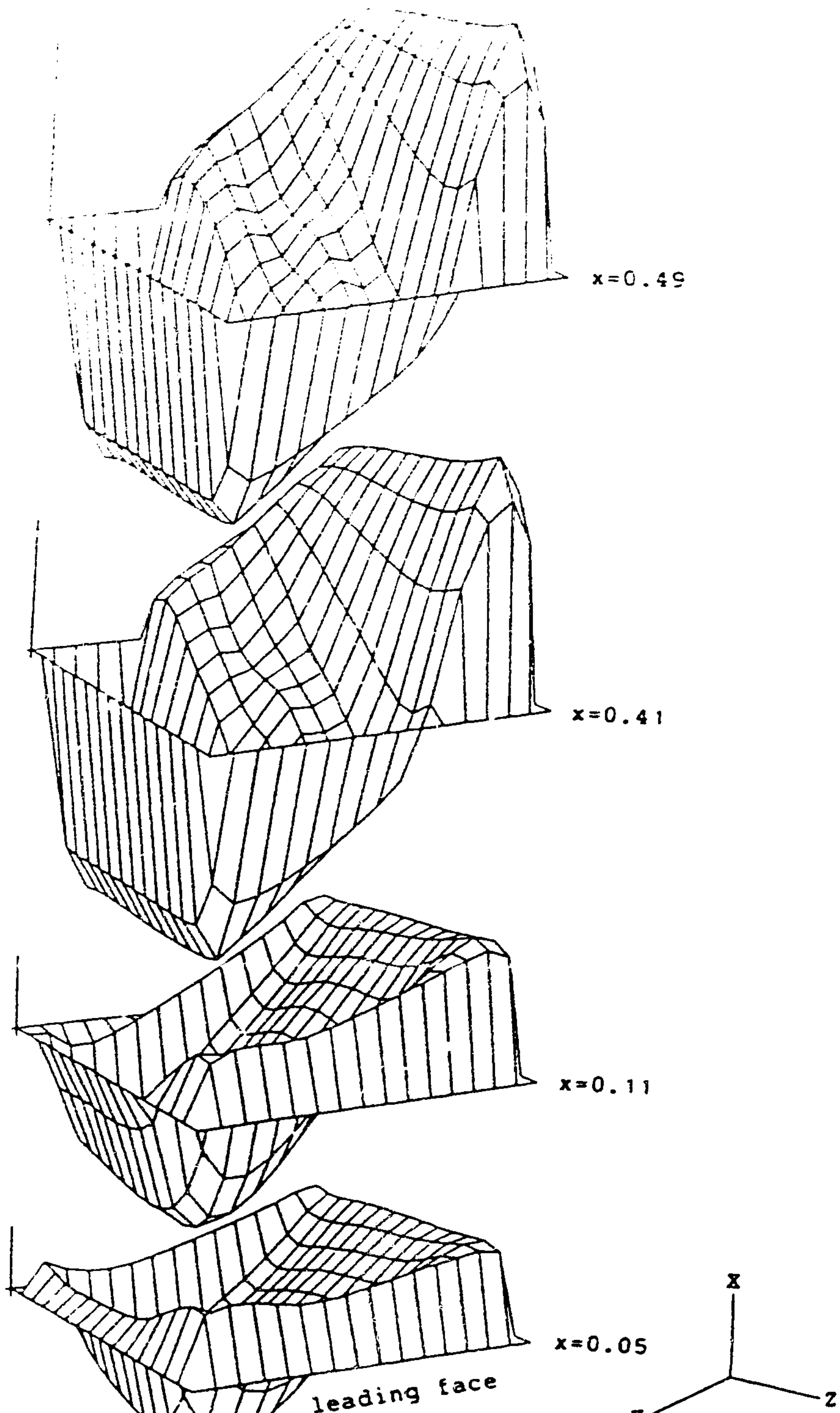

Figure 4.16 Development of the main flow velocity profile for Pr=0.01, at Ra=5×10^4, Ek=2×10^{-3}, R$_q$=100, R$_l$=100.

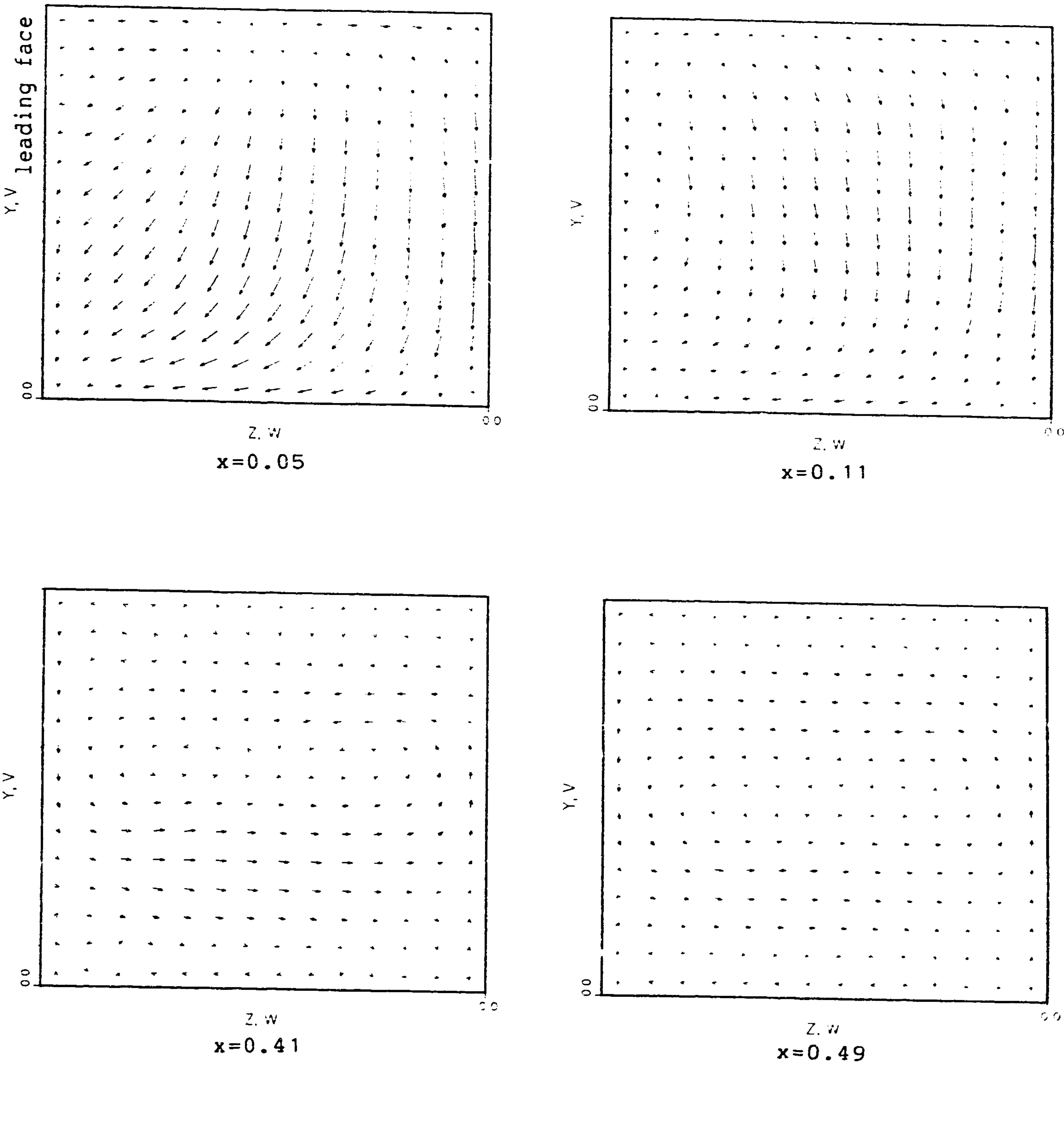

Figure 4.17 Development of the transverse velocity field for Pr=0.01, at $Ra=5\times10^4$, $Ek=2\times10^{-3}$, $R_g=100$, $R_l=100$.

from 10 to 1, the Nusselt number increases from 2.5 to 5.2 as shown in Figure 4.18.

At $R_g=1$, with other parameters constant ($Ra=5\times10^4$, $Ek=2\times10^{-3}$, $Pr=100$ and $R_1=100$), the flow pattern is similar to that at $R_g=100$. Only in the main circulation, a tendency towards annular refluent flow appears near the ends as shown in Figure 4.19 and 4.20. This is clearly due to the direct gravitational buoyancy force.

4.5 THE EFFECT OF ECCENTRICITY

For R_1 larger than 10, it was found that the centrifugal force in the Y direction can be treated as uniform, and the component of the centrifugal force in the Z direction can be neglected. The flow pattern is the same. Nusselt number is the same. For R_1 less than 10, the heat transfer rate decreases gradually. The Nusselt number drops from 2.22 at $R_1=10$ to 1.80 at $R_1=1$, and further to 1.26 at $R_1=0$ as shown in Figure 4.21.

As R_1 decreases, the centrifugal force field goes down, and has an increasing component in the Z direction. But this has little effect on the flow pattern. Even at $R_1=0$, when the inner surface coincide with the axis of rotation, the flow pattern is the same as at $R_1=100$, except it is weaker.

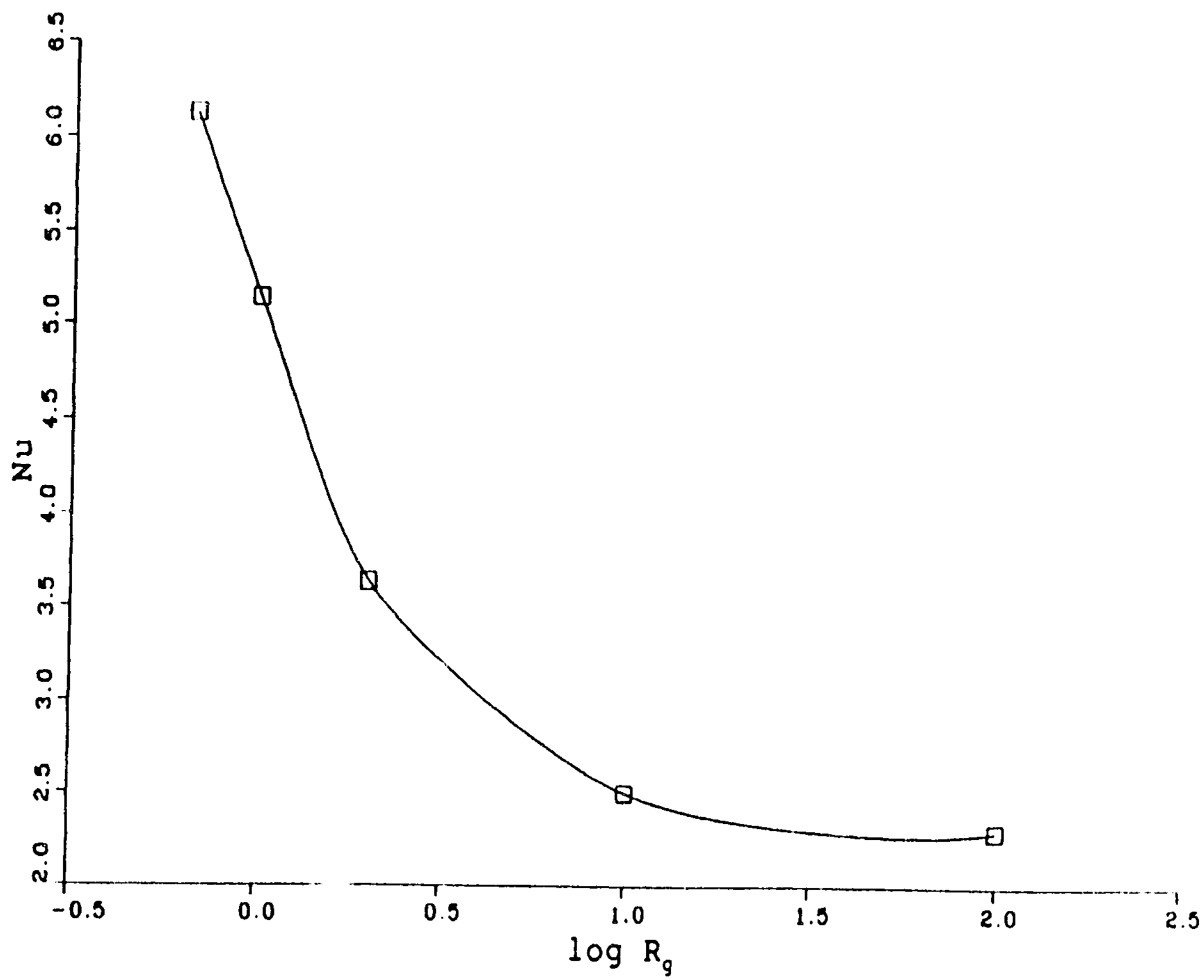

Figure 4.18 Effect of acceleration ratio on heat transfer at $Ra=5\times10^4$, $Ek=2\times10^{-3}$, $Pr=100$, $R_l=1$

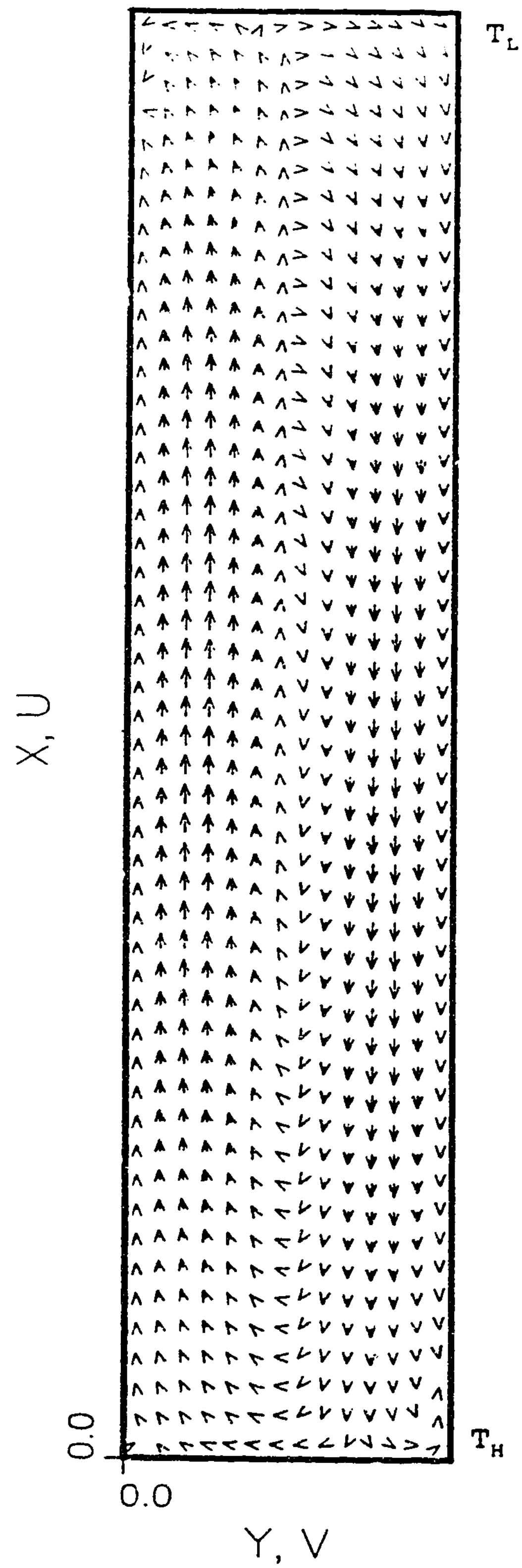

Figure 4.19 Velocity field in plane z=0.46 for R_g=1, at Ra=5×10^4, Ek=2×10^{-3}, Pr=100, R_1=100.

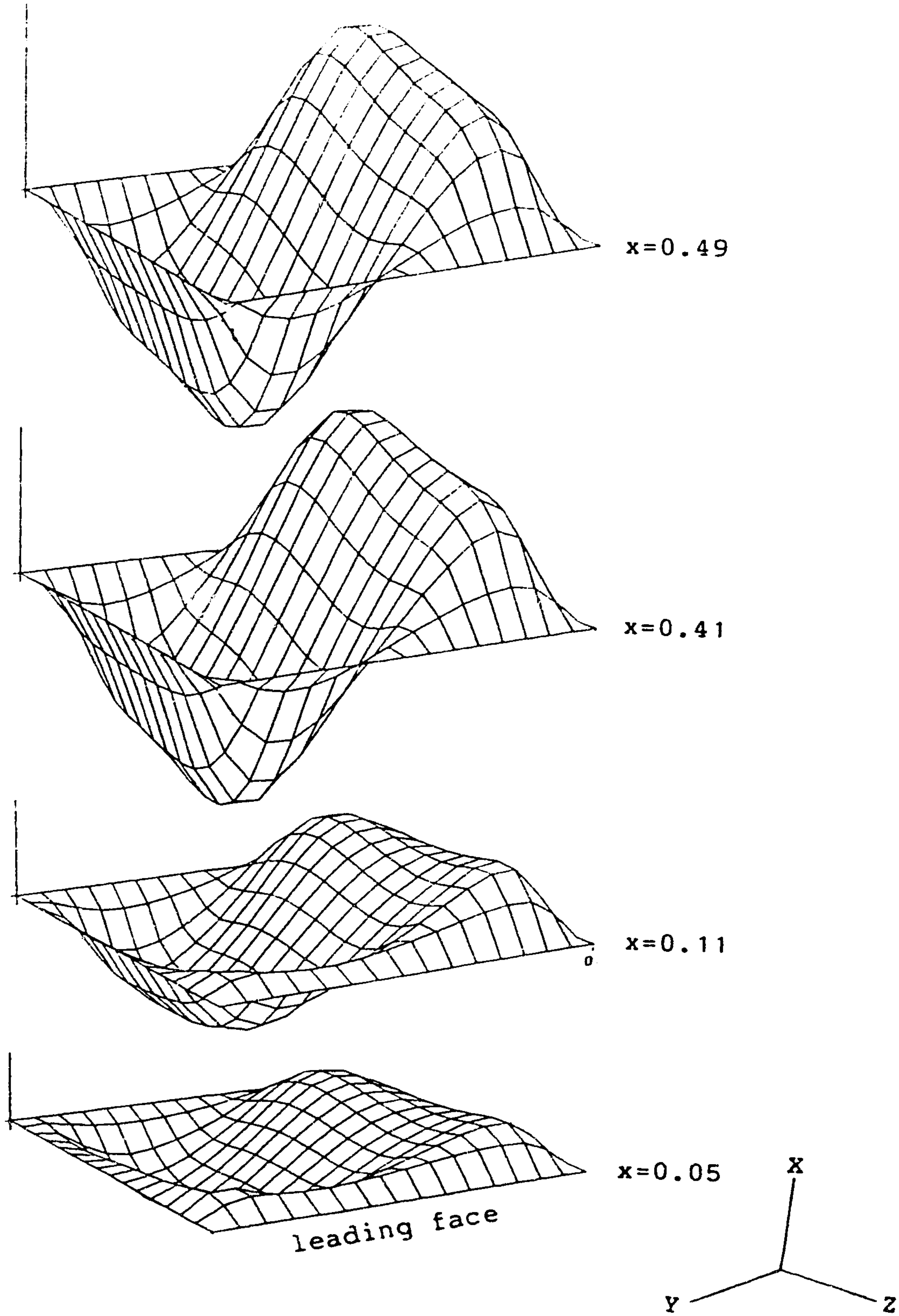

Figure 4.20 Development of the main flow velocity profile for $R_g=1$, at $Ra=5\times10^4$, $Ek=2\times10^{-3}$, $Pr=100$, $R_1=100$.

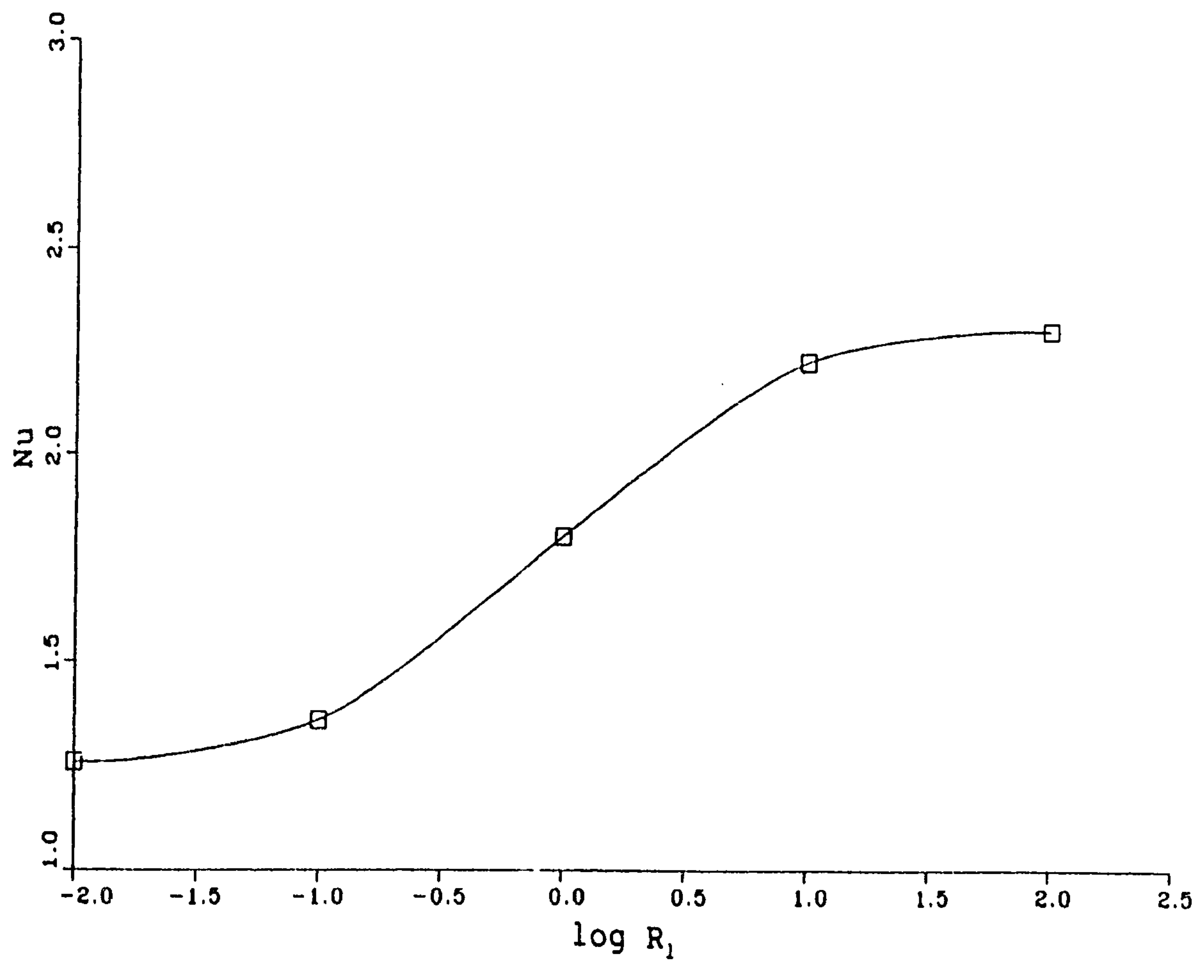

Figure 4.21 Effect of eccentricity on heat transfer at $Ra=5\times10^4$, $Ek=2\times10^{-3}$, $Pr=100$, $R_q=100$.

4.6 CONCLUSIONS

In this chapter, the flow pattern and heat transfer characteristics of the rotating eccentric thermosyphon were explored numerically.

As the thermosyphon rotates about a vertical axis parallel to its centre line, the centrifugal force will create a body force field similar to that in a horizontal stationary thermosyphon. The body force field is perpendicular to the main temperature gradient. The system is driven by indirect buoyancy force, except near the ends, and a bifilamental main circulation is formed with the cooler fluid moving down at the outer surface, and the hotter fluid moving up at the inner surface. Near the closed ends, under the influence of both the buoyancy force and the Coriolis force, an S shape secondary flow appears, and this secondary flow modifies the main flow profile.

The curve of Nusselt number against Rayleigh number is similar to that for a stationary horizontal thermosyphon in both magnitude and shape. Flow patterns are similar for all Rayleigh numbers.

For higher Ekman numbers, indicating a smaller Coriolis effect, the flow pattern is closer to that of a stationary system, and the flow is stronger. For relatively low Ekman number, buoyancy force is balanced more by Coriolis force. As a result, the main flow velocity is retarded. So the heat transfer rate drops as Ek decreases.

At low Prandtl number, the flow is complicated. Superimposed on the bi-filamental flow, there is a large cell in the mid length region with cold fluid moving down the leading face and hot fluid moving up the trailing face. The heat transfer rate increase caused by convection over conduction is less for low Prandtl number fluid.

As gravity becomes more important, an annular refluent flow appears near the ends in the main circulation due to the direct buoyancy force. The heat transfer rate is then higher.

The change of eccentricity has little effect on the flow pattern. A lower heat transfer rate occurs as R_1 decreases.

5. CONCENTRIC THERMOSYPHON

In this chapter, the behaviour of the rotating concentric thermosyphon, as illustrated in Figure 2.3 will be explored. As the system rotates about its own vertical centre line, the centrifugal force always points radially outward from the centre line. The bottom end is fixed at a high temperature and the top end is fixed at a low temperature. The body force field is perpendicular to the main temperature gradient vector. It is important to recognize that the smallness of the effective radius in a concentric thermosyphon implies a weaker flow than in the eccentric thermosyphon. This suggests that the concentric device will not likely achieve particularly high heat transfer rates.

As with the eccentric thermosyphon, the aspect ratios in the governing equations will be set at: $A_x=5$ and $A_y=1$. The parameter R_1 is always $-\frac{1}{2}$ in the concentric thermosyphon. A $51\times15\times15$ uniform mesh network was used to generate the field data.

5.1 THE EFFECT OF RAYLEIGH NUMBER

In this section, the basic flow pattern of the rotating concentric thermosyphon and the effect of Rayleigh number on heat transfer rate and fluid flow will be studied. All other parameters will be fixed: $Ek=2\times10^{-3}$, $Pr=100$, and $R_g=100$.

For sufficiently low temperature gradients, heat is transferred by conduction from the bottom hotter end to the top cooler end. As the Rayleigh number increases, e.g. the temperature difference between the two ends increases, the fluid flow gradually becomes strong enough to change the temperature distribution within the thermosyphon; the heat transfer rate then begins to increase gradually. As shown in Figure 5.1, when $Ra<10^3$ heat is transferred mainly by conduction. For Ra from $10^{4.5}$ to 10^6, the slope of the tangent of the curve is about one; this suggests that the conduction regime is succeeded by an impeded regime. Comparing with the eccentric system, the heat transfer rate is much lower, as would be expected with a smaller eccentricity.

Figure 5.2 gives three longitudinal velocity profiles for $Ra=5\times10^4$. These show that a hot core flow is flowing upward, then turning around at the top cold end and flowing downward near the sides of the tube, mainly in the four corners. The main flow profiles in Figure 5.3 give a clearer picture of such a flow pattern, and shows how the square section modifies the basic axisymmetry.

The presence of a secondary flow is evident in the flanking profiles in Figure 5.2. This flow is shown in Figure 5.4. Near the hot end (x=0.01), the fluid tends to flow radially inwards under the influence of direct thermal buoyancy, but the Coriolis force changes the flow direction, and makes the fluid spiral toward the centre. The secondary flow almost forms concentric circles. This flow propagates to about two fifths of the tube length. And at the top end,

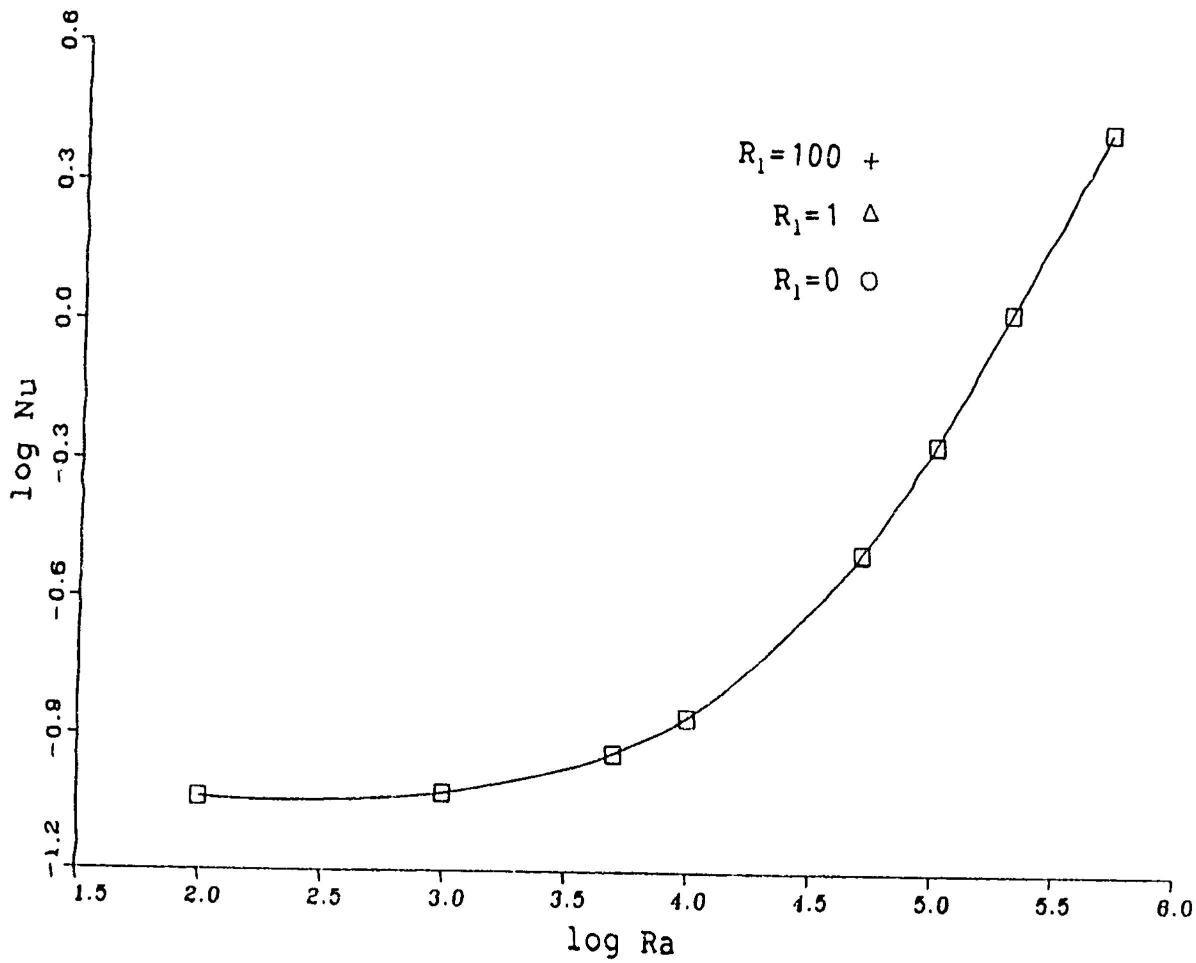

Figure 5.1 Effect of Rayleigh number on heat transfer in a concentric thermosyphon at $Ek=2\times10^{-3}$, $Pr=100$, $R_g=100$.

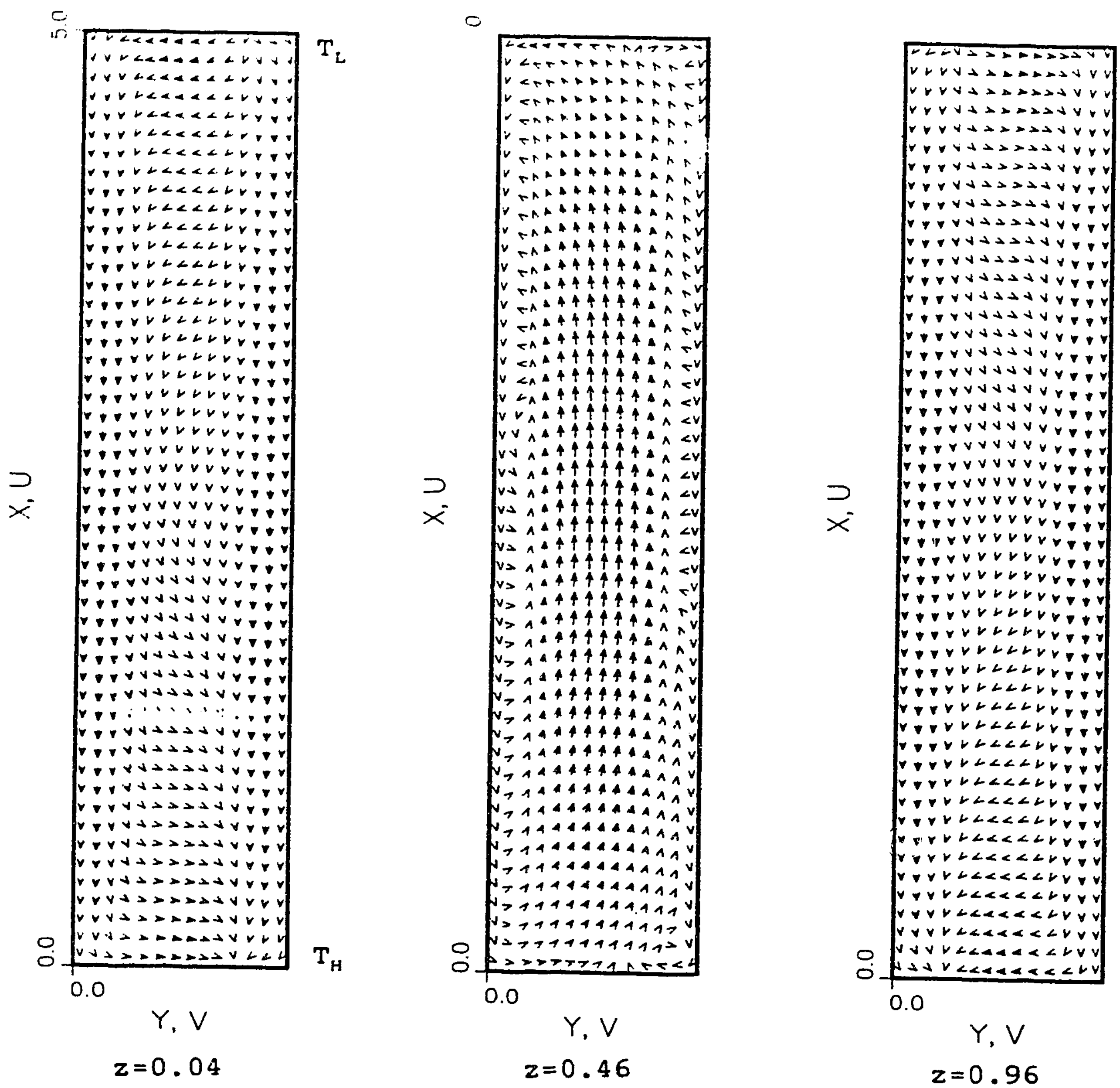

Figure 5.2 Longitudinal velocity field for $Ra=5\times10^4$ at $Ek=2\times10^{-3}$, $Pr=100$, $R_g=100$.

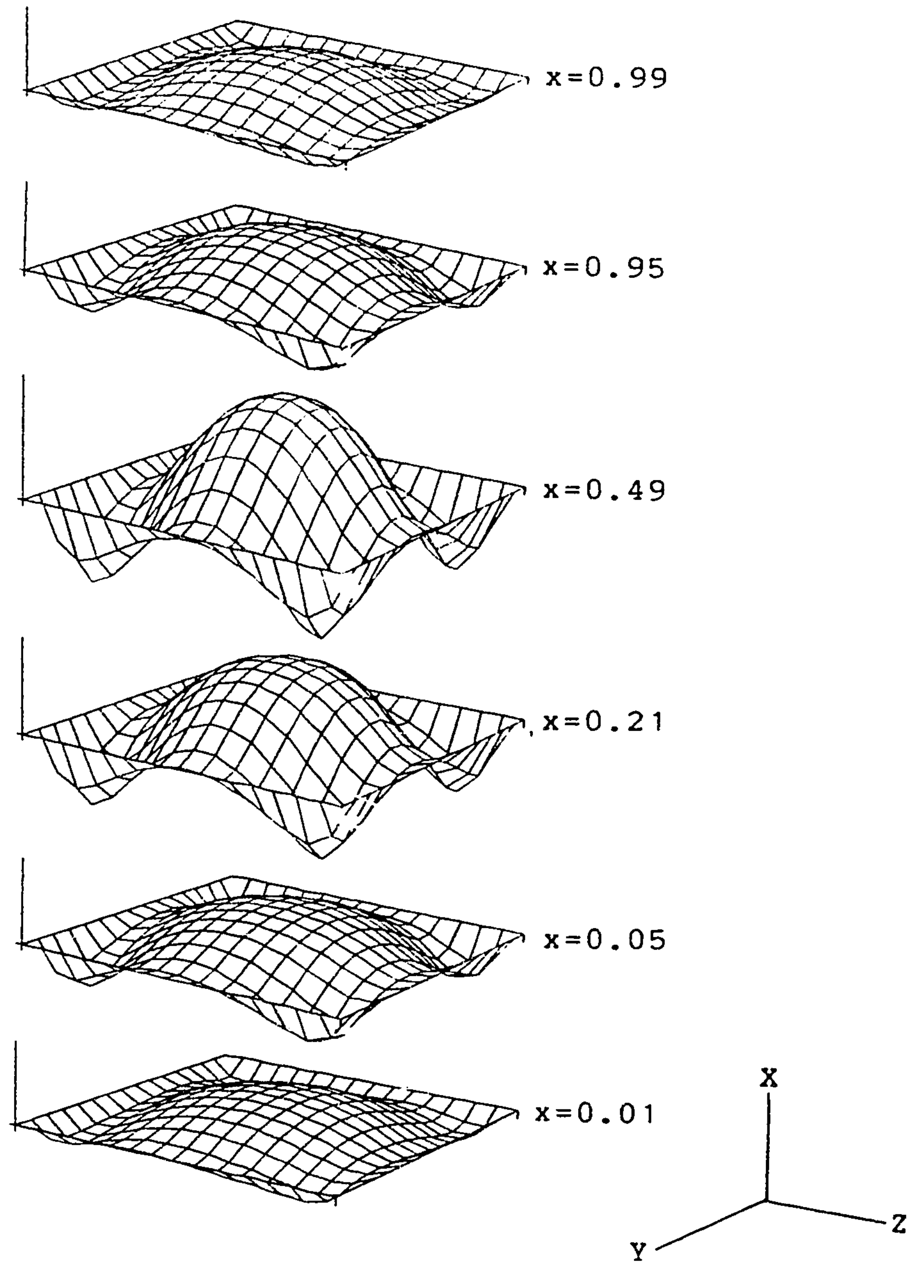

Figure 5.3 Development of the main flow velocity profile for $Ra=5\times10^4$ at $Ek=2\times10^{-3}$, $Pr=100$, $R_q=100$.

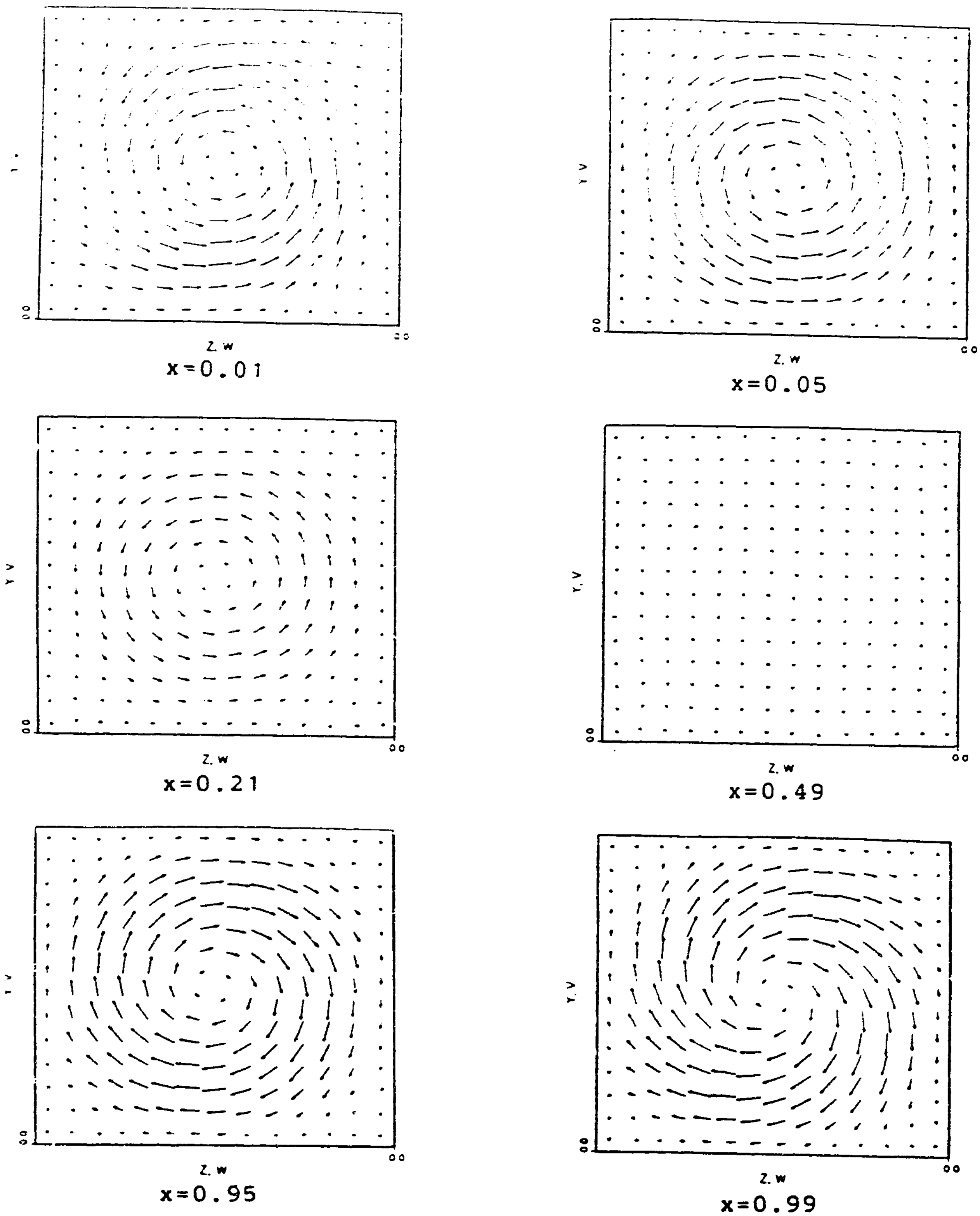

Figure 5.4 Development of the secondary flow velocity field for $Ra=5\times10^{4}$ at $Ek=2\times10^{-3}$, $Pr=100$, $R_q=100$.

an inverse circulation forms.

The primary and secondary flow patterns described above remained unchanged for all the Rayleigh numbers studied. Only the velocity magnitudes increased as the Rayleigh number was increased.

Figure 5.5 gives the surface component heat transfer rates. The heat transfer from the hot end keeps almost constant for all the Rayleigh numbers. It is the increase of heat transfer from the side walls that makes the total heat transfer rate rise. And this is purely due to convection.

5.2 THE EFFECT OF EKMAN NUMBER

Consider the flow structure first. Figure 5.6, the main flow field, Figure 5.7, the main flow profile, and the Figure 5.8, the secondary flow field, are for $Ek=2\times10^{-2}$. These indicate that the core upward flow is restricted to a narrower area, and is vigorous. The secondary flow is then much weaker because the influence of the Coriolis acceleration is smaller. This suggests that the Coriolis force gradually enters into a balance with the direct buoyancy force if Ek decreases sufficiently. The main flow is thus reduced.

The heat transfer rate increases when the Ekman number increases, as shown in Figure 5.9. The hot end heat transfer remains constant for all Ekman numbers, but heat is transferred mainly from the side walls. It is the change at the side walls which makes the total heat transfer change.

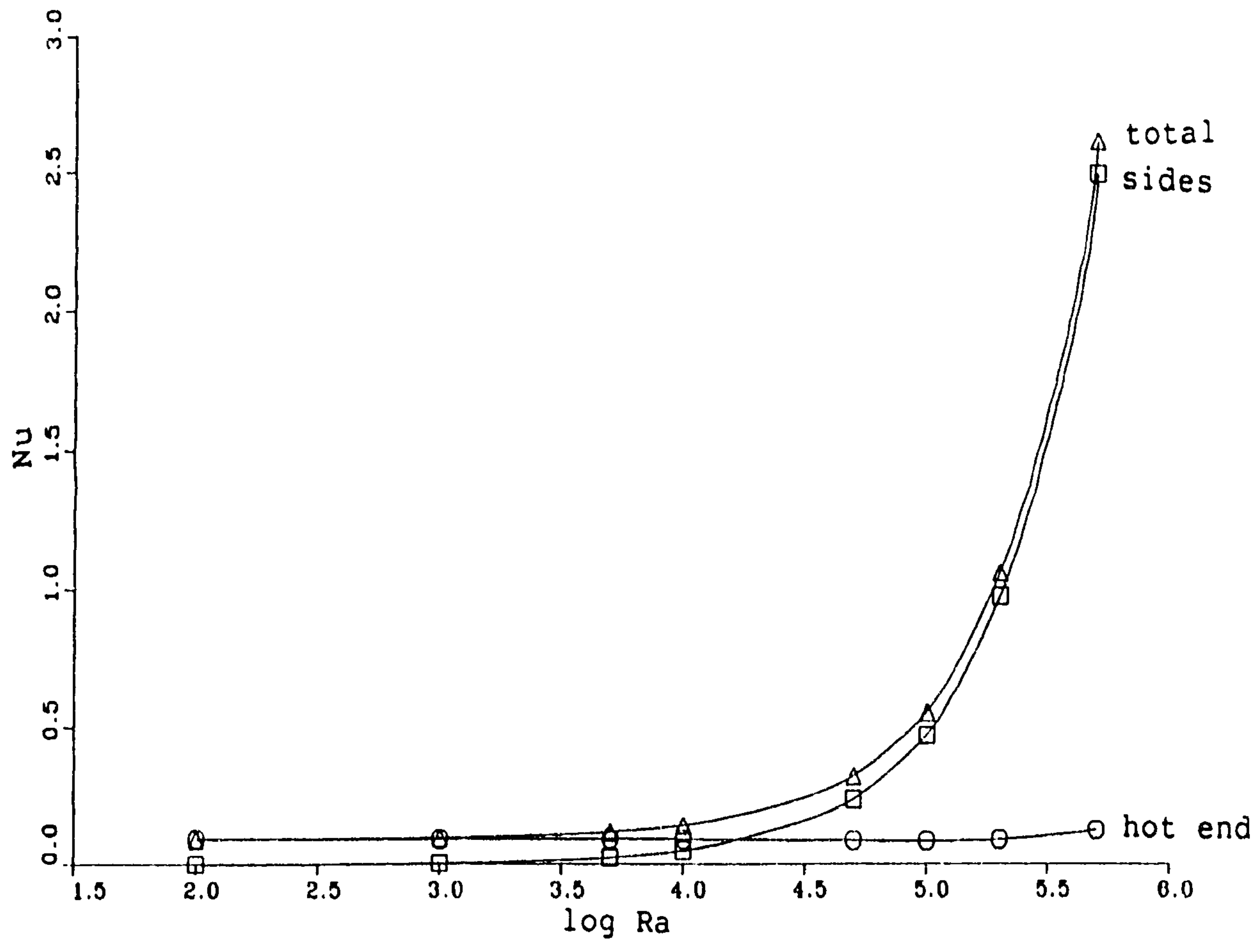

Figure 5.5 Components of the heat transfer rate

at $Ek=2\times10^{-3}$, $Pr=100$, $R_g=100$.

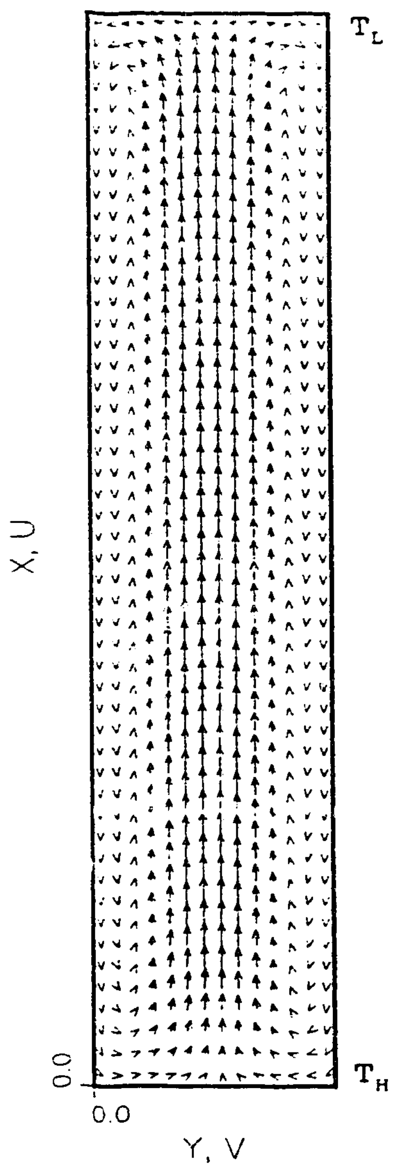

Figure 5.6 Longitudinal velocity field at z=0.46 for $Ek=2\times10^{-2}$ at $Ra=5\times10^{4}$, $Pr=100$, $R_g=100$.

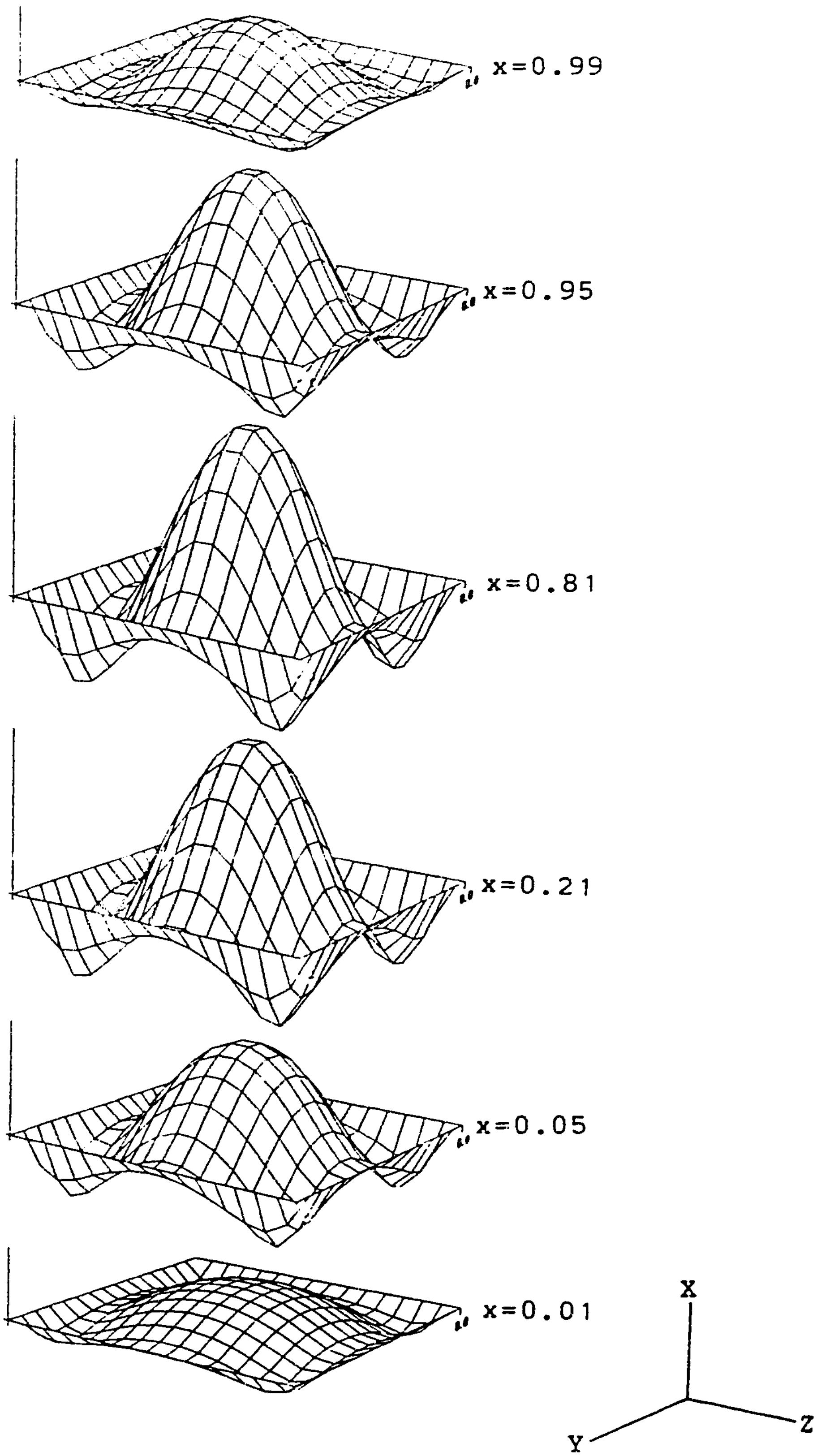

Figure 5.7 Development of the main flow velocity profile for $Ek=2\times10^{-2}$ at $Ra=5\times10^{4}$, $Pr=100$, $R_g=100$.

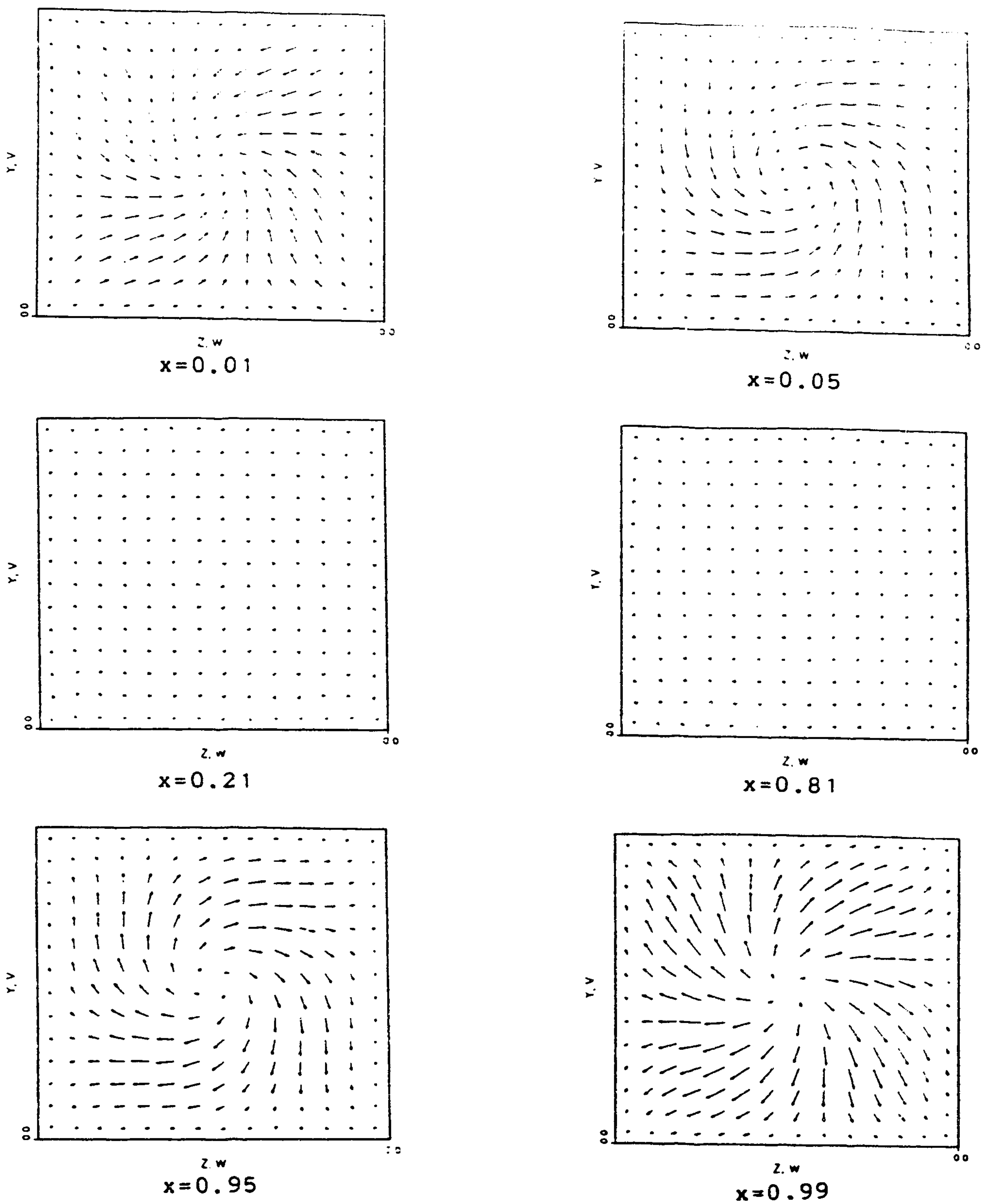

Figure 5.8 Development of the secondary flow velocity field for $Ek=2\times10^{-2}$ at $Ra=5\times10^{4}$, $Pr=100$, $R_g=100$.

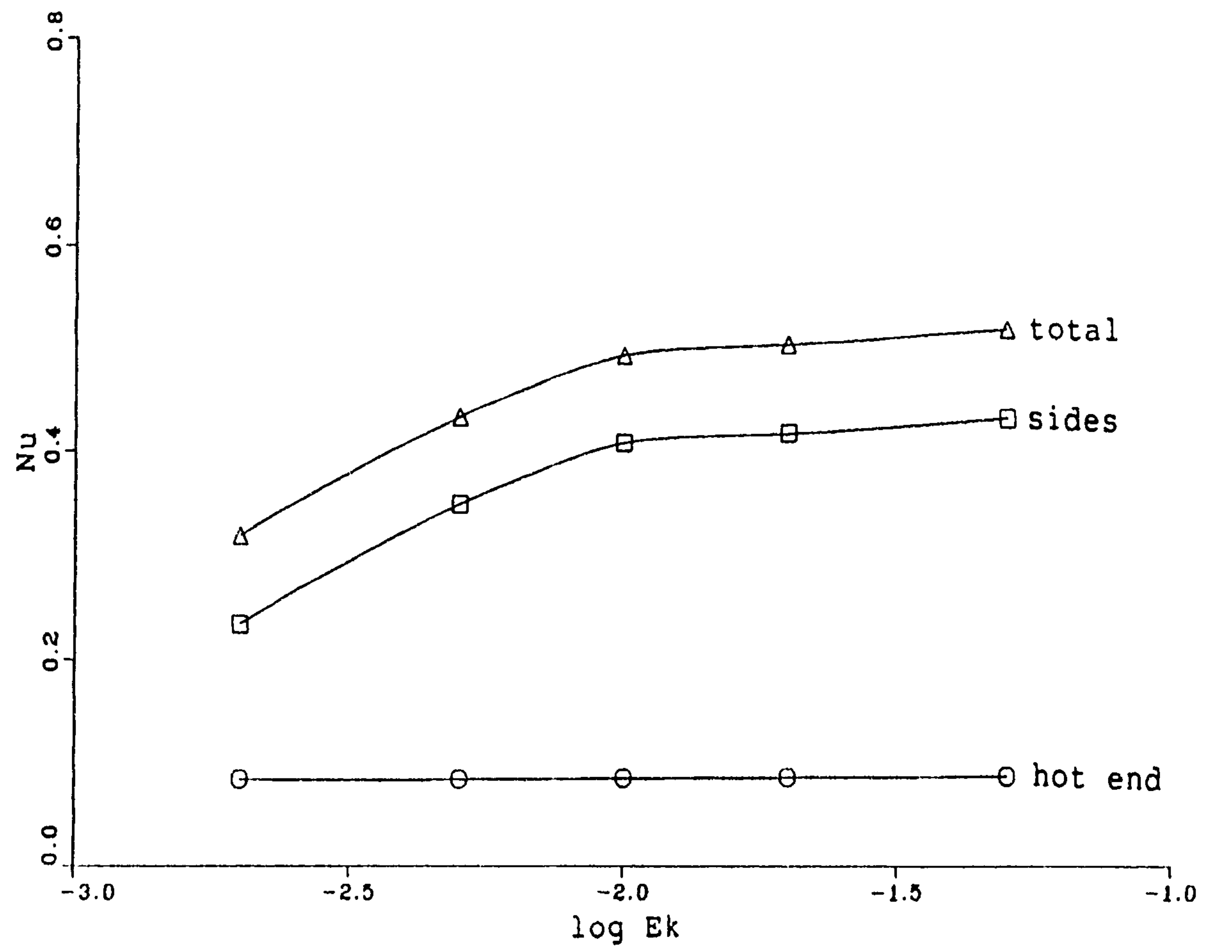

Figure 5.9 Effect of Ekman number on heat transfer at $Ra=5\times10^4$, $Pr=100$, $R_g=100$.

As Ek decreases, the spiral secondary flow caused by the Coriolis acceleration gets stronger, the longitudinal pressure gradient falls, and the main flow is reduced. As a result, the total heat transfer rate decreases as Ek decreases.

5.3 THE EFFECT OF PRANDTL NUMBER

When Pr=0.01, representing a very small viscosity, the fluid flow will be much more vigorous. In Figure 5.10, the scale is fifty times of that in Figure 5.2 when Pr=100. It is evident that the flow near the bottom end is quite similar to that in Figure 5.2, but the top end is very different. The stagnation point at the bottom end is still displaced from the centre. The main flow gradually develops towards the middle. Near the top end, the main flow is strong and has a stagnation point at the centre of the end.

Figure 5.11 and Figure 5.12 present the main flow profile and the secondary flow field, respectively. From Figure 5.12, at x=0.01, it seems that the Coriclis force is strong at the centre, and weak near the walls. A strong ring flow is formed at the centre, and this flow strongly modifies the main flow as shown in Figure 5.11. Gradually, concentric flow is developed towards the mid length plane, and beyond. At x=0.81, anticlockwise rings still exist at the centre, but clockwise flow begins to appear near the walls. Near the cold end, a diverging flow develops from the centre to the sides; the concentric ring flow found before

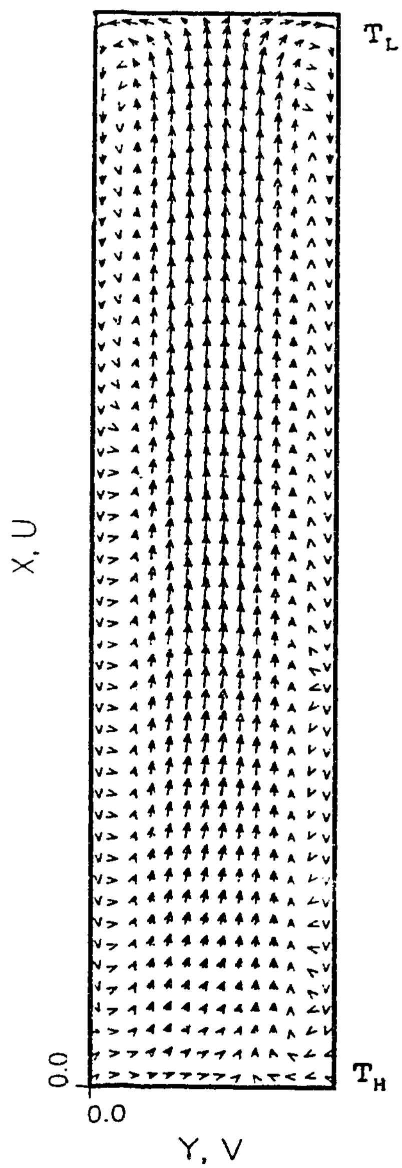

Figure 5.10 Longitudinal velocity field at z=0.46 for Pr=0.01 at Ra=5×10^4, Ek=2×10^{-3}, R_g=100.

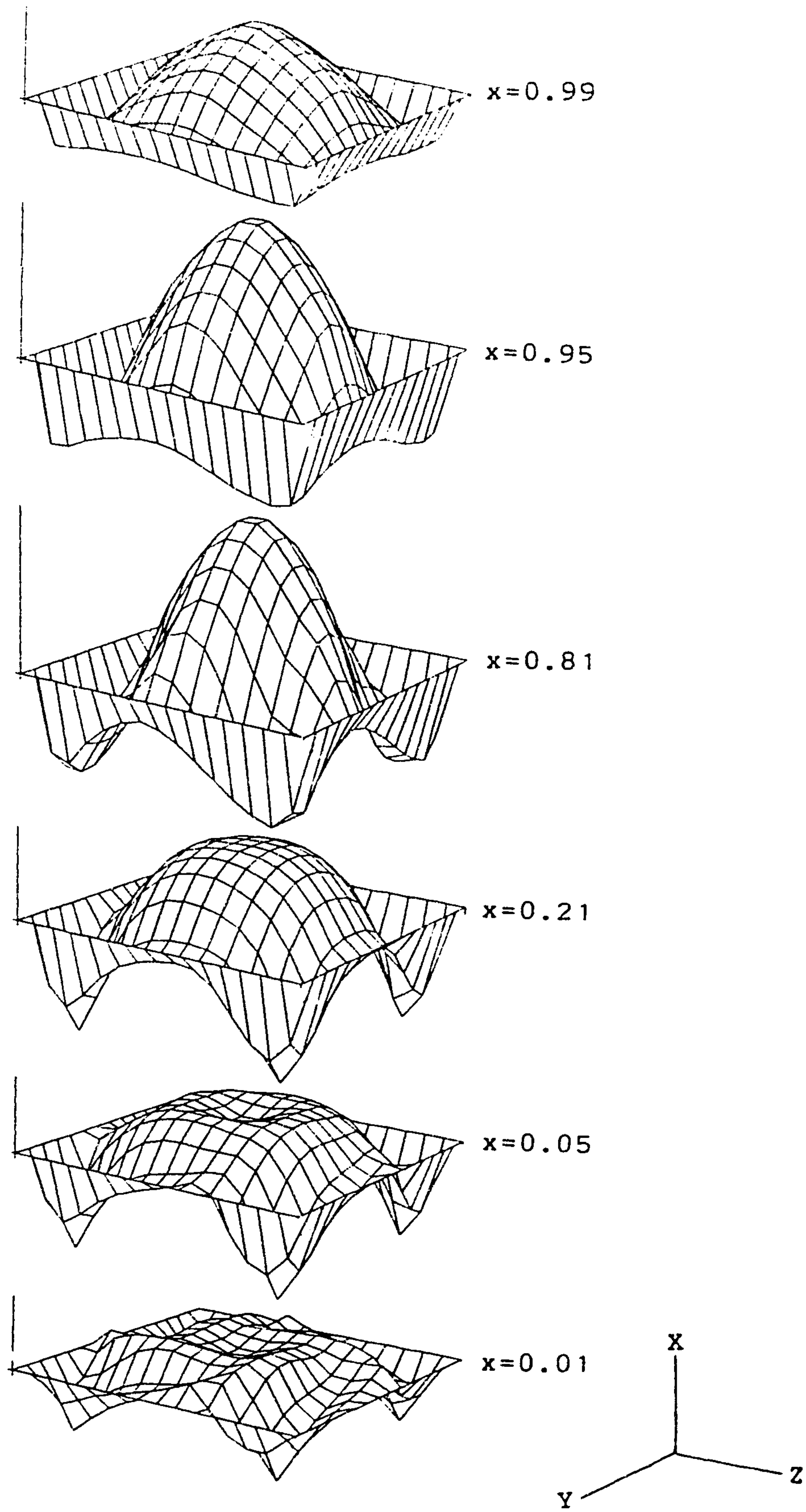

Figure 5.11 Development of the main flow velocity profile for Pr=0.01 at Ra=5×10^4, Ek=2×10^{-3}, R_g=100.

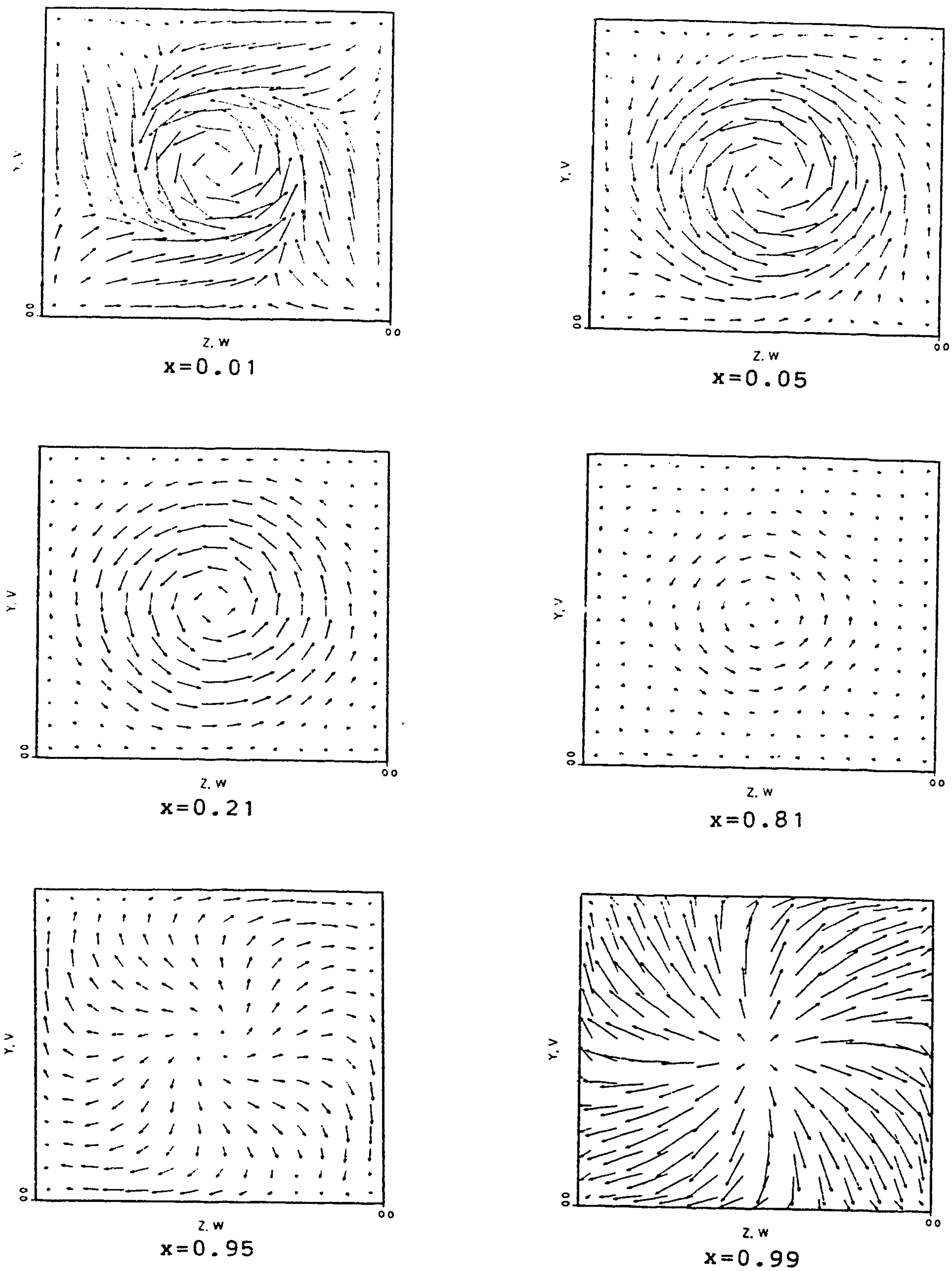

x=0.01 x=0.05 x=0.21 x=0.81 x=0.95 x=0.99

Figure 5.12 Development of the secondary flow velocity field for Pr=0.01 at $Ra=5\times10^{4}$, $Ek=2\times10^{-3}$, $R_g=100$.

is absent here.

All of this suggests that the Coriolis force does not have a equal effect on radially converging and diverging flows. When Pr<<1, inertia terms are more important, and the difference between the two ends becomes greater.

The Nusselt number was found to be constant at about 0.32 for all the Prandtl number studied, except at Pr=0.01, when it is slightly lower at 0.30. All of these are only slightly higher than the pure conduction value of 0.09.

5.4 THE EFFECT OF ACCELERATION RATIO

All of the above results were obtained for a very large acceleration ratio. For small acceleration ratios, specifically for $R_g=1$, both centrifugal and gravitational forces are important. Gravity acts directly in the main flow direction. This effect largely reinforces the main flow; as a result, the heat transfer rate is increased.

Actually, for $Ra=5\times10^4$, $Ek=2\times10^{-3}$, Pr=100, when $R_g=1$, the basic flow pattern is still the same as in Figures 5.2, 5.3, 5.4, but the flow is much stronger than at $R_g=100$. The Nusselt number is increased from 0.31 at $R_g=100$ to 1.07 at $R_g=1$, as illustrated in Figure 5.13.

5.5 CONCLUSIONS

Flow patterns and heat transfer rates in the concentric thermosyphon were explored in this chapter.

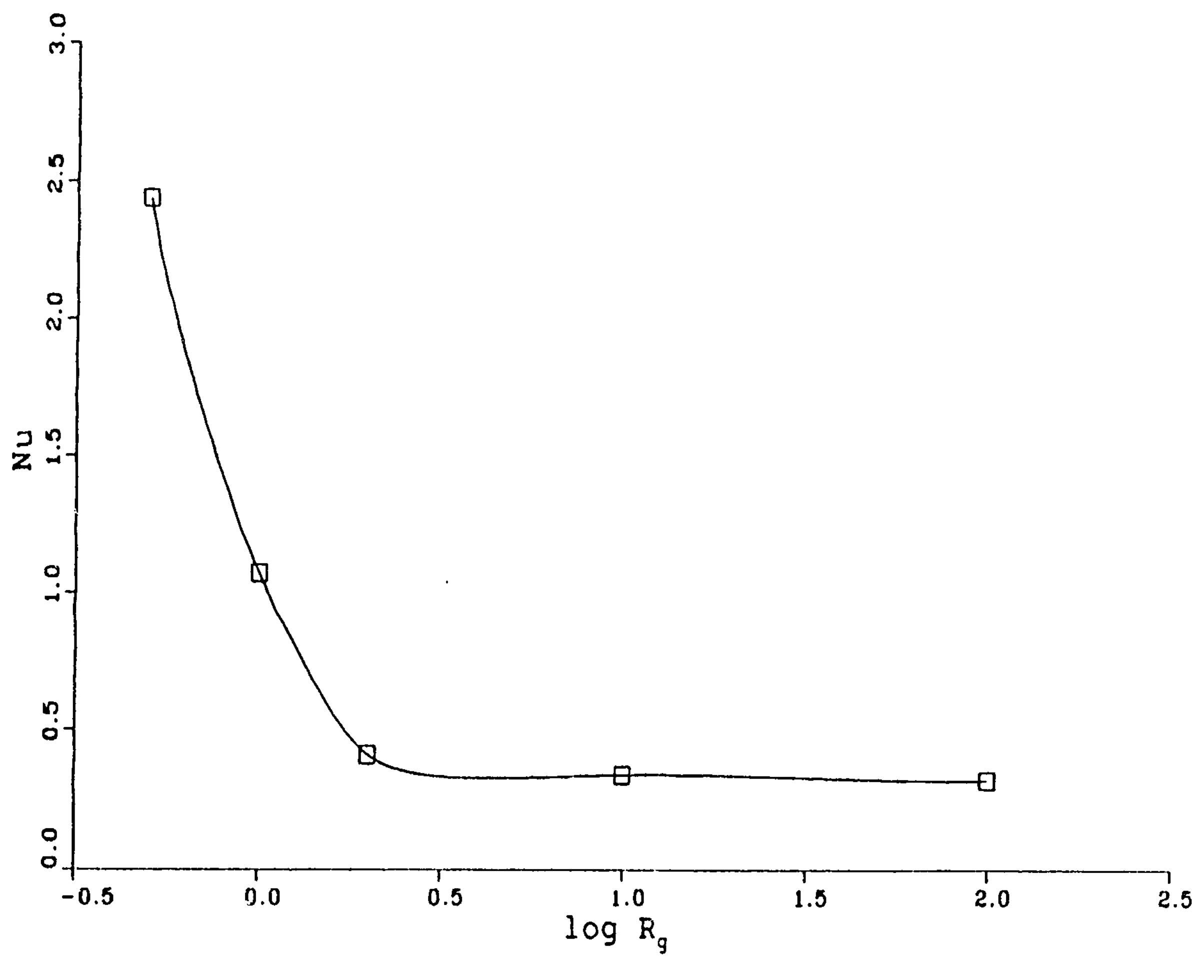

Figure 5.13 Effect of acceleration ratio on heat transfer at $Ra=5\times10^4$, $Ek=2\times10^{-3}$, $Pr=100$.

As the thermosyphon rotates about its vertical centre line, the centrifugal force always points radially outward. Hot fluid moves upward in the central core, and cold fluid moves downward near the walls, especially in the four corners. The converging flow at the hot end is twisted by Coriolis force to form a anticlockwise secondary flow, and the diverging flow at the top cold end is also twisted to form a clockwise secondary flow.

Varying the Rayleigh number evidently does not change the basic flow pattern. The plot of Nu~Ra indicates that heat is transferred mainly from the side walls, and it is the increase from the side walls that makes the total heat transfer rise between conduction and impeded flow regime.

As Ek decreases, the Coriolis force eventually balances the pressure gradient, and the main flow is reduced. Thus for a higher Ekman number, the main flow is more vigorous and the heat transfer rate is higher.

For very small Prandtl numbers, the fluid flow is much more vigorous. The different effects of Coriolis force on converging flow and diverging flow is important. The anticlockwise flow at the hot bottom end propagates almost to the cold end. The Nusselt number is almost constant for all Prandtl numbers.

Smaller acceleration ratios enhance the main flow, and the heat transfer rate increases accordingly.

6. GENERAL CONCLUSIONS AND RECOMMENDATIONS

The behaviour of square section rotating closed thermosyphons was studied numerically under single-phase, laminar flow conditions. Detailed flow patterns and heat transfer characteristics were described for radial, eccentric and concentric tubes rotating about a vertical axis. Effort was given to further understanding of the physical process of the rotating thermosyphon.

The flow pattern in a radial thermosyphon consists of an annular refluent flow near the two closed ends combined with a bifilamental flow in the mid length region. A distinctive feature of the rotating radial thermosyphon is that the Coriolis force may flatten the axial velocity profile, making it look almost two-dimensional.

In an eccentric thermosyphon, a bifilamental main circulation is formed; superimposed on that is an S-shaped secondary flow induced near the ends by buoyancy and Coriolis forces. This secondary flow modifies the main flow profile.

As expected, the flow pattern of a concentric thermosyphon consists of a central core in which the hot fluid moves towards the cold end and an annular flow in which the cold fluid moves towards the hot end. Under the Coriolis force, a converging ring flow at the hot end and a diverging ring flow at the cold end are formed as the secondary flow.

The Nu~Ra curves of the three thermosyphons are plotted in Figure 6.1. The plots indicate that an impeded regime succeeds the conduction regime for all the three types; and they suggest that a boundary layer regime succeeds the impeded regime in radial and eccentric thermosyphons at least. The heat transfer rate of the concentric thermosyphon is much lower than that of the radial and eccentric due to weak body force field.

The Nu~Ek curves for the three thermosyphons are plotted in Figure 6.2. It is clear that when Ek decreases, the heat transfer rate has a maximum for radial thermosyphon, whereas the heat transfer rates decrease monotonically for eccentric and concentric thermosyphons. At about $Ek=10^{-2}$, the heat transfer rate for all three types begins to drop quickly when Ek decreases further; the variation for the concentric thermosyphon is relatively small.

It seems that in order to fully describe the thermal and hydrodynamic regimes of a rotating thermosyphon, in addition to the Nu~Ra curve, the plot of Nu~Ek is also needed. The flow regime is thus defined by both Ra and Ek. As the Ekman number decreases, the Coriolis force plays a bigger role.

The lowest Ek for which a converged solution can be obtained is about 2×10^{-3} for all three types. Some preliminary probing for the radial thermosyphon with lower Ek suggests that a new flow pattern may form, and the heat

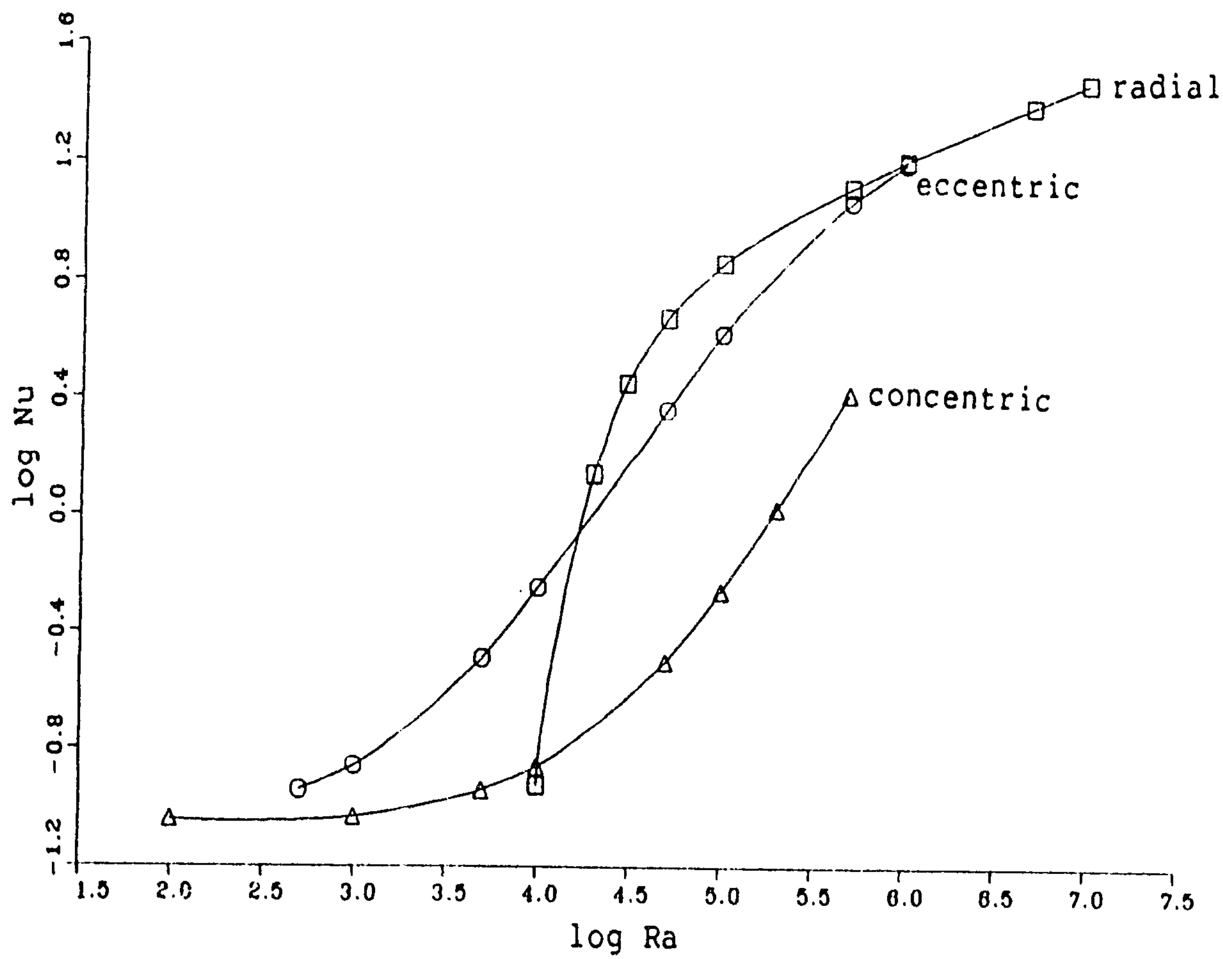

Figure 6.1 Comparison of the effect of Rayleigh number on heat transfer for three different thermosyphons at $Ek=2\times10^{-3}$ (for radial, $Ek=5\times10^{-3}$), $Pr=100$, $R_g=100$, $R_l=100$.

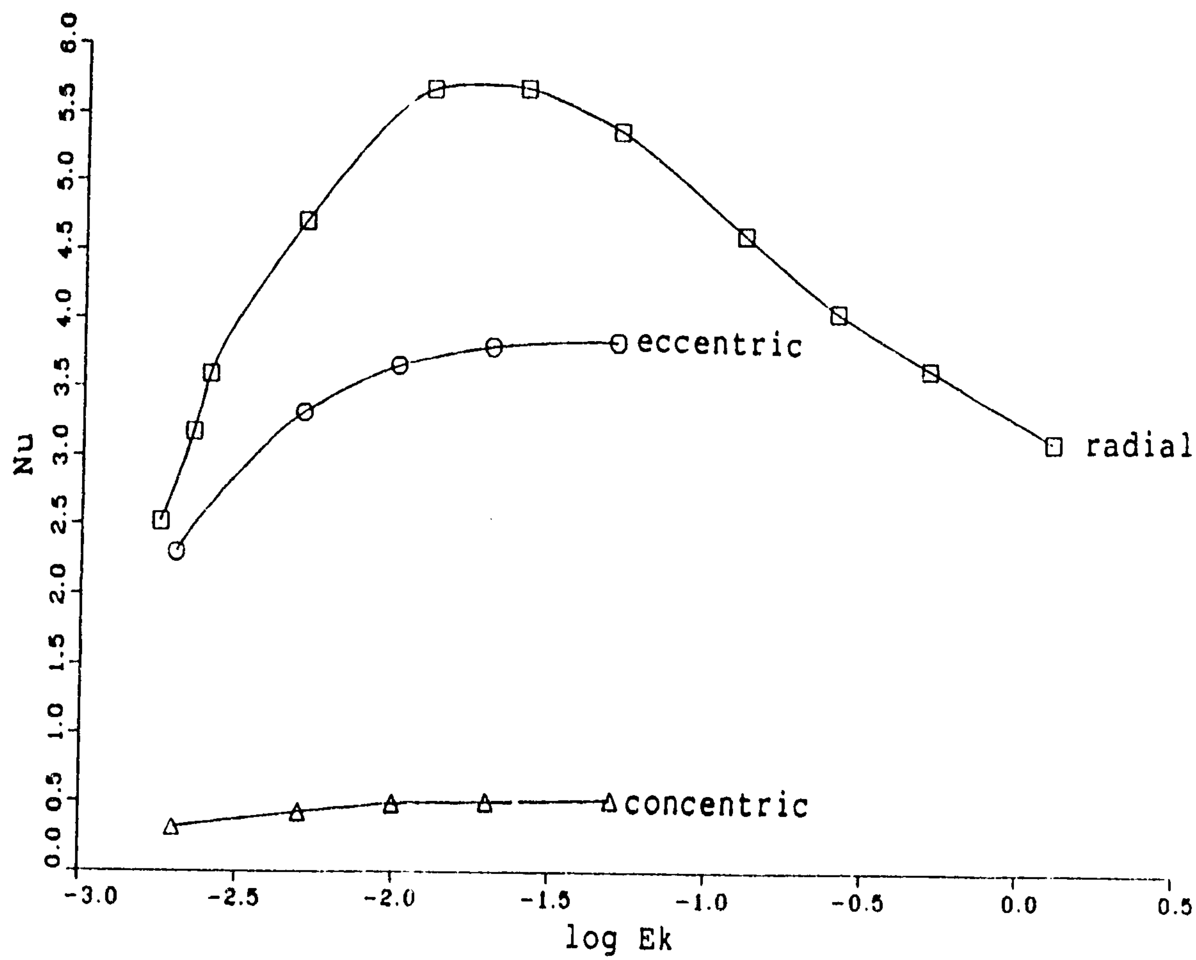

Figure 6.2 Co..parison of the effect of Ekman number on heat transfer for three different thermosyphons at $Ra=5\times10^4$, $Pr=100$, $R_g=100$, $R_l=100$.

transfer rate may then jump to a much higher value.

Flow patterns and Nusselt numbers change very little for Pr>>1. For Pr=0.01, however, flow is much more vigorous, and Nu is lower.

As gravity becomes important, heat transfer rates are higher, and the flow pattern may be modified accordingly.

When eccentricity becomes smaller, the heat transfer rates are lower due to a weaker body force field. The heat transfer rate of concentric thermosyphon is the lowest.

As a result of this study, several recommendations for future work may be made:

1) For engineering application, the practical Ekman number range is from 10^{-2} to 10^{-7}. Investigation of the physical process for Ekman number in this entire range is needed.
2) For large temperature differences, or high rotating speeds, the Rayleigh number is high, and the flow may not be laminar. Turbulance behaviour of the rotating thermosyphon is worth exploring.
3) The aspect ratio of a practical thermosyphon might be quite large. The behaviour of large aspect ratio (length over diameter) thermosyphons should be investigated.

REFERENCES

1. Japikse,D., Advances in thermosyphon technology, Advances in Heat Transfer, Vol.9, pp.2-111, 1973.

2. Holzwarth, H., Die Entwicklung der Holzwarth-Gasturbine, Holzwarth-Gasturbine, Gmbh Muellheim - Ruhr, 1938.

3. Schmidt, E., Heat transmission by natural convection at high centrifugal acceleration in water-cooled gas turbine blades, Proc. Inst. Mech. Eng. A.S.M.E. (London) Conf. Proc., pp.361-363, 1951.

4. Cohen, H. and Bayley, F.J., Heat transfer problems of liquid-cooled gas-turbine blades, Proc. of the Inst. Mech. Eng., Vol.169, No.53, pp.1063, 1955.

5. Davis, T.H. and Morris, W.D., Heat transfer characteristics of a closed loop rotating thermosyphon, Third International Heat Transfer Conference Proceedings, Vol.2, pp.172-181, 1966.

6. Thoren, F., Heat pipe cooled induction motors, Tsukuta, pp.365-371, 1984.

7. Polasek, F., Cooling of a.c. motor by heat pipes, Proc. 1st International Heat Pipe Conference, Stuttgart, 1973.

8. Lock, G.S.H., The Tubular Thermosyphon: Variations on a Theme, Oxford University Press, (in preparation).

9. Catton, I., Natural convection in enclosures, 6th International Heat Transfer Conference, Vol.6, pp.13, 1979.

10. Lock, G.S.H., Heat transfer studies of the closed thermosyphon, Ph.D Thesis, University of Durham, Appl. Sci., Durham, England, 1962.

11. Bayley,F.J. and Lock, G.S.H., Heat transfer characteristics of the closed thermosyphon, Trans. ASME C: J. Heat Transfer, Vol.87, pp.30-40, 1965.

12. Japikse, D., Heat transfer in open and closed thermosyphons, Ph.D. Thesis, Purdue University, Lafayette, Indiana, 1969.

13. Japikse, D., Jallouk, P.A. and Winter, E.R.F., Single-phase transport processes in the closed thermosyphon, Int. J. Heat Mass Transfer, Vol.14, pp.869-887, 1971.

14. Japiske, D. and Winter, E.R.F., Heat transfer and flow in the closed thermosyphon, Proc. Int. Heat Transfer Conf., 4th, Paper NC2.9, 1970.

15. Mallinson, G.D., Graham, A.D. and de Vahl Davis, G., Three-dimensional flow in a closed thermosyphon, J. Fluid mechanics, Vol.109, pp.259-275, 1981.

16. Crespo, E., Bontoux, P., Smutek, C., Roux, B., Hardin, G., Sani, R., Rosenberger, F., Three-dimensional simulations of convection regimes in cylindrical ampoules. Comparisons with theoretical analysis and experiments, Proc. 6th European Symposium on Material Sciences under microgravity conditions, Bordeaux, France, pp.529-537, 1987.

17. Lock,G.S.H. and Zhao, Litong, The laminar flow field in a near-vertical, closed tube thermosyphon, Mathematical and Computer Modelling, Vol.14, pp.822-825, 1990.

18. Cormack, D.E., Leal, L.G. & Imberger, J., Natural convection in a shallow cavity with differentially heated endwalls. Part 1: Asymptotic theory, J. of Fluid Mechanics, Vol.65, pp.209-229,1974.

19. Cormack, D.E., Leal, L.G. & Seinfield, J.N., Natural convection in a shallow cavity with differentially heated endwalls. Part 2: Numerical solutions, J. of Fluid Mechanics, Vol.65, pp.231-246, 1974.

20. Imberger, J., Natural convection in a shallow cavity with differentially heated endwalls. Part 3: Experimental results, J. of Fluid Mechanics, Vol.65, pp.247-260, 1974.

21. Bejan, A. & Tien, C.L., Laminar natural convection heat

transfer in a horizontal cavity with different end temperatures, Trans. ASME C: J. Heat Transfer, Vol.100, pp.641-647, 1978.

22. Bejan, A. & Tien, C.L., Fully developed natural counterflow in a long horizontal pipe with different end temperatures, Int. J. Heat Mass Transfer, Vol.21, pp.701-708, 1978.

23. Ostrach, S., Loka, R.R. & Kumar, A., Natural convection in low aspect ratio rectangular enclosures, Natural Covection in Enclosures, HTD-8, pp.1-10, ASME, 1980.

24. Schiroky,G.H. & Rosenberger, F., Free convection of gases in a horizontal cylinder with differentially heated end walls, Int. J. Heat Mass Transfer, Vol.27, pp.587-598, 1984.

25. Smutek, C., Bontoux, P., Roux, B., Schiroky, G.H., Hurford., A.C., Rosenberger, F., de Vahl Davis, G., Three-dimensional convection in horizontal cylinders: numerical solutions and comparison with experimental and analytical results, Numerical Heat Transfer, Vol.8, pp.613-631, 1985.

26. Bontoux, P., Smutek, C., Roux, B., Lacroix, J.M., Three-dimensional buoyancy-driven flows in cylindrical cavities with differentially heated endwalls. Part 1. Horizontal cylinders, J. Fluid Mechanics, Vol.169, pp.211-227, 1986.

27. Bontoux, P., Roux, B., Schiroky, G.H., Markham, B.L., and Rosenberger, F., Convection in the vertical midplane of a horizontal cylinder. Comparison of two-dimensional approximations with three-dimensional results, Int. J. Heat Mass Transfer, Vol.29, pp.227-240, 1986.

28. Han, Jianchiu, Orientational effects in a buoyant cavity flow, M.Sc thesis, University of Alberta, 1988.

29. Lock, G.S.H., Han, J.-C., Buoyant laminar flow of air in a long, square-section cavity aligned with the ambient temperature gradient, J. Fluid Mech., Vol.207, pp.489-504, 1989.

30. Lock, G.S.H., and Zhao, Litong, Natural convection in honeycomb wall spaces, Int. J. Heat Mass Transfer, (in press).

31. Brown, T.W.F., CIMAC CONGR. Zurich, pp443-484, 195 .

32. Ogale, V.A., On the application of the semi-closed thermosyphon system to gas turbine blade cooling, Dr. Thesis, Technological University of Delft, Delft, Netherlands, 1968.

33. Bontoux, P., Smutek, C., Randriamampianina, A., Roux, B., Extremet, G.P., Hurford, A.C., Rosenberger, F. and De Vahl Davis, G., Numerical solutions and experimental results for three dimensional buoyancy driven flows in tilted cylinders, Adv. Space Res., Vol.6, No.5, pp.155-160, 1986.

34. Lock, G.S.H. and Kirchner, J.D., Some characteristics of the inclined, closed tube thermosyphon under low Rayleigh number conditions, Int. J. Heat Mass Transfer, (in press).

35. Tritton D.J., Physical Fluid Dynamics, Van Nostrand Reinhold Company, 1977.

36. Chenoweth, D.R. and Paolucci, S., Natural convection in a vertical air layer with large horizontal temperature differences, J. Fluid Mechanics, Vol.169, pp.173, 1986.

37. Patankar, S.V., Numerical Heat Transfer and Fluid Flow, McGraw-Hill, 1980.

38. Van Doormaal, J.P. and Raithby, G.D., Enhancements of the SIMPLE method for predicting incompressible fluid flows, Numer. Heat Transf., Vol.7, pp.147-163, 1984.

39. Mallinson, G.D. and de Vahl Davis, G., Three-dimensional natural convection in a box: a numerical study, J. Fluid Mech., Vol.83, pp.1-31, 1977.

40. Kheshgi, H.S. and Scriven, L.E., Viscous flow through a rotating square channel, Phys. Fluids, Vol.28, pp.2968-2979, 1985.

41. Speziale, C.G., Numerical study of viscous flow in rotating rectangular ducts, J. Fluid Mech., Vol.122, pp.251-271, 1982.

42. Greenspan, H.P., The Theory of Rotating Fluids, Cambridge University Press, 1969.

43. Gray, Donald D. and Giorgini, Aldo, The validity of the Boussinesq approximation for liquids and gases, Int. J. Heat Mass transfer, Vol.19, pp.545-551, 1976.

44. Glatz, Gerry, Free convection from a horizontal surface, M.Sc thesis, University of Alberta, 1966.

BIBLIOGRAPHY

Andivg, T.A., Rotating rig experiments on the effectiveness of the closed thermosyphon system for the cooling of turbine rotor blades, PAMERTRADA Contract Rep. #C108, 1956.

Ballback, L.J., The operation of a rotating wickless heat pipe, M.S. Thesis, Naval Postgraduate School, Monterey, 1969.

Bejan, A. and Tien, C.L., Fully developed conterflow in a long horizontal pipe with different end temperatures, Int J. Heat Mass Transfer., vol.21, pp.701-708, 1978.

Bejan, A., Al-Hamoud, A.A. and Imberger, J., Experimental study of high-Rayleigh number convection in a horizontal cavity with different end temperatures, J. Fluid Mech., vol.109, pp.283-299, 1981.

Bontoux, P., Smutek, C., Roux, B. and Lacroix, J.M., Three dimensional buoyancy-driven flows in cylindrical cavities with differentially-heated endwalls. Part I. Horizontal cylinders, J. Fluid Mech., vol.169, pp.211-227, 1986.

Boussinesq, J., Theorie Analytique de la Chaleur, Gauthier-Villars, vol.2, pp.172, 1903.

Brooks, I. and Ostrach, S., An experimental investigation of natural convection in a horizontal cylinder, J. Fluid Mech., vol.44, pp.545-561, 1970.

Daniels,.. and Al-Jumaily, F.K., Investigations of the factors affecting the performance of a rotating heat pipe, Int. J. Heat Mass Transfer, vol.18, pp.961-973, 1975.

Daniels, T.C. and Williams, R.J., Experimental temperature distribution and heat load characteristics of rotating heat pipes, Int. J. Heat Mass Transfer, vol.21, pp.193-201, 1978.

Davis, S.H., Convection in a box: linear theory, J. Fluid Mech., vol.30, pp.465-478, 1967.

de Vahl Davis, G., Finite difference methods for natural and mixed convection in enclosures, Proc. 8th Int. Heat Transfer. Conf., (San Francisco), Hemisphere Pub. Corp., vol.1, pp190-199, 1986.

Duck, P.W., Flow through rotating straight pipes of a circular cross section, Phys. Fluids, vol.26, pp.614-618, 1983.

Hart, J.E., Stability of the flow in a differentially heated inclined box, J. Fluid Mech., vol.47, pp.547-582, 1971.

Hart, J.E., Observations of complex oscillations in a closed thermosyphon, J. Heat Transfer, vol.107, pp.833-839, 1985.

Hoogendoorn, C.T., Natural convection in enclosures, Proc. 8th Int. Heat Transfer Conf., (San Francisco), Hemisphere Pub. Corp., vol.1, pp.111-120, 1986.

Jaluria, Y., Natural Convection Heat and Mass Transfer, Pergamon Press, Oxford, 1980.

Kimura, S. and Bejan, A., The boundary layer natural convection regime in a rectangular cavity woth uniform heat flux from the side, J. Heat Transfer, vol.106, pp.98-103, 1984.

Lee, Y. and Bedrossian, A., The characteristics of heat exchangers using heat pipes or thermosyphons, Int. J. Heat Mass Transfer, vol.21, pp.221-229, 1978.

Linthorst, S.J.M., Schinkel, W.M.M. and Hoogendoorn, C.J., Flow structure with natural convection in inclined air-filled enclosures, J. Heat Transfer, vol.103, pp.535-539, 1981.

Lock, G.S.H. and Kirchner, J.D., Performance of an air-filled, open thermosyphon tube with particular reference to wind augmentation, Int. J. Heat Mass

Transfer, vol.31, pp.2357-2364, 1988.

Lock, G.S.H. and Liu, Y., The effect of geometry on the performance of the closed tube thermosyphon at low Rayleigh numbers, Int. J. Heat Mass Transfer, vol.32, pp.1175-1182, 1989.

Lock, G.S.H., Chong, K., Dyckerhoff, A., Huyer, J. and Jones, B., On the design of wind-augmented thermosyphons, Cold Regions Science and Technology, vol.16, pp.11-23, 1989.

Lock, G.S.H. and Kirchner, J.D., Wind augmented heat transfer in an open thermosyphon tube with large length-diameter ratios, J. Heat Transfer, vol.112, pp.71-77, 1990.

Majcen, M. and Sarunac, N., Heat pipe cooled twin airfoil blade as an element for higher efficiency of long life gas turbine, Heat and Mass Transfer in Rotating Machinery, (eds. Metzger, D.E. and Afgan, N.H.), Hemisphere Pub. Corp., Washington, pp.689-700, 1984.

Martin, B.W. and Cresswell, D.J., Influence of Coriolis forces on heat transfer in the open thermosyphon, The Engineer, vol.204, pp.926-930, 1957.

Martini, W.R. and Churcuill, S.W., Natural convection inside a horizontal cylinder, A.I.Ch.E. J., vol.6, pp.251-257, 1960.

Marto, P.J., Performance characteristics of rotating, wickless heat pipes, Proc. 2nd Int. Heat Pipe Conf., (Bologna), PP.281-291, 1976.

Marto, P.J. and Wahenseil, L.L., Augmenting the condenser heat transfer performance of rotating heat pipes, AIAA Journal, vol.17, No.6, pp.647-652, 1979.

Marto, P.J. and Weigel, H., The development of economical rotating heat pipes, Advances in Heat Pipe Technology, Proc. 4th Int. Heat Pipe Conf., (London), pp.709-723, 1982.

Marto, P.J., Rotating heat pipes, in Heat and Mass Transfer in Rotating Machinery, (eds. Metzger, D.E. and Afgan, N.H.), Hemisphere Pub. Washington, pp.609-632, 1984.

Metzger, D.E. and Afgan, N.H., (eds), Heat and Mass Transfer in Rotating Machinery, Hemisphere Pub., Washington, 1984.

Morrison, G.L. and Tran, V.Q., Laminar flow structure in vertical free convectiove cavities, Int. J. Heat Mass Transfer, vol.106, pp.203-213, 1978.

Nakayama, W., Ohtsuka, Y., Itoh, H. and Yoshikawa, T., Optimum charge of working fluids in horizontal rotating heat pipes, Heat and Mass Transfer in Rotating Machinery, (eds Metzger, D.E. and Afgan, N.H.), Hemisphere Pub. Washington, pp.633-644, 1984.

Niekawa, J., Matsumoto, K., Koisumi, T., Hasegawa, K., Kaneko, H. and Mizoguchi, Y., Performance of revolving heat pipes and application to a rotary heat exchanger, Advances in Heat Pipe Technology, Pergamon Press, Oxford, pp.225-234, 1982.

Ostrach, S., Natural convection in enclosures, J. Heat Transfer, vol.110, pp.1175-1189, 1988.

Pokorny, B., Polasek, F., Schneller, J. and Stulc, P., Heat transfer in co-axial and parallel rotating heat pipes, Proc. 5th Int. Heat Pipe Conf., (Tsukuba), vol.4, pp.90-98, 1984.

Raithby, G.D. and Hollands, K.G.T., Natural convection, Handbook of Heat Transfer, (eds. Rohsenow, W.M. et al.), McGraw-Hill, New York, 1984.

Schneller, J., Pokorny, B. and Polasek, F., Heat transfer in rotating co-axial and parallel heat pipes and their application in machinery, Heat and Mass Transfer in Rotating Machinery, (eds. Metzger, D.E. and Afgan, N.H.), Hemisphere Pub. Washington, pp.669-687, 1982.

Shiroky, G.H. and Rosenberger, F., Free convection of gases in a horizontal cylinder with differentially-heated endwalls, Int. J. Heat Mass Transfer, vol.27, pp.587-598, 1984.

Simpkins, P.G. and Chen, K.S., Convection in horizontal cavities, J. Fluid Mechanics, vol.166, pp.21-39, 1986.

Vasiliev, L.L. and Khrolenok, V.V., Centrifugal coaxial heat pipes, Proc. 2nd Int. Heat Pipe Conf., (Bologna), PP.293-302, 1976.

Yang, H.Q., Yang, K.T. and Lloyd, J.R., Flow transition in a three-dimensional tilted rectangular enclosure, Proc. 8th Int. Heat Transfer Conf., (San Francisco), vol.4, 1495-1500, 1986.

Yang, H.Q., Yang, K.T. and Lloyd J.R., Laminar natural convection flow transitions in tilted three-dimensional longitudinal rectangular enclosures, Int. J. Heat Mass Transfer., vol.3, pp.1637-1644, 1987.

Yang, H.Q., Yang, K.T. and Lloyd, J.R., Three dimensional bimodel flow transitions in tilted enclosures, Int. J. Heat Mass Transfer, vol.9, pp.90-97, 1988.

Yang, K.T., Transitions and bifurcations in laminar buoyant flows in confined enclosures, J. Heat Transfer, vol.110, pp.1191-1204, 1988.

Yang, W., (ed), Heat Transfer and Fluid Flow in Rotating Machinery, Hemisphere Pub., Washington, 1987.

Zarling, J.P., Haynes, F.D. and Daly, S.F., On the application of thermosyphon in cold regions, Proc. 7th Int. Conf. on Offshore Mechanics and Arctic Eng., vol.IV, pp.280-286, 1988.

APPENDIX A CONSISTENCY AND ACCURACY OF THE PROGRAM

Accuracy analysis is important in numerical calculation, especially for a complicated problem where experimental data are unavailable for comparison. The question concerning computational solutions is what guarantee can be given that the computational solution will be close to the exact solution of the partial differential equations. If the exact solution is known explicitly, this might be easier to answer. For most practical problems, such as the problem in this work, the exact solution of the partial differential equations can not be obtained analytically, the exact error caused by using numerical approximation is therefore unknown. We have to look for alternatives. There are some techniques that may be used to estimate the accuracy of the approximate solution.

The SIMPLE method is based on the central-difference scheme, and the power-law scheme is used to impove it. So a higher than second-order accuracy is expected.

One technique for assessing accuracy is to obtain solutions on successively refined grids and to check that the solution is not changing to some predetermined accuracy. This method is easier to perform for a uniform grid system. Since a non-uniform grid system was used for the radial thermosyphon, while a uniform grid system was used for eccentric and concentric thermosyphons, the eccentric thermosyphon was chosen as a representative to estimate the accuracy of the numerical approximation.

All the data used in this thesis were obtained by using a FPS-164 Scientific Computer, but the grid test was carried out on an IBM Risc 6000 computer. For eccentric thermosyphon, at $Ra=5\times10^4$, $Ek=2\times10^{-3}$, $Pr=100$, $R_g=100$, $R_l=100$, different uniform grid sizes were used to generate field data. It was found that all the grids tested were equally good at catching the general features of the flow structure. Comparison of velocity in the x direction and total Nusselt number are given at different grid sizes in Table A.1.

	grid	$u(\times10^{-2})$	$\Delta u/u(\%)$	Nu	$\Delta Nu/Nu(\%)$
FPS-164	51×15×15	0.4207	0.0	2.3019	0.0
IBM Risc 6000	41×15×15	0.4716	12.1	2.4542	6.6
	51×15×15	0.4463	6.1	2.3686	2.9
	101×15×15	0.4406	4.7	2.3608	2.6
	51×19×19	0.4311	2.5	2.2997	-0.1
	51×29×29	0.4286	1.9	2.2429	-2.6

Table A.1 Data comparison from different grid sizes.

For a practical fluid flow problem, especially a complex problem such as the refluent flow here, a minimum practical grid is required to depict the flow structure. It was found that at least 13 points were needed in the y and z directions. Effort was not given to find out the practical minimum in the x direction; however less than 41 points may cause untolerable error. It seems that the grid system

5×15×15 used to generate field data is a fair compromise between solution accuracy and computational efficiency.

Another method available to estimate truncation error is the Richardson-type Extrapolation. For three different mesh sizes,

$$\Delta x_1 \times \Delta y_1 \times \Delta z_1$$
$$\Delta x_2 \times \Delta y_2 \times \Delta z_2$$
$$\Delta x_3 \times \Delta y_3 \times \Delta z_3$$

If $\Delta y_i = \Delta z_i$, i=1,2,3, the exact solution ψ may be written as

$$\psi = \psi_i + C_1 \Delta x_i^m + C_2 \Delta y_i^n \qquad i=1,2,3 \qquad \text{(A.1)}$$

where ψ_i is the numerical solution from mesh size $\Delta x_i \times \Delta y_i \times \Delta z_i$; and C_1 and C_2 are independent of Δx_i and Δy_i. Writing (A.1) in different mesh sizes

$$\psi = \psi_1 + C_1 \Delta x_1^m + C_2 \Delta y_1^n \qquad \text{(A.2.1)}$$

$$\psi = \psi_2 + C_1 \Delta x_2^m + C_2 \Delta y_2^n \qquad \text{(A.2.2)}$$

$$\psi = \psi_3 + C_1 \Delta x_3^m + C_2 \Delta y_3^n \qquad \text{(A.2.3)}$$

We thus have

$$\frac{\psi_1 - \psi_2}{\psi_2 - \psi_3} = \frac{C_1[\Delta x_2^m - \Delta x_1^m] + C_2[\Delta y_2^n - \Delta y_1^n]}{C_1[\Delta x_3^m - \Delta x_2^m] + C_2[\Delta y_3^n - \Delta y_2^n]} \qquad \text{(A.3)}$$

If $\Delta y_1 = \Delta y_2 = \Delta y_3$, (A.3) becomes

$$\frac{\psi_1 - \psi_2}{\psi_2 - \psi_3} = \frac{\Delta x_2^m - \Delta x_1^m}{\Delta x_3^m - \Delta x_2^m} \qquad \text{(A.4)}$$

Using the data of u from 41×15×15, 51×15×15, 101×15×15 in Table A.1, the above non-linear equation (A.4) can be solved numerically. The m is estimated as

$$m = 8$$

If $\Delta x_1 = \Delta x_2 = \Delta x_3$, (A.3) becomes

$$\frac{\psi_1 - \psi_2}{\psi_2 - \psi_3} = \frac{\Delta y_2^n - \Delta y_1^n}{\Delta y_3^n - \Delta y_2^n} \qquad (A.5)$$

Using the data of u from 51×15×15, 51×19×19, 51×29×29 in Table A.1, n is solved numerical as

$$n = 8$$

The exact solution ψ may be represented as:

$$\psi = \psi_1 + C_1 \Delta x_1^8 + C_2 \Delta y_1^8 \qquad (A.6)$$

This means that, for a relatively coarse grid size, a more accurate solution may be obtained by reducing the grid size; below a certain point, the accuracy of the solution may not be improved substantially by further reducing the grid size.

For better accuracy and stability control, two levels of control were implemented in the program. The first level of control is in the form of the average local residual of the corresponding algebraic equations. The second level of control is in the form of the relative change in the dependent variables for two consecutive iterations. The criterion for the second level of control was 0.01, while the criterion for the first level of control was 0.005 for u, v, w, ϕ, and $10^{-7} \times 0.5^{m}$ for p, where m = NINT[N/10] (N is the iteration number). A higher criterion for p was necessary for convergence and stability. Usually less than 100 iterations were needed to obtain one solution. That is about 2 hour CPU time on FPS-164 computer.

APPENDIX B

```
C     THIS IS A PROGRAM SOLVING NATURAL CONVECTION PROBLEMS
C                    IN RADIAL ROTATING SYSTEM
C
      PARAMETER(N=15,M=51,L=15,NN=N+1,MM=M+1,LL=L+1)
      PARAMETER(NP=N-1,MP=M-1,LP=L-1)
      DIMENSION UP(N,MM,LL),VP(NN,M,LL),WP(NN,MM,L)
      DIMENSION T(NN,MM,LL),PP(NN,MM,LL),P(NN,MM,LL)
      DIMENSION U(N,MM,LL),V(NN,M,LL),W(NN,MM,L),GRADT(NN)
      DIMENSION DX(NN),DY(MM),DZ(LL),AP3(2:N,2:M,2:L)
      DIMENSION Y(M),Z(L)
      DIMENSION PX(NN),QX(NN),PY(MM),QY(MM),PZ(LL),QZ(LL)
      DIMENSION
     +AP1(2:N,2:M,2:L),AP2(2:N,2:M,2:L),S(2:N,2:M,2:L)
      DIMENSION
     +AE(2:N,2:M,2:L),AW(2:N,2:M,2:L),AN(2:N,2:M,2:L)
      DIMENSION
     +AS(2:N,2:M,2:L),AT(2:N,2:M,2:L),AB(2:N,2:M,2:L)
      DIMENSION
     +PSB(2:N,2:L),QSB(2:N,2:L),ANB(2:N,2:L),CNB(2:N,2:L)
      DIMENSION
     +PWB(2:M,2:L),QWB(2:M,2:L),AEB(2:M,2:L),CEB(2:M,2:L)
      DIMENSION
     +PBB(2:N,2:M),QBB(2:N,2:M),ATB(2:N,2:M),CTB(2:N,2:M)
      DIMENSION SEB(2:M,2:L),SNB(2:N,2:L),STB(2:N,2:M)
C
C     CALL SYS$DISEXC(0,0,0,4)
C
      OPEN(5,FILE='D1')
      READ(5,*)AX,AZ
      READ(5,*)RA,PRD,EK,RG,RL
      READ(5,*)ALFV
      READ(5,*)TOLV1,TOLV2,TOLT1,TOLT2,TOLP
      READ(5,*)(DX(I),I=1,NN)
      READ(5,*)(DY(J),J=1,MM)
      READ(5,*)(DZ(K),K=1,LL)
      READ(5,*)NCR,NCCR,AMP
C
      Y(1)=DY(1)
      Z(1)=DZ(1)
      DO 21 J=2,M
   21 Y(J)=Y(J-1)+DY(J)
```

```
      DO 23 K=2,L
   23 Z(K)=Z(K-1)+DZ(K)
C
      AA1=1.0/(1.0-ALFV)
C
      AX2=AX*AX
      AZ2=AZ*AZ
      RY=1.0/(SQRT((2.0*PRD)/RA))
      RX=RY*AX2
      RZ=RY*AZ2
      AXI=1.0/AX
      AXI2=AXI*AXI
      AZI=1.0/AZ
      AZI2=AZI*AZI
      RK=SQRT((2.0*PRD)/(RA*EK**2))
C
      GX=1.0/RX
      GY=1.0/RY
      GZ=1.0/RZ
      GTZ=GZ/PRD
      GTX=GX/PRD
      GTY=GY/PRD
      NCOUNT=0
      NCC=0
C
C        INPUT INITIAL GUESSED VALUES FOR U, V, W AND T
C
      OPEN(4,FILE='IN')
      READ(4,11)(((UP(I,J,K),I=1,N),J=1,MM),K=1,LL)
      READ(4,11)(((VP(I,J,K),I=1,NN),J=1,M),K=1,LL)
      READ(4,11)(((WP(I,J,K),I=1,NN),J=1,MM),K=1,L)
      READ(4,11)(((T(I,J,K),I=1,NN),J=1,MM),K=1,LL)
      READ(4,11)(((PP(I,J,K),I=2,N),J=2,M),K=2,L)
C
      DO 22 K=1,LL
      DO 22 J=1,MM
      DO 22 I=1,N
   22 U(I,J,K)=UP(I,J,K)
C
      DO 24 K=1,LL
      DO 24 J=1,M
      DO 24 I=1,NN
   24 V(I,J,K)=VP(I,J,K)
```

```
C
      DO 26 K=1,L
      DO 26 J=1,MM
      DO 26 I=1,NN
   26 W(I,J,K)=WP(I,J,K)
C
C
C          APPLY BOUNDARY CONDITIONS
C
      GRADT(1)=-1.0
      DO 33 J=1,M
   33 GRADT(J+1)=GRADT(J)+DY(J)+DY(J+1)
C
      DO 45 K=2,L
      DO 45 I=2,N
      PSB(I,K)=0.0
      ANB(I,K)=1.0
   45 CNB(I,K)=0.0
C
      DO 50 K=2,L
      DO 50 J=2,M
      PWB(J,K)=0.0
      AEB(J,K)=1.0
   50 CEB(J,K)=0.0
C
      DO 55 J=2,M
      DO 55 I=2,N
      PBB(I,J)=0.0
      ATB(I,J)=1.0
   55 CTB(I,J)=0.0
C
C
C           SOLVING U, V AND W FOR GIVEN P AND T
C
 1000 DO 75 K=2,L
      DO 75 I=2,N
      QSB(I,K)=0.0
   75 SNB(I,K)=0.0
C
      DO 80 K=2,L
      DO 80 J=2,M
      QWB(J,K)=0.0
   80 SEB(J,K)=0.0
```

```
C
      DO 85 J=2,M
      DO 85 I=2,N
      QBB(I,J)=0.0
   85 STB(I,J)=0.0
C
C    SOLVING FOR U
C
      DO 120 K=2,L
      DO 120 J=2,M
      DO 120 I=2,NP
      CALL FLUX(DX(I+1),DX(I),T(I+1,J,K),T(I,J,K),ST)
  120 S(I,J,K)=0.5*(DX(I)+DX(I+1))*DY(J)*DZ(K)*AXI*ST*RG+
     +AXI2*DY(J)*DZ(K)*(PP(I,J,K)-PP(I+1,J,K))
C
      DO 130 K=2,L
      DO 130 J=2,M
      DO 130 I=2,NP
      AE(I,J,K)=0.5*(UP(I,J,K)+UP(I+1,J,K))
      AW(I,J,K)=0.5*(UP(I-1,J,K)+UP(I,J,K))
      CALL
     +FLUX(DX(I+1),DX(I),VP(I+1,J,K),VP(I,J,K),AN(I,J,K))
      CALL FLUX(
     +DX(I+1),DX(I),VP(I+1,J-1,K),VP(I,J-1,K),AS(I,J,K))
      CALL
     +FLUX(DX(I+1),DX(I),WP(I+1,J,K),WP(I,J,K),AT(I,J,K))
      CALL FLUX(
     +DX(I+1),DX(I),WP(I+1,J,K-1),WP(I,J,K-1),AB(I,J,K))
  130 CONTINUE
C
      CALL COEF(DX,DY,DZ,AP1,AE,AW,AN,AS,AT,AB,GX,GY,GZ,
     +NN,MM,LL,N,M,L,NP,M,L,0,1,1,ALFV)
C
      CALL SOLVER(AP1,AE,AW,AN,AS,AT,AB,S,U,PX,QX,PY,QY,
     +PZ,QZ,PSB,QSB,ANB,CNB,SNB,PWB,QWB,AEB,CEB,SEB,PBB,
     +QBB,ATB,CTB,STB,N,M,L,NN,MM,LL,N,MM,LL,ALFV,TOLV1)
C
C    SOLVING FOR V
C
      DO 220 K=2,L
      DO 220 J=2,MP
      DO 220 I=2,N
      CALL FLUX(DY(J+1),DY(J),T(I,J+1,K),T(I,J,K),ST)
```

```
      SW1=0.5*(W(I,J,K-1)+W(I,J,K))
      SW2=0.5*(W(I,J+1,K-1)+W(I,J+1,K))
      CALL FLUX(DY(J+1),DY(J),SW2,SW1,SW)
  220 S(I,J,K)=0.5*DX(I)*(DY(J)+DY(J+1))*DZ(K)*(2.*AZ*RK*SW
     +-ST*(RL+Y(J))/(RL+1.))+DX(I)*DZ(K)*(PP(I,J,K)
     +-PP(I,J+1,K))
C
      DO 230 K=2,L
      DO 230 J=2,MP
      DO 230 I=2,N
      CALL
     +FLUX(DY(J+1),DY(J),UP(I,J+1,K),UP(I,J,K),AE(I,J,K))
      CALL FLUX(
     +DY(J+1),DY(J),UP(I-1,J+1,K),UP(I-1,J,K),AW(I,J,K))
      AN(I,J,K)=0.5*(VP(I,J,K)+VP(I,J+1,K))
      AS(I,J,K)=0.5*(VP(I,J-1,K)+VP(I,J,K))
      CALL
     +FLUX(DY(J+1),DY(J),WP(I,J+1,K),WP(I,J,K),AT(I,J,K))
      CALL FLUX(
     +DY(J+1),DY(J),WP(I,J+1,K-1),WP(I,J,K-1),AB(I,J,K))
  230 CONTINUE
C
      CALL COEF(DX,DY,DZ,AP2,AE,AW,AN,AS,AT,AB,GX,GY,GZ,
     +NN,MM,LL,N,M,L,N,MP,L,1,0,1,ALFV)
C
      CALL SOLVER(AP2,AE,AW,AN,AS,AT,AB,S,V,PX,QX,PY,QY,
     +PZ,QZ,PSB,QSB,ANB,CNB,SNB,PWB,QWB,AEB,CEB,SEB,PBB,
     +QBB,ATB,CTB,STB,N,M,L,NN,MM,LL,NN,M,LL,ALFV,TOLV1)
C
C   SOLVING FOR W
C
      DO 720 K=2,LP
      DO 720 J=2,M
      DO 720 I=2,N
      SV1=0.5*(V(I,J,K)+V(I,J-1,K))
      SV2=0.5*(V(I,J,K+1)+V(I,J-1,K+1))
      CALL FLUX(DZ(K+1),DZ(K),SV2,SV1,SV)
      CALL FLUX(DZ(K+1),DZ(K),T(I,J,K+1),T(I,J,K),ST)
  720 S(I,J,K)=AZI2*DX(I)*DY(J)*(PP(I,J,K)-PP(I,J,K+1))
     +-0.5*DX(I)*DY(J)*(DZ(K)+DZ(K+1))*(AZI*2.0*RK*SV
     ++ST*(Z(K)-0.5)/(RL+1.))
C
      DO 730 K=2,LP
```

```
      DO 730 J=2,M
      DO 730 I=2,N
      CALL
     +FLUX(DZ(K+1),DZ(K),UP(I,J,K+1),UP(I,J,K),AE(I,J,K))
      CALL FLUX(
     +DZ(K+1),DZ(K),UP(I-1,J,K+1),UP(I-1,J,K),AW(I,J,K))
      CALL
     +FLUX(DZ(K+1),DZ(K),VP(I,J,K+1),VP(I,J,K),AN(I,J,K))
      CALL FLUX(
     +DZ(K+1),DZ(K),VP(I,J-1,K+1),VP(I,J-1,K),AS(I,J,K))
      AT(I,J,K)=0.5*(WP(I,J,K)+WP(I,J,K+1))
      AB(I,J,K)=0.5*(WP(I,J,K-1)+WP(I,J,K))
  730 CONTINUE
C
      CALL COEF(DX,DY,DZ,AP3,AE,AW,AN,AS,AT,AB,GX,GY,GZ,
     +NN,MM,LL,N,M,L,N,M,LP,1,1,0,ALFV)
C
      CALL SOLVER(AP3,AE,AW,AN,AS,AT,AB,S,W,PX,QX,PY,QY,
     +PZ,QZ,PSB,QSB,ANB,CNB,SNB,PWB,QWB,AEB,CEB,SEB,PBB,
     +QBB,ATB,CTB,STB,N,M,L,NN,MM,LL,NN,MM,L,ALFV,TOLV1)
C
C
C           PRESSURE CORRECTIONS
C
      DO 310 K=2,L
      DO 310 J=2,M
      DO 310 I=2,N
  310 S(I,J,K)=DY(J)*DZ(K)*(U(I-1,J,K)-U(I,J,K))+
     +DZ(K)*DX(I)*(V(I,J-1,K)-V(I,J,K))+
     +DX(I)*DY(J)*(W(I,J,K-1)-W(I,J,K))
C
      DO 320 K=2,L
      DO 320 J=2,M
      AW(2,J,K)=0.0
  320 AE(N,J,K)=0.0
      DO 330 K=2,L
      DO 330 J=2,M
      DO 330 I=2,NP
      AE(I,J,K)=AA1*AXI2*DY(J)*DZ(K)*DY(J)*DZ(K)/AP1(I,J,K)
  330 AW(I+1,J,K)=AE(I,J,K)
C
      DO 340 K=2,L
      DO 340 I=2,N
```

```
      AS(I,2,K)=0.0
  340 AN(I,M,K)=0.0
      DO 350 K=2,L
      DO 350 J=2,MP
      DO 350 I=2,N
      AN(I,J,K)=AA1*DZ(K)*DX(I)*DZ(K)*DX(I)/AP2(I,J,K)
  350 AS(I,J+1,K)=AN(I,J,K)
C
      DO 353 J=2,M
      DO 353 I=2,N
      AB(I,J,2)=0.0
  353 AT(I,J,L)=0.0
      DO 357 K=2,LP
      DO 357 J=2,M
      DO 357 I=2,N
      AT(I,J,K)=AA1*AZI2*DX(I)*DY(J)*DX(I)*DY(J)/AP3(I,J,K)
  357 AB(I,J,K+1)=AT(I,J,K)
C
      DO 360 K=2,L
      DO 360 J=2,M
      DO 360 I=2,N
  360 AP1(I,J,K)=AE(I,J,K)+AW(I,J,K)+AN(I,J,K)+AS(I,J,K)
     ++AT(I,J,K)+AB(I,J,K)
C
      CALL SOLVER(AP1,AE,AW,AN,AS,AT,AB,S,P,PX,QX,PY,QY,
     +PZ,QZ,PSB,QSB,ANB,CNB,SNB,PWB,QWB,AEB,CEB,SEB,PBB,
     +QBB,ATB,CTB,STB,N,M,L,NN,MM,LL,NN,MM,LL,1.0,TOLP)
C
C
      DO 365 K=2,L
      DO 365 J=2,M
      DO 365 I=2,N
  365 P(I,J,K)=P(I,J,K)-P(N,M,L)
C
      DO 370 K=2,L
      DO 370 J=2,M
      DO 370 I=2,NP
  370 U(I,J,K)=U(I,J,K)+AE(I,J,K)/DY(J)/DZ(K)*(P(I,J,K)
     +-P(I+1,J,K))
C
      DO 380 K=2,L
      DO 380 J=2,MP
      DO 380 I=2,N
```

```
  380 V(I,J,K)=V(I,J,K)+AN(I,J,K)/DZ(K)/DX(I)*(P(I,J,K)
     +-P(I,J+1,K))
C
      DO 385 K=2,LP
      DO 385 J=2,M
      DO 385 I=2,N
  385 W(I,J,K)=W(I,J,K)+AT(I,J,K)/DX(I)/DY(J)*(P(I,J,K)
     +-P(I,J,K+1))
C
      DO 390 K=2,L
      DO 390 I=2,N
      DO 390 J=2,M
  390 PP(I,J,K)=PP(I,J,K)+P(I,J,K)
C
C
C     SOLVING T
C
      RNU0=RNU
C
      DO 450 K=2,L
      DO 450 I=2,N
      QSB(I,K)=-1.0
  450 SNB(I,K)=1.0
C
      DO 453 K=2,L
      DO 453 J=2,M
      QWB(J,K)=GRADT(J)
  453 SEB(J,K)=GRADT(J)
C
      DO 455 J=2,M
      DO 455 I=2,N
      QBB(I,J)=GRADT(J)
  455 STB(I,J)=GRADT(J)
C
      DO 420 K=2,L
      DO 420 J=2,M
      DO 420 I=2,N
  420 S(I,J,K)=0.0
C
      DO 430 K=2,L
      DO 430 J=2,M
      DO 430 I=2,N
      AE(I,J,K)=U(I,J,K)
```

```
      AW(I,J,K)=U(I-1,J,K)
      AN(I,J,K)=V(I,J,K)
      AS(I,J,K)=V(I,J-1,K)
      AT(I,J,K)=W(I,J,K)
      AB(I,J,K)=W(I,J,K-1)
  430 CONTINUE
C
      CALL COEF(DX,DY,DZ,AP1,AE,AW,AN,AS,AT,AB,GTX,GTY,GTZ,
     +NN,MM,LL,N,M,L,N,M,L,1,1,1,1.0)
C
      CALL SOLVER(AP1,AE,AW,AN,AS,AT,AB,S,T,PX,QX,PY,QY,
     +PZ,QZ,PSB,QSB,ANB,CNB,SNB,PWB,QWB,AEB,CEB,SEB,PBB,
     +QBB,ATB,CTB,STB,N,M,L,NN,MM,LL,NN,MM,LL,1.0,TOLT1)
C
      NCC=NCC+1
C
      IF(NCC.GE.NCCR) THEN
      TOLP=AMP*TOLP
      NCC=0
      END IF
C
      NCOUNT=NCOUNT+1
C
      IF(NCOUNT.GE.NCR) THEN
      GO TO 4000
      END IF
C
      RNU=0.0
      DO 500 K=2,L
      DO 500 I=2,N
  500 RNU=RNU+DX(I)*DZ(K)*(T(I,2,K)-T(I,1,K))
C
      ERT=RNU-RNU0
      ERT=ABS(ERT)
      ERT=ERT/RNU
C
      IF(ERT.GT.TOLT2) THEN
      DO 503 K=2,L
      DO 503 J=2,M
      DO 503 I=2,NP
  503 UP(I,J,K)=U(I,J,K)
C
      DO 505 K=2,L
```

```
      DO 505 J=2,MP
      DO 505 I=2,N
  505 VP(I,J,K)=V(I,J,K)
C
      DO 507 K=2,LP
      DO 507 J=2,M
      DO 507 I=2,N
  507 WP(I,J,K)=W(I,J,K)
C
      GO TO 1000
      END IF
C
      CALL ERR(UP,U,N,MM,LL,EU)
      CALL ERR(VP,V,NN,M,LL,EV)
      CALL ERR(WP,W,NN,MM,L,EW)
C
      IF (EU.GT.TOLV2.OR.EV.GT.TOLV2.OR.EW.GT.TOLV2) THEN
C
      DO 520 K=2,L
      DO 520 J=2,M
      DO 520 I=2,NP
  520 UP(I,J,K)=U(I,J,K)
C
      DO 530 K=2,L
      DO 530 J=2,MP
      DO 530 I=2,N
  530 VP(I,J,K)=V(I,J,K)
C
      DO 540 K=2,LP
      DO 540 J=2,M
      DO 540 I=2,N
  540 WP(I,J,K)=W(I,J,K)
      GO TO 1000
      END IF
C
C
 4000 RA=RA*0.008
      RAL=ALOG10(RA)
      RNU=RNU/DY(2)
      RNUL=ALOG10(RNU)
C
      OPEN(7,FILE='OUTPUT')
      WRITE(7,11)(((U(I,J,K),I=1,N),J=1,MM),K=1,LL)
```

```
      WRITE(7,11)(((V(I,J,K),I=1,NN),J=1,M),K=1,LL)
      WRITE(7,11)(((W(I,J,K),I=1,NN),J=1,MM),K=1,L)
      WRITE(7,11)(((T(I,J,K),I=1,NN),J=1,MM),K=1,LL)
      WRITE(7,11)(((PP(I,J,K),I=2,N),J=2,M),K=2,L)
C
      WRITE(7,111)AX,AZ
      WRITE(7,222)RA,RAL
      WRITE(7,333)PRD,EK,RG,RL
      WRITE(7,444)RNU,RNUL
      WRITE(7,555)N,M,L
      WRITE(7,666)NCOUNT,TOLP
      WRITE(7,777)EU,EV,EW,ERT
C
   11 FORMAT(13E15.5)
  111 FORMAT('Ax:',F5.2,'   Az:',F5.2)
  222 FORMAT('Ra:',E11.3,'  Log(Ra/A):',E13.5)
  333 FORMAT('Pr:',E11.3,'  Ek:',E11.3,'  Rg:',E11.3,
     +'  Rl:',E11.3)
  444 FORMAT('Nu:',E14.5,'  LogNu:',E14.5)
  555 FORMAT('Mesh: ',I3,'X',I2,'X',I2)
  666 FORMAT('NCOUNT:',I5,'    TOLP',E15.5)
  777 FORMAT('Eu:',E10.3,'  Ev:',E10.3,'  Ew:',E10.3,
     +'  Et:',e10.3)
C
      STOP
      END
C
C
      SUBROUTINE FLUX(DF,DB,VF,VB,OPT)
      R=1.0/(DF+DB)
      OPT=R*(DB*VF+DF*VB)
      RETURN
      END
C
C
      SUBROUTINE PWRLW(GXY,WW,DDS,DS,JUU)
      F=DDS*WW
      DDI=GXY*DDS/DS
      P=F/DDI
      X=1.0-0.1*ABS(P)
      X=X*X*X*X*X
      X=AMAX1(0.0,X)
      IF (JUU.EQ.1) THEN
```

```
      WW=DDI*X+AMAX1(-F,0.0)
      ELSE
      WW=DDI*X+AMAX1(F,0.0)
      END IF
      RETURN
      END
C
C
      SUBROUTINE COEF(DX,DY,DZ,AP,AE,AW,AN,AS,AT,AB,
     +GX,GY,GZ,NN,MM,LL,N,M,L,NX,NY,NZ,JX,JY,JZ,AL)
      DIMENSION DX(NN),DY(MM),DZ(LL),AP(2:N,2:M,2:L)
      DIMENSION AE(2:N,2:M,2:L),AW(2:N,2:M,2:L)
      DIMENSION AN(2:N,2:M,2:L),AS(2:N,2:M,2:L)
      DIMENSION AT(2:N,2:M,2:L),AB(2:N,2:M,2:L)
C
      ALI=1.0/AL
C
      DO 25 K=2,NZ
      DO 25 J=2,NY
      DO 25 I=2,NX
C
      IF (JX.EQ.1) THEN
      DXE=0.5*(DX(I+1)+DX(I))
      DXW=0.5*(DX(I)+DX(I-1))
      DDX=DX(I)
      ELSE
      DXE=DX(I+1)
      DXW=DX(I)
      DDX=0.5*(DX(I)+DX(I+1))
      END IF
C
      IF (JY.EQ.1) THEN
      DYN=0.5*(DY(J+1)+DY(J))
      DYS=0.5*(DY(J)+DY(J-1))
      DDY=DY(J)
      ELSE
      DYN=DY(J+1)
      DYS=DY(J)
      DDY=0.5*(DY(J)+DY(J+1))
      END IF
C
      IF (JZ.EQ.1) THEN
      DZT=0.5*(DZ(K+1)+DZ(K))
```

```
      DZB=0.5*(DZ(K)+DZ(K-1))
      DDZ=DZ(K)
      ELSE
      DZT=DZ(K+1)
      DZB=DZ(K)
      DDZ=0.5*(DZ(K+1)+DZ(K))
      END IF
C
      AEW=DDY*DDZ
      ANS=DDZ*DDX
      ATB=DDX*DDY
C
      CALL PWRLW(GX,AE(I,J,K),AEW,DXE,1)
      CALL PWRLW(GX,AW(I,J,K),AEW,DXW,0)
      CALL PWRLW(GY,AN(I,J,K),ANS,DYN,1)
      CALL PWRLW(GY,AS(I,J,K),ANS,DYS,0)
      CALL PWRLW(GZ,AT(I,J,K),ATB,DZT,1)
      CALL PWRLW(GZ,AB(I,J,K),ATB,DZB,0)
C
      AP(I,J,K)=ALI*(AE(I,J,K)+AW(I,J,K)+AN(I,J,K)+
     +AS(I,J,K)+AT(I,J,K)+AB(I,J,K))
C
   25 CONTINUE
C
      RETURN
      END
C
C
      SUBROUTINE SOLVER(AP,AE,AW,AN,AS,AT,AB,S,QQ,PX,QX,PY,
     +QY,PZ,QZ,PSB,QSB,ANB,CNB,SNB,PWB,QWB,AEB,CEB,SEB,PBB,
     +QBB,ATB,CTB,STB,N,M,L,NN,MM,LL,NX,NY,NZ,ALF,TOL)
      DIMENSION AE(2:N,2:M,2:L),AW(2:N,2:M,2:L)
      DIMENSION AN(2:N,2:M,2:L),AS(2:N,2:M,2:L)
      DIMENSION AT(2:N,2:M,2:L),AB(2:N,2:M,2:L)
      DIMENSION AP(2:N,2:M,2:L),S(2:N,2:M,2:L),QQ(NX,NY,NZ)
      DIMENSION PSB(2:N,2:L),QSB(2:N,2:L),SNB(2:N,2:L)
      DIMENSION PWB(2:M,2:L),QWB(2:M,2:L),SEB(2:M,2:L)
      DIMENSION PBB(2:N,2:M),QBB(2:N,2:M),STB(2:N,2:M)
      DIMENSION CNB(2:N,2:L),CEB(2:M,2:L),CTB(2:N,2:M)
      DIMENSION ANB(2:N,2:L),AEB(2:M,2:L),ATB(2:N,2:M)
      DIMENSION PX(NN),QX(NN),PY(MM),QY(MM),PZ(LL),QZ(LL)
C
      NXP=NX-1
```

```
      NYP=NY-1
      NZP=NZ-1
C
 100  A1=1.0-ALF
      DO 10 K=2,NZP
      DO 10 J=2,NYP
      DO 10 I=2,NXP
   10 S(I,J,K)=S(I,J,K)+A1*AP(I,J,K)*QQ(I,J,K)
C
      DO 30 K=2,NZP
      DO 30 I=2,NXP
C
      PY(1)=PSB(I,K)
      QY(1)=QSB(I,K)
C
      DO 35 J=2,NYP
      ST=S(I,J,K)+AE(I,J,K)*QQ(I+1,J,K)+AW(I,J,K)
     +*QQ(I-1,J,K)
     ++AT(I,J,K)*QQ(I,J,K+1)+AB(I,J,K)*QQ(I,J,K-1)
      PY(J)=AN(I,J,K)/(AP(I,J,K)-AS(I,J,K)*PY(J-1))
   35 QY(J)=(ST+AS(I,J,K)*QY(J-1))/(AP(I,J,K)
     +-AS(I,J,K)*PY(J-1))
      QY(NY)=(SNB(I,K)+CNB(I,K)*QY(NYP))/(ANB(I,K)
     +-CNB(I,K)*PY(NYP))
C
      QQ(I,NY,K)=QY(NY)
      DO 40 J=1,NYP
   40 QQ(I,NY-J,K)=PY(NY-J)*QQ(I,NY-J+1,K)+QY(NY-J)
   30 CONTINUE
C
      DO 50 K=2,NZP
      DO 50 J=2,NYP
C
      PX(1)=PWB(J,K)
      QX(1)=QWB(J,K)
C
      DO 55 I=2,NXP
      ST=S(I,J,K)+AN(I,J,K)*QQ(I,J+1,K)+AS(I,J,K)*QQ(
     +(I,J-1,K)+AT(I,J,K)*QQ(I,J,K+1)+AB(I,J,K)*QQ(I,J,K-1)
      PX(I)=AE(I,J,K)/(AP(I,J,K)-AW(I,J,K)*PX(I-1))
   55 QX(I)=(ST+AW(I,J,K)*QX(I-1))/(AP(I,J,K)-AW(I,J,K)
     +*PX(I-1))
      QX(NX)=(SEB(J,K)+CEB(J,K)*QX(NXP))/(AEB(J,K)
```

```
     +-CEB(J,K)*PX(NXP))
C
      QQ(NX,J,K)=QX(NX)
      DO 50 I=1,NXP
   50 QQ(NX-I,J,K)=PX(NX-I)*QQ(NX-I+1,J,K)+QX(NX-I)
C
      DO 150 J=2,NYP
      DO 150 I=2,NXP
C
      PZ(1)=PBB(I,J)
      QZ(1)=QBB(I,J)
C
      DO 155 K=2,NZP
      ST=S(I,J,K)+AE(I,J,K)*QQ(I+1,J,K)+AW(I,J,K)*QQ
     +(I-1,J,K)+AN(I,J,K)*QQ(I,J+1,K)+AS(I,J,K)*QQ(I,J-1,K)
      PZ(K)=AT(I,J,K)/(AP(I,J,K)-AB(I,J,K)*PZ(K-1))
  155 QZ(K)=(ST+AB(I,J,K)*QZ(K-1))/(AP(I,J,K)
     +-AB(I,J,K)*PZ(K-1))
      QZ(NZ)=([illegible](I,J)+CTB(I,J)*QZ(NZP))/(ATB(I,J)
     +-CTB(I,J)*PZ(NZP))
C
      QQ(I,J,NZ)=QZ(NZ)
      DO 160 K=1,NZP
  160 QQ(I,J,NZ-K)=PZ(NZ-K)*QQ(I,J,NZ-K+1)+QZ(NZ-K)
  150 CONTINUE
C
      ER=0.0
      DO 60 K=2,NZP
      DO 60 J=2,NYP
      DO 60 I=2,NXP
      X=[illegible]I,J,K)*QQ(I,J,K)-S(I,J,K)
     +-AE(I,J,K)*QQ(I+1,J,K)-AW(I,J,K)*QQ(I-1,J,K)
     +-AN(I,J,K)*QQ(I,J+1,K)-AS(I,J,K)*QQ(I,J-1,K)
     +-AT(I,J,K)*QQ(I,J,K+1)-AB(I,J,K)*QQ(I,J,K-1)
      X=ABS(X)
   60 ER=ER+X
      ER=ER/FLOAT(NXP-1)/FLOAT(NYP-1)/FLOAT(NZP-1)
      IF(ER.GT.TOL) GO TO 100
C
      RETURN
      END
C
C
```

```
      SUBROUTINE ERR(EP,EN,NX,NY,NZ,ER)
      DIMENSION EP(NX,NY,NZ),EN(NX,NY,NZ)
      NXP=NX-1
      NYP=NY-1
      NZP=NZ-1
      RX2=NX-2.0
      RY2=NY-2.0
      RZ2=NZ-2.0
      R3=RX2*RY2*RZ2
      ER=0.0
      DO 81 K=2,NZP
      DO 81 I=2,NXP
      DO 81 J=2,NYP
      E1=EP(I,J,K)-EN(I,J,K)
      E1=E1*E1
      E2=EN(I,J,K)*EN(I,J,K)
      IF (E2.EQ.0.0) THEN
         E1=E1
      ELSE
         E1=E1/E2
      END IF
81    ER=ER+E1
      ER=SQRT(ER)
      ER=ER/R3
      RETURN
      END
```

APPENDIX C

```
C     THIS IS A PROGRAM SOLVING NATURAL CONVECTION PROBLEMS
C          IN ECCENTRIC AND CONCENTRIC ROTATING SYSTEM
C
       PARAMETER(N=51,M=15,L=15,NN=N+1,MM=M+1,LL=L+1)
       PARAMETER(NP=N-1,MP=M-1,LP=L-1)
       DIMENSION UP(N,MM,LL),VP(NN,M,LL),WP(NN,MM,L)
       DIMENSION T(NN,MM,LL),PP(NN,MM,LL),P(NN,MM,LL)
       DIMENSION U(N,MM,LL),V(NN,M,LL),W(NN,MM,L),GRADT(NN)
       DIMENSION DX(NN),DY(MM),DZ(LL),AP3(2:N,2:M,2:L)
       DIMENSION Y(M),Z(L)
       DIMENSION PX(NN),QX(NN),PY(MM),QY(MM),PZ(LL),QZ(LL)
       DIMENSION
      +AP1(2:N,2:M,2:L),AP2(2:N,2:M,2:L),S(2:N,2:M,2:L)
       DIMENSION
      +AE(2:N,2:M,2:L),AW(2:N,2:M,2:L),AN(2:N,2:M,2:L)
       DIMENSION
      +AS(2:N,2:M,2:L),AT(2:N,2:M,2:L),AB(2:N,2:M,2:L)
       DIMENSION
      +PSB(2:N,2:L),QSB(2:N,2:L),ANB(2:N,2:L),CNB(2:N,2:L)
       DIMENSION
      +PWB(2:M,2:L),QWB(2:M,2:L),AEB(2:M,2:L),CEB(2:M,2:L)
       DIMENSION
      +PBB(2:N,2:M),QBB(2:N,2:M),ATB(2:N,2:M),CTB(2:N,2:M)
       DIMENSION SEB(2:M,2:L),SNB(2:N,2:L),STB(2:N,2:M)
C
C      CALL SYS$DISEXC(0,0,0,4)
C
       OPEN(5,FILE='D1')
       READ(5,*)AX,AZ
       READ(5,*)RA,PRD,EK,RG,RL
       READ(5,*)ALFV
       READ(5,*)TOLV1,TOLV2,TOLT1,TOLT2,TOLP
       READ(5,*)(DX(I),I=1,NN)
       READ(5,*)(DY(J),J=1,MM)
       READ(5,*)(DZ(K),K=1,LL)
       READ(5,*)NCR,NCCR,AMP
C
       Y(1)=DY(1)
       Z(1)=DZ(1)
       DO 21 J=2,M
   21  Y(J)=Y(J-1)+DY(J)
```

```
      DO 23 K=2,L
   23 Z(K)=Z(K-1)+DZ(K)
C
      AA1=1.0/(1.0-ALFV)
C
      AX2=AX*AX
      AZ2=AZ*AZ
      RY=1.0/(SQRT((2.0*PRD)/RA))
      RX=RY*AX2
      RZ=RY*AZ2
      AXI=1.0/AX
      AXI2=AXI*AXI
      AZI=1.0/AZ
      AZI2=AZI*AZI
      RK=SQRT((2.0*PRD)/(RA*F..**2))
      RL1=1./(RL+1.)
C
      GX=1.0/RX
      GY=1.0/RY
      GZ=1.0/RZ
      GTZ=GZ/PRD
      GTX=GX/PRD
      GTY=GY/PRD
      NCOUNT=0
      NCC=0
C
C       INPUT INITIAL GUESSED VALUES FOR U, V, W AND T
C
      OPEN(4,FILE='IN')
      READ(4,11)(((UP(I,J,K),I=1,N),J=1,MM),K=1,LL)
      READ(4,11)(((VP(I,J,K),I=1,NN),J=1,M),K=1,LL)
      READ(4,11)(((WP(I,J,K) I=1,NN),J=1,MM),K=1,L)
      READ(4,11)(((T(I,J,K),I=1,NN),J=1,MM),K=1,LL)
      READ(4,11)(((PP(I,J,K),I=2,N),J=2,M),K=2,L)
C
      DO 22 K=1,LL
      DO 22 J=1,MM
      DO 22 I=1,N
   22 U(I,J,K)=UP(I,J,K)
C
      DO 24 K=1,LL
      DO 24 J=1,M
      DO 24 I=1,NN
```

```
   24 V(I,J,K)=VP(I,J,K)
C
      DO 26 K=1,L
      DO 26 J=1,MM
      DO 26 I=1,NN
   26 W(I,J,K)=WP(I,J,K)
C
C
C           APPLY BOUNDARY CONDITIONS
C
      GRADT(1)=1.0
      DO 33 I=1,N
   33 GRADT(I+1)=GRADT(I)-DX(I)-DX(I+1)
C
      DO 45 K=2,L
      DO 45 I=2,N
      PSB(I,K)=0.0
      ANB(I,K)=1.0
   45 CNB(I,K)=0.0
C
      DO 50 K=2,L
      DO 50 J=2,M
      PWB(J,K)=0.0
      AEB(J,K)=1.0
   50 CEB(J,K)=0.0
C
      DO 55 J=2,M
      DO 55 I=2,N
      PBB(I,J)=0.0
      ATB(I,J)=1.0
   55 CTB(I,J)=0.0
C
C
C             SOLVING U, V AND W FOR GIVEN P AND T
C
 1000 DO 75 K=2,L
      DO 75 I=2,N
      QSB(I,K)=0.0
   75 SNB(I,K)=0.0
C
      DO 80 K=2,L
      DO 80 J=2,M
      QWB(J,K)=0.0
```

```
   80 SEB(J,K)=0.0
C
      DO 85 J=2,M
      DO 85 I=2,N
      QBB(I,J)=0.0
   85 STB(I,J)=0.0
C
C   SOLVING FOR U
C
      DO 120 K=2,L
      DO 120 J=2,M
      DO 120 I=2,NP
      CALL FLUX(DX(I+1),DX(I),T(I+1,J,K),T(I,J,K),ST)
  120 S(I,J,K)=0.5*(DX(I)+DX(I+1))*DY(J)*DZ(K)*AXI*ST*RG+
     +AXI2*DY(J)*DZ(K)*(PP(I,J,K)-PP(I+1,J,K))
C
      DO 130 K=2,L
      DO 130 J=2,M
      DO 130 I=2,NP
      AE(I,J,K)=0 5*(UP(I,J,K)+UP(I+1,J,K))
      AW(I,J,[illegible] (UP(I-1,J,K)+UP(I,J,K))
      CALL
     +FLUX(DX(I+1),DX(I),VP(I+1,J,K),VP(I,J,K),AN(I,J,K))
      CALL FLUX(
     +DX(I+1),DX(I),VP(I+1,J-1,K),VP(I,J-1,K),AS(I,J,K))
      CALL
     +FLUX(DX(I+1),DX(I),WP(I+1,J,K),WP(I,J,K),AT(I,J,K))
      CALL FLUX(
     +DX(I+1),DX(I),WP(I+1,J,K-1),WP(I,J,K-1),AB(I,J,K))
  130 CONTINUE
C
      CALL COEF(DX,DY,DZ,AP1,AE,AW,AN,AS,AT,AB,GX,GY,GZ,
     +NN,MM,LL,N,M,L,NP,M,L,0,1,1,ALFV)
C
      CALL SOLVER(AP1,AE,AW,AN,AS,AT,AB,S,U,PX,QX,PY,QY,
     +PZ,QZ,PSB,QSB,ANB,CNB,SNB,PWB,QWB,AEB,CEB,SEB,PBB,
     +QBB,ATB,CTB,STB,N,M,L,NN,MM,LL,N,MM,LL,ALFV,TOLV1)
C
C   SOLVING FOR V
C
      DO 220 K=2,L
      DO 220 J=2,MP
      DO 220 I=2,N
```

```
      CALL FLUX(DY(J+1),DY(J),T(I,J+1,K),T(I,J,K),ST)
      SW1=0.5*(W(I,J,K-1)+W(I,J,K))
      SW2=0.5*(W(I,J+1,K-1)+W(I,J+1,K))
      CALL FLUX(DY(J+1),DY(J),SW2,SW1,SW)
  220 S(I,J,K)=0.5*DX(I)*(DY(J)+DY(J+1))*DZ(K)*(2.*AZ*RK*SW
     +-ST*(RL+Y(J))*RL1)+DX(I)*DZ(K)*(PP(I,J,K)-PP(I,J+1,K))
C
      DO 230 K=2,L
      DO 230 J=2,MP
      DO 230 I=2,N
      CALL
     +FLUX(DY(J+1),DY(J),UP(I,J+1,K),UP(I,J,K),AE(I,J,K))
      CALL FLUX(
     +DY(J+1),DY(J),UP(I-1,J+1,K),UP(I-1,J,K),AW(I,J,K))
      AN(I,J,K)=0.5*(VP(I,J,K)+VP(I,J+1,K))
      AS(I,J,K)=0.5*(VP(I,J-1,K)+VP(I,J,K))
      CALL
     +FLUX(DY(J+1),DY(J),WP(I,J+1,K),WP(I,J,K),AT(I,J,K))
      CALL FLUX(
     +DY(J+1),DY(J),WP(I,J+1,K-1),WP(I,J,K-1),AB(I,J,K))
  230 CONTINUE
C
      CALL COEF(DX,DY,DZ,AP2,AE,AW,AN,AS,AT,AB,GX,GY,GZ,
     +NN,MM,LL,N,M,L,N,MP,L,1,0,1,ALFV)
C
      CALL SOLVER(AP2,AE,AW,AN,AS,AT,AB,S,V,PX,QX,PY,QY,
     +PZ,QZ,PSB,QSB,ANB,CNB,SNB,PWB,QWB,AEB,CEB,SEB,PBB,
     +QBB,ATB,CTB,STB,N,M,L,NN,MM,LL,NN,M,LL,ALFV,TOLV1)
C
C    SOLVING FOR W
C
      DO 720 K=2,LP
      DO 720 J=2,M
      DO 720 I=2,N
      SV1=0.5*(V(I,J,K)+V(I,J-1,K))
      SV2=0.5*(V(I,J,K+1)+V(I,J-1,K+1))
      CALL FLUX(DZ(K+1),DZ(K),SV2,SV1,SV)
      CALL FLUX(DZ(K+1),DZ(K),T(I,J,K+1),T(I,J,K),ST)
  720 S(I,J,K)=AZI2*DX(I)*DY(J)*(PP(I,J,K)-PP(I,J,K+1))
     +-0.5*DX(I)*DY(J)*(DZ(K)+DZ(K+1))*(AZ*2.0*RK*SV+
     +ST*(Z(K)-0.5)*RL1)
C
      DO 730 K=2,LP
```

```
      DO 730 J=2,M
      DO 730 I=2,N
      CALL
     +FLUX(DZ(K+1),DZ(K),UP(I,J,K+1),UP(I,J,K),AE(I,J,K))
      CALL FLUX(
     +DZ(K+1),DZ(K),UP(I-1,J,K+1),UP(I-1,J,K),AW(I,J,K))
      CALL
      FLUX(DZ(K+1),DZ(K),VP(I,J,K+1),VP(I,J,K),AN(I,J,K))
      CALL FLUX(
     +DZ(K+1),DZ(K),VP(I,J-1,K+1),VP(I,J-1,K),AS(I,J,K))
      AT(I,J,K)=0.5*(WP(I,J,K)+WP(I,J,K+1))
      AB(I,J,K)=0.5*(WP(I,J,K-1)+WP(I,J,K))
  730 CONTINUE
C
      CALL COEF(DX,DY,DZ,AP3,AE,AW,AN,AS,AT,AB,GX,GY,GZ,
     +NN,MM,LL,N,M,L,N,M,LP,1,1,0,ALFV)
C
      CALL SOLVER(AP3,AE,AW,AN,AS,AT,AB,S,W,PX,QX,PY,QY,
     +PZ,QZ,PSB,QSB,ANB,CNB,SNB,PWB,QWB,AEB,CEB,SEB,PBB,
     +QBB,ATB,CTB,STB,N,M,L,NN,MM,LL,NN,MM,L,ALFV,TOLV1)
C
C
C            PRESSURE CORRECTIONS
C
      DO 310 K=2,L
      DO 310 J=2,M
      DO 310 I=2,N
  310 S(I,J,K)=DY(J)*DZ(K)*(U(I-1,J,K)-U(I,J,K))+
     +DZ(K)*DX(I)*(V(I,J-1,K)-V(I,J,K))+
     +DX(I)*DY(J)*(W(I,J,K-1)-W(I,J,K))
C
      DO 320 K=2,L
      DO 320 J=2,M
      AW(2,J,K)=0.0
  320 AE(N,J,K)=0.0
      DO 330 K=2,L
      DO 330 J=2,M
      DO 330 I=2,NP
      AE(I,J,K)=AA1*AXI2*DY(J)*DZ(K)*DY(J)*DZ(K)/AP1(I,J,K)
  330 AW(I+1,J,K)=AE(I,J,K)
C
      DO 340 K=2,L
      DO 340 I=2,N
```

```
      AS(I,2,K)=0.0
  340 AN(I,M,K)=0.0
      DO 350 K=2,L
      DO 350 J=2,MP
      DO 350 I=2,N
      AN(I,J,K)=AA1*DZ(K)*DX(I)*DZ(K)*DX(I)/AP2(I,J,K)
  350 AS(I,J+1,K)=AN(I,J,K)
C
      DO 353 J=2,M
      DO 353 I=2,N
      AB(I,J,2)=0.0
  353 AT(I,J,L)=0.0
      DO 357 K=2,LP
      DO 357 J=2,M
      DO 357 I=2,N
      AT(I,J,K)=AA1*AZI2*DX(I)*DY(J)*DX(I)*DY(J)/AP3(I,J,K)
  357 AB(I,J,K+1)=AT(I,J,K)
C
      DO 360 K=2,L
      DO 360 J=2,M
      DO 360 I=2,N
  360 AP1(I,J,K)=AE(I,J,K)+AW(I,J,K)+AN(I,J,K)+AS(I,J,K)
     ++AT(I,J,K)+AB(I,J,K)
C
      CALL SOLVER(AP1,AE,AW,AN,AS,AT,AB,S,P,PX,QX,PY,QY,
     +PZ,QZ,PSB,QSB,ANB,CNB,SNB,PWB,QWB,AEB,CEB,SEB,PBB,
     +QBB,ATB,CTB,STB,N,M,L,NN,MM,LL,NN,MM,LL,1.0,TOLP)
C
C
      DO 365 K=2,L
      DO 365 J=2,M
      DO 365 I=2,N
  365 P(I,J,K)=P(I,J,K)-P(N,M,L)
C
      DO 370 K=2,L
      DO 370 J=2,M
      DO 370 I=2,NP
  370 U(I,J,K)=U(I,J,K)+AE(I,J,K)/DY(J)/DZ(K)*(P(I,J,K)
     +-P(I+1,J,K))
C
      DO 380 K=2,L
      DO 380 J=2,MP
      DO 380 I=2,N
```

```
  380 V(I,J,K)=V(I,J,K)+AN(I,J,K)/DZ(K)/DX(I)*(P(I,J,K)
     +-P(I,J+1,K))
C
      DO 385 K=2,LP
      DO 385 J=2,M
      DO 385 I=2,N
  385 W(I,J,K)=W(I,J,K)+AT(I,J,K)/DX(I)/DY(J)*(P(I,J,K)
     +-P(I,J,K+1))
C
      DO 390 K=2,L
      DO 390 I=2,N
      DO 390 J=2,M
  390 PP(I,J,K)=PP(I,J,K)+P(I,J,K)
C
C
C     SOLVING T
C
      RNU0=RNU
C
      DO 450 K=2,L
      DO 450 I=2,N
      QSB(I,K)=GRADT(I)
  450 SNB(I,K)=GRADT(I)
C
      DO 453 K=2,L
      DO 453 J=2,M
      QWB(J,K)=1.0
  453 SEB(J,K)=-1.0
C
      DO 455 J=2,M
      DO 455 I=2,N
      QBB(I,J)=GRADT(I)
  455 STB(I,J)=GRADT(I)
C
      DO 420 K=2,L
      DO 420 J=2,M
      DO 420 I=2,N
  420 S(I,J,K)=0.0
C
      DO 430 K=2,L
      DO 430 J=2,M
      DO 430 I=2,N
      AE(I,J,K)=U(I,J,K)
```

```
      AW(I,J,K)=U(I-1,J,K)
      AN(I,J,K)=V(I,J,K)
      AS(I,J,K)=V(I,J-1,K)
      AT(I,J,K)=W(I,J,K)
      AB(I,J,K)=W(I,J,K-1)
  430 CONTINUE
C
      CALL COEF(DX,DY,DZ,AP1,AE,AW,AN,AS,AT,AB,GTX,GTY,GTZ,
     +NN,MM,LL,N,M,L,N,M,L,1,1,1,1.0)
C
      CALL SOLVER(AP1,AE,AW,AN,AS,AT,AB,S,T,PX,QX,PY,QY,
     +PZ,QZ,PSB,QSB,ANB,CNB,SNB,PWB,QWB,AEB,CEB,SEB,PBB,
     +QBB,ATB,CTB,STB,N,M,L,NN,MM,LL,NN,MM,LL,1.0,TOLT1)
C
      NCC=NCC+1
C
      IF(NCC.GE.NCCR) THEN
      TOLP=AMP*TOLP
      NCC=0
      END IF
C
      NCOUNT=NCOUNT+1
C
      IF(NCOUNT.GE.NCR) THEN
      GO TO 4000
      END IF
C
      RNU=0.0
      DO 500 K=2,L
      DO 500 J=2,M
  500 RNU=RNU+DY(J)*DZ(K)*(T(1,J,K)-T(2,J,K))
C
      ERT=RNU-RNU0
      ERT=ABS(ERT)
      ERT=ERT/RNU
C
      IF(ERT.GT.TOLT2) THEN
      DO 503 K=2,L
      DO 503 J=2,M
      DO 503 I=2,NP
  503 UP(I,J,K)=U(I,J,K)
C
      DO 505 K=2,L
```

```
      DO 505 J=2,MP
      DO 505 I=2,N
  505 VP(I,J,K)=V(I,J,K)
C
      DO 507 K=2,LP
      DO 507 J=2,M
      DO 507 I=2,N
  507 WP(I,J,K)=W(I,J,K)
C
      GO TO 1000
      END IF
C
      CALL ERR(UP,U,N,MM,LL,EU)
      CALL ERR(VP,V,NN,M,LL,EV)
      CALL ERR(WP,W,NN,MM,L,EW)
C
      IF (EU.GT.TOLV2.OR.EV.GT.TOLV2.OR.EW.GT.TOLV2) THEN
C
      DO 520 K=2,L
      DO 520 J=2,M
      DO 520 I=2,NP
  520 UP(I,J,K)=U(I,J,K)
C
      DO 530 K=2,L
      DO 530 J=2,MP
      DO 530 I=2,N
  530 VP(I,J,K)=V(I,J,K)
C
      DO 540 K=2,LP
      DO 540 J=2,M
      DO 540 I=2,N
  540 WP(I,J,K)=W(I,J,K)
      GO TO 1000
      END IF
C
C
 4000 RAL=ALOG10(RA)
      RNU=RNU/DY(2)
C
      OPEN(7,FILE='OUTPUT')
      WRITE(7,11)(((U(I,J,K),I=1,N),J=1,MM),K=1,LL)
      WRITE(7,11)(((V(I,J,K),I=1,NN),J=1,M),K=1,LL)
      WRITE(7,11)(((W(I,J,K),I=1,NN),J=1,MM),K=1,L)
```

```
      WRITE(7,11)(((T(I,J,K),I=1,NN),J=1,MM),K=1,LL)
      WRITE(7,11)(((PP(I,J,K),I=2,N),J=2,M),K=2,L)
C
      WRITE(7,111)AX,AZ
      WRITE(7,222)RA,RAL
      WRITE(7,333)PRD,EK,RG,RL
      WRITE(7,444)RNU
      WRITE(7,555)N,M,L
      WRITE(7,666)NCOUNT,TOLP
      WRITE(7,777)EU,EV,EW,ERT
C
   11 FORMAT(13E15.5)
  111 FORMAT('Ax:',F5.2,'   Az:',F5.2)
  222 FORMAT('Ra:',E11.3,'  Log(Ra/A):',E13.5)
  333 FORMAT('Pr:',E11.3,'  Ek:',E11.3,'  Rg:',E11.3,
     +'  Rl:',E11.3)
  444 FORMAT('Nu:',E14.5)
  555 FORMAT('Mesh: ',I3,'X',I2,'X',I2)
  666 FORMAT('NCOUNT:',I5,'   TOLP',E15.5)
  777 FORMAT('Eu:',E10.3,'  Ev:',E10.3,'  Ew:',E10.3,
     +'  Et:',E10.3)
C
      STOP
      END
C
C
      SUBROUTINE FLUX(DF,DB,VF,VB,OPT)
      R=1.0/(DF+DB)
      OPT=R*(DB*VF+DF*VB)
      RETURN
      END
C
C
      SUBROUTINE PWRLW(GXY,WW,DDS,DS,JUU)
      F=DDS*WW
      DDI=GXY*DDS/DS
      P=F/DDI
      X=1.0-0.1*ABS(P)
      X=X*X*X*X*X
      X=AMAX1(0.0,X)
      IF (JUU.EQ.1) THEN
      WW=DDI*X+AMAX1(-F,0.0)
      ELSE
```

```
      WW=DDI*X+AMAX1(F,0.0)
      END IF
      RETURN
      END
C
C
      SUBROUTINE COEF(DX,DY,DZ,AP,AE,AW,AN,AS,AT,AB,
     +GX,GY,GZ,NN,MM,LL,N,M,L,NX,NY,NZ,JX,JY,JZ,AL)
      DIMENSION DX(NN),DY(MM),DZ(LL),AP(2:N,2:M,2:L)
      DIMENSION AE(2:N,2:M,2:L),AW(2:N,2:M,2:L)
      DIMENSION AN(2:N,2:M,2:L),AS(2:N,2:M,2:L)
      DIMENSION AT(2:N,2:M,2:L),AB(2:N,2:M,2:L)
C
      ALI=1.0/AL
C
      DO 25 K=2,NZ
      DO 25 J=2,NY
      DO 25 I=2,NX
C
      IF (JX.EQ.1) THEN
      DXE=0.5*(DX(I+1)+DX(I))
      DXW=0.5*(DX(I)+DX(I-1))
      DDX=DX(I)
      ELSE
      DXE=DX(I+1)
      DXW=DX(I)
      DDX=0.5*(DX(I)+DX(I+1))
      END IF
C
      IF (JY.EQ.1) THEN
      DYN=0.5*(DY(J+1)+DY(J))
      DYS=0.5*(DY(J)+DY(J-1))
      DDY=DY(J)
      ELSE
      DYN=DY(J+1)
      DYS=DY(J)
      DDY=0.5*(DY(J)+DY(J+1))
      END IF
C
      IF (JZ.EQ.1) THEN
      DZT=0.5*(DZ(K+1)+DZ(K))
      DZB=0.5*(DZ(K)+DZ(K-1))
      DDZ=DZ(K)
```

```
      ELSE
      DZT=DZ(K+1)
      DZB=DZ(K)
      DDZ=0.5*(DZ(K+1)+DZ(K))
      END IF
C
      AEW=DDY*DDZ
      ANS=DDZ*DDX
      ATB=DDX*DDY
C
      CALL PWRLW(GX,AE(I,J,K),AEW,DXE,1)
      CALL PWRLW(GX,AW(I,J,K),AEW,DXW,0)
      CALL PWRLW(GY,AN(I,J,K),ANS,DYN,1)
      CALL PWRLW(GY,AS(I,J,K),ANS,DYS,0)
      CALL PWRLW(GZ,AT(I,J,K),ATB,DZT,1)
      CALL PWRLW(GZ,AB(I,J,K),ATB,DZB,0)
C
      AP(I,J,K)=ALI*(AE(I,J,K)+AW(I,J,K)+AN(I,J,K)+
     +AS(I,J,K)+AT(I,J,K)+AB(I,J,K))
C
   25 CONTINUE
C
      RETURN
      END
C
C
      SUBROUTINE SOLVER(AP,AE,AW,AN,AS,AT,AB,S,QQ,PX,QX,PY,
     +QY,PZ,QZ,PSB,QSB,ANB,CNB,SNB,PWB,QWB,AEB,CEB,SEB,PBB,
     +QBB,ATB,CTB,STB,N,M,L,NN,MM,LL,NX,NY,NZ,ALF,TOL)
      DIMENSION AE(2:N,2:M,2:L),AW(2:N,2:M,2:L)
      DIMENSION AN(2:N,2:M,2:L),AS(2:N,2:M,2:L)
      DIMENSION AT(2:N,2:M,2:L),AB(2:N,2:M,2:L)
      DIMENSION AP(2:N,2:M,2:L),S(2:N,2:M,2:L),QQ(NX,NY,NZ)
      DIMENSION PSB(2:N,2:L),QSB(2:N,2:L),SNB(2:N,2:L)
      DIMENSION PWB(2:M,2:L),QWB(2:M,2:L),SEB(2:M,2:L)
      DIMENSION PBB(2:N,2:M),QBB(2:N,2:M),STB(2:N,2:M)
      DIMENSION CNB(2:N,2:L),CEB(2:M,2:L),CTB(2:N,2:M)
      DIMENSION ANB(2:N,2:L),AEB(2:M,2:L),ATB(2:N,2:M)
      DIMENSION PX(NN),QX(NN),PY(MM),QY(MM),PZ(LL),QZ(LL)
C
      NXP=NX-1
      NYP=NY-1
      NZP=NZ-1
```

```
C
 100  A1=1.0-ALF
      DO 10 K=2,NZP
      DO 10 J=2,NYP
      DO 10 I=2,NXP
   10 S(I,J,K)=S(I,J,K)+A1*AP(I,J,K)*QQ(I,J,K)
C
      DO 30 K=2,NZP
      DO 30 I=2,NXP
C
      PY(1)=PSB(I,K)
      QY(1)=QSB(I,K)
C
      DO 35 J=2,NYP
      ST=S(I,J,K)+AE(I,J,K)*QQ(I+1,J,K)+AW(I,J,K)
     +*QQ(I-1,J,K)
     ++AT(I,J,K)*QQ(I,J,K+1)+AB(I,J,K)*QQ(I,J,K-1)
      PY(J)=AN(I,J,K)/(AP(I,J,K)-AS(I,J,K)*PY(J-1))
   35 QY(J)=(ST+AS(I,J,K)*QY(J-1))/(AP(I,J,K)
     +-AS(I,J,K)*PY(J-1))
      QY(NY)=(SNB(I,K)+CNB(I,K)*QY(NYP))/(ANB(I,K)
     +-CNB(I,K)*PY(NYP))
C
      QQ(I,NY,K)=QY(NY)
      DO 40 J=1,NYP
   40 QQ(I,NY-J,K)=PY(NY-J)*QQ(I,NY-J+1,K)+QY(NY-J)
   30 CONTINUE
C
      DO 50 K=2,NZP
      DO 50 J=2,NYP
C
      PX(1)=PWB(J,K)
      QX(1)=QWB(J,K)
C
      DO 55 I=2,NXP
      ST=S(I,J,K)+AN(I,J,K)*QQ(I,J+1,K)+AS(I,J,K)*QQ(
     +(I,J-1,K)+AT(I,J,K)*QQ(I,J,K+1)+AB(I,J,K)*QQ(I,J,K-1)
      PX(I)=AE(I,J,K)/(AP(I,J,K)-AW(I,J,K)*PX(I-1))
   55 QX(I)=(ST+AW(I,J,K)*QX(I-1))/(AP(I,J,K)-AW(I,J,K)
     +*PX(I-1))
      QX(NX)=(SEB(J,K)+CEB(J,K)*QX(NXP))/(AEB(J,K)
     +-CEB(J,K)*PX(NXP))
C
```

```
      QQ(NX,J,K)=QX(NX)
      DO 50 I=1,NXP
   50 QQ(NX-I,J,K)=PX(NX-I)*QQ(NX-I+1,J,K)+QX(NX-I)
C
      DO 150 J=2,NYP
      DO 150 I=2,NXP
C
      PZ(1)=PBB(I,J)
      QZ(1)=QBB(I,J)
C
      DO 155 K=2,NZP
      ST=S(I,J,K)+AE(I,J,K)*QQ(I+1,J,K)+AW(I,J,K)*QQ
     +(I-1,J,K)+AN(I,J,K)*QQ(I,J+1,K)+AS(I,J,K)*QQ(I,J-1,K)
      PZ(K)=AT(I,J,K)/(AP(I,J,K)-AB(I,J,K)*PZ(K-1))
  155 QZ(K)=(ST+AB(I,J,K)*QZ(K-1))/(AP(I,J,K)
     +-AB(I,J,K)*PZ(K-1))
      QZ(NZ)=(STB(I,J)+CTB(I,J)*QZ(NZP))/(ATB(I,J)
     +-CTB(I,J)*PZ(NZP))
C
      QQ(I,J,NZ)=QZ(NZ)
      DO 160 K=1,NZP
  160 QQ(I,J,NZ-K)=PZ(NZ-K)*QQ(I,J,NZ-K+1)+QZ(NZ-K)
  150 CONTINUE
C
      ER=0.0
      DO 60 K=2,NZP
      DO 60 J=2,NYP
      DO 60 I=2,NXP
      X=AP(I,J,K)*QQ(I,J,K)-S(I,J,K)
     +-AE(I,J,K)*QQ(I+1,J,K)-AW(I,J,K)*QQ(I-1,J,K)
     +-AN(I,J,K)*QQ(I,J+1,K)-AS(I,J,K)*QQ(I,J-1,K)
     +-AT(I,J,K)*QQ(I,J,K+1)-AB(I,J,K)*QQ(I,J,K-1)
      X=ABS(X)
   60 ER=ER+X
      ER=ER/FLOAT(NXP-1)/FLOAT(NYP-1)/FLOAT(NZP-1)
      IF(ER.GT.TOL) GO TO 100
C
      RETURN
      END
C
C
      SUBROUTINE ERR(EP,EN,NX,NY,NZ,ER)
      DIMENSION EP(NX,NY,NZ),EN(NX,NY,NZ)
```

```
      NXP=NX-1
      NYP=NY-1
      NZP=NZ-1
      RX2=NX-2.0
      RY2=NY-2.0
      RZ2=NZ-2.0
      R3=RX2*RY2*RZ2
      ER=0.0
      DO 81 K=2,NZP
      DO 81 I=2,NXP
      DO 81 J=2,NYP
      E1=EP(I,J,K)-EN(I,J,K)
      E1=E1*E1
      E2=EN(I,J,K)*EN(I,J,K)
      IF (E2.EQ.0.0) THEN
         E1=E1
      ELSE
         E1=E1/E2
      END IF
 81   ER=ER+E1
      ER=SQRT(ER)
      ER=ER/R3
      RETURN
      END
```